Volcanic tremor analysis based on advanced signal processing concepts including music information retrieval (MIR) strategies

---

Zahra Zali

Cumulative dissertation
for the degree of doctor rerum naturalium
(Dr. rer. nat.)

Submitted to the Faculty of Mathematics and Natural Science
Institute for Geosciences at the University of Potsdam

Date of disputation: September 12, 2023

Submitted on April 17, 2023

Supervisors:
Prof. Fabrice Cotton
Dr. Matthias Ohrnberger

Mentor:
Prof. Frank Scherbaum

External Reviewers:
Prof. Florent Brenguier
Prof. Conny Hammer

Examination Board:
Prof. Fabrice Cotton
Prof. Florent Brenguier
Prof. Conny Hammer
Prof. Frank Kruger
Prof. Eva Eibl

Published online on the
Publication Server of the University of Potsdam:
https://doi.org/10.25932/publishup-61086
https://nbn-resolving.org/urn:nbn:de:kobv:517-opus4-610866

Declaration of Authorship

I, Zahra Zali, hereby declare that this work has been completed by myself. I have fully acknowledged and referenced the ideas and work of others, whether published or unpublished, in my thesis. Furthermore, this dissertation has not been submitted to any other university.

Zahra Zali

Potsdam, April 2023

Abstract

Volcanoes are one of the Earth's most dynamic zones and responsible for many changes in our planet. Volcano seismology aims to provide an understanding of the physical processes in volcanic systems and anticipate the style and timing of eruptions by analyzing the seismic records. Volcanic tremor signals are usually observed in the seismic records before or during volcanic eruptions. Their analysis contributes to evaluate the evolving volcanic activity and potentially predict eruptions. Years of continuous seismic monitoring now provide useful information for operational eruption forecasting. The continuously growing amount of seismic recordings, however, poses a challenge for analysis, information extraction, and interpretation, to support timely decision making during volcanic crises. Furthermore, the complexity of eruption processes and precursory activities makes the analysis challenging.

A challenge in studying seismic signals of volcanic origin is the coexistence of transient signal swarms and long-lasting volcanic tremor signals. Separating transient events from volcanic tremors can, therefore, contribute to improving our understanding of the underlying physical processes. Some similar issues (data reduction, source separation, extraction, and classification) are addressed in the context of music information retrieval (MIR). The signal characteristics of acoustic and seismic recordings comprise a number of similarities. This thesis is going beyond classical signal analysis techniques usually employed in seismology by exploiting similarities of seismic and acoustic signals and building the information retrieval strategy on the expertise developed in the field of MIR.

First, inspired by the idea of harmonic–percussive separation (HPS) in musical signal processing, I have developed a method to extract harmonic volcanic tremor signals and to detect transient events from seismic recordings. This provides a clean tremor signal suitable for tremor investigation along with a characteristic function suitable for earthquake detection. Second, using HPS algorithms, I have developed a noise reduction technique for seismic signals. This method is especially useful for denoising ocean bottom seismometers, which are highly contaminated by noise. The advantage of this method compared to other denoising techniques is that it doesn't introduce distortion to the broadband earthquake waveforms, which makes it reliable for different applications in passive seismological analysis. Third, to address the challenge of extracting information from high-dimensional data and investigating the complex eruptive phases, I have developed an advanced machine learning model that results in a comprehensive signal processing scheme for volcanic tremors. Using this method seismic signatures of major eruptive phases can be automatically detected. This helps to provide a chronology of the volcanic system. Also, this model is capable to detect weak precursory volcanic tremors prior to the eruption, which could be used as an indicator of imminent eruptive activity. The extracted patterns of seismicity and their temporal variations finally provide an explanation for the transition mechanism between eruptive phases.

Zusammenfassung

Vulkane gehören zu den dynamischsten Zonen der Erde und sind für viele Veränderungen auf unserem Planeten verantwortlich. Die Vulkanseismologie zielt darauf ab, physikalischen Prozesse in Vulkansystemen besser zu verstehen und die Art und den Zeitpunkt von Eruptionen durch die Analyse der seismischen Aufzeichnungen vorherzusagen. Die Signale vulkanischer Tremore werden normalerweise vor oder während Vulkanausbrüchen beobachtet und müssen überwacht werden, um die vulkanische Aktivität zu bewerten. Die Untersuchung vulkanischer Tremore ist ein wichtiger Teil der Vulkanüberwachung, die darauf abzielt, Anzeichen für das Erwachen oder Wiedererwachen von Vulkanen zu erkennen und möglicherweise Ausbrüche vorherzusagen. Mehrere Dekaden kontinuierlicher seismischer Überwachung liefern nützliche Informationen für die operative Eruptionsvorhersage. Die ständig wachsende Menge an seismischen Aufzeichnungen stellt jedoch eine Herausforderung für die Analyse, Informationsextraktion und Interpretation für die zeitnahe Entscheidungsfindung während Vulkankrisen dar. Darüber hinaus erschweren die Komplexität der Eruptionsprozesse und Vorläuferaktivitäten die Analyse.

Eine Herausforderung bei der Untersuchung seismischer Signale vulkanischen Ursprungs ist die Koexistenz von transienten Signalschwärmen und lang anhaltenden vulkanischen Tremoren. Die Trennung dieser beiden Signaltypen kann daher dazu beitragen, unser Verständnis der zugrunde liegenden physikalischen Prozesse zu verbessern. Einige ähnliche Probleme (Datenreduktion, Quellentrennung, Extraktion und Klassifizierung) werden im Zusammenhang mit Music Information Retrieval (MIR, dt. Etwa Musik-Informationsabruf) behandelt. Die Signaleigenschaften von akustischen und seismischen Aufzeichnungen weisen eine Reihe von Gemeinsamkeiten auf. Ich gehe über die klassischen Signalanalysetechniken hinaus, die normalerweise in der Seismologie verwendet werden, indem ich die Ähnlichkeiten von seismischen und akustischen Signalen und das Fachwissen aus dem Gebiet der MIR zur Informationsgewinnung nutze.

Inspiriert von der Idee der harmonisch-perkussiven Trennung (HPS) in der musikalischen Signalverarbeitung habe ich eine Methode entwickelt, mit der harmonische vulkanische Erschütterungssignale extrahiert und transiente Ereignisse aus seismischen Aufzeichnungen erkannt werden können. Dies liefert ein sauberes Tremorsignal für die Tremoruntersuchung, sowie eine charakteristischen Funktion, die für die Erdbebenerkennung geeignet ist. Weiterhin habe ich unter Verwendung von HPS-Algorithmen eine Rauschunterdrückungstechnik für seismische Signale entwickelt. Diese kann zum Beispiel verwendet werden, um klarere Signale an Meeresbodenseismometern zu erhalten, die sonst durch zu starkes Rauschen überdeckt sind. Der Vorteil dieser Methode im Vergleich zu anderen Denoising-Techniken besteht darin, dass sie keine Verzerrung in der Breitbandantwort der Erdbebenwellen einführt, was sie für verschiedene Anwendungen in der passiven seismologischen Analyse zuverlässiger macht. Um Informationen aus hochdimensionalen Daten zu extrahieren und komplexe Eruptionsphasen zu untersuchen, habe ich ein fortschrittliches maschinelles Lernmodell entwickelt, aus dem ein umfassendes Signalverarbeitungsschema für vulkanische Erschütterungen abgeleitet werden kann. Mit dieser Methode können automatisch seismische Signaturen größerer Eruptionsphasen identifizieren werden. Dies ist nützlich, um die Chronologie eines Vulkansystems zu verstehen. Außerdem ist dieses Modell in der Lage, schwache vulkanische Vorläuferbeben zu erkennen, die als Indikator für bevorstehende Eruptionsaktivität verwendet werden könnten. Basierend auf den extrahierten Seismizitätsmustern und ihren zeitlichen Variationen liefere ich eine Erklärung für den Übergangsmechanismus zwischen verschiedenen Eruptionsphasen.

Acknowledgments

I would like to express my heartfelt thanks to my supervisors Fabrice Cotton and Matthias Ohrnberger for their invaluable guidance and support throughout my PhD journey. Fabrice is more than a supervisor; he is a wellspring of brilliant scientific ideas that surface even in our shortest discussions. He understands the demands of a PhD life and consistently supports his students with a perpetual smile. Matthias is ever-present, always ready to assist, lend an ear, and share his expertise. His support and infinite patience have provided me with the peace of mind I needed to accomplish my PhD. I am honored to have had the opportunity to have Frank Scherbaum as my mentor. I have always been amazed by his creative ideas and unique way of thinking. His boundless energy, perpetually youthful mind, great interest, and continuous encouragement are the best companions for any scientific project. Every word from him is a valuable lesson for me, and working with him is an asset for my entire academic life.

I would also like to extend my gratitude to my thesis committee members, Florent Brenguier and Conny Hammer, for their meticulous review of my thesis and their invaluable feedback. Additionally, I want to express my thanks to Frank Krüger and Eva Eibl for their participation on the committee, their insightful feedback, and the fruitful discussions.

During my PhD, I had the privilege of working with different people. I worked with Frank Krüger and Eva Eibl. I am deeply appreciative of the knowledge and experience I gained from them during this collaboration. Additionally, I had the chance to collaborate with Mostafa Mousavi, whose generous help and guidance in the final phase of my PhD left a significant impact on my academic journey. I would like to extend my appreciation to Sebastian Heimann for his assistance with coding and his willingness to address related questions. I am also grateful to Brigitte Knapmeyer-Endrun for the collaborative efforts and discussions we have had, which I hope to see extended in the future. I also want to thank my colleagues and friends Theresa Rein and Leila Ehsaninezhad for the great collaboration we had. Being positioned between two institutes, I could enjoy insightful discussions and engage in valuable social interactions with colleagues from both the Seismic Hazard and Risk Dynamics section at GFZ and the geophysics group at the University of Potsdam. I would like to thank all my colleagues and friends, especially Annabel Händel, for her ever-present kindness.

My PhD was primarily funded by the German Academic Exchange Service (DAAD) through the Graduate School Scholarship Program. I also had the benefit of being an associated member of the NatRiskChange group at the University of Potsdam. Additionally, I received support from both GFZ and the University of Potsdam for this work.

Lastly, I want to express my deepest gratitude to my loving and supportive family. Their love and belief have empowered me to pursue my goals. The confidence instilled in me by my parents enables me to approach any endeavor with the capability to overcome challenges.

Contents

List of Figures

List of Tables

Chapter 1

Introduction

Volcanic and magmatic activities have played a significant role in the formation of the Earth's crust today (Tilling, 1989). The dynamics of the crust and mantle can be closely linked to the activities and spatial distribution of volcanoes. About half of the volcanoes that erupted during Holocene time are classified as active volcanoes. On average, between 50 and 60 volcanoes (about one per week) erupt somewhere on Earth each year (Simkin et al., 1981). However, there may also be volcanoes with a dormant period of several centuries that are currently classified as dormant but could become active again. When a volcano erupts after a long dormant period, a great deal of energy is released (Tilling, 1989). Some of the most catastrophic eruptions in history occurred at volcanoes that were thought to be dormant and would not erupt again, such as the eruption of Mount Vesuvius in 79 AD, which destroyed the cities of Pompeii and Herculaneum (Sigurdsson et al., 1985), and the eruption of Mount Lamington (in Papua New Guinea) in 1951 (Taylor, 1958).

Volcanology, which emerged as a modern science in the early 20th century, not only provides an understanding of the physical processes in volcanic systems, which are among the most dynamic zones on the Earth and are responsible for many changes on our planet, but also helps scientists to anticipate the nature and timing of eruptions with varying degrees of certainty. Volcano monitoring aims to detect signs of change that herald the awakening or reawakening of a volcano and helps us to predict when a volcanic eruption will occur. The activity of a volcano is monitored by studying seismic activity, ground deformation, gas emission, and heat flow. Volcano seismology uses seismic signals to investigate the activities of the volcanoes. Seismic activity and volcanic tremors, which can be recorded in seismic waveforms, are among the main precursors to volcanic eruptions.

Volcanic tremors are persistent seismic signals that precede and/or accompany most volcanic eruptions (Konstantinou and Schlindwein, 2003). They have been identified as specific seismic signals that appear to be highly correlated with internal volcanic processes at active volcanoes, i.e., magma movement, fluid flow, or repeated rock failure. Volcanic tremors are therefore the most valuable source of information when it comes to understanding the physics of the forces that drive volcanic eruptions. Continuous monitoring of the properties of volcanic tremors, therefore, reveals the evolution of internal volcanic activity status and could therefore be useful in identifying seismic signal patterns that may be considered as precursors to catastrophic volcanic events.

Seismological station networks at active volcanoes continuously record ground motions. Such continuous recording could provide useful information for volcanic activity monitoring and operational eruption forecasting. Continuous characterization of tremor signals as recorded by seismic networks in the vicinity of active volcanoes is however still a major challenge for analysts. The challenge is to effectively and efficiently process such large-scale and high-dimensional seismic datasets. Automated approaches are needed to provide a complete and consistent record of event evolution. Moreover, volcanic tremors are usually hidden in the background of energy of transient signals such as earthquakes, especially during periods of high seismic activity preceding eruptions. Advanced signal processing techniques are then also needed to extract this signal from the seismic records to make the detailed investigation of volcanic tremor possible.

Similar issues (data reduction, extraction and classification) are addressed in the field of audio signal processing (ASP) or in the context of music information retrieval (MIR). The signal characteristics of acoustic and seismic recordings comprise a number of similarities. We aimed to introduce promising strategies and methods from ASP and MIR communities into a seismological processing scheme that deem to be useful for the seismological community. We (in this thesis, the use of "we" refers to the authors of the related paper) went beyond the classical signal analysis techniques commonly used in seismology by exploiting the similarities between seismic and acoustic signals, and built the information retrieval strategy based on expertise developed in the field of MIR and ASP. The goal was to develop an innovative seismological data processing scheme for volcanic tremor for the purpose of seismological monitoring and understanding the underlying physical source processes.

1.1 Purpose of the study: better understanding of volcanic processes

Continuous seismic recordings are required to monitor volcanic activity indirectly from seismic activity. To assess the evolution of a volcanic crisis, huge amounts of data must be automatically filtered for information related to volcanic processes, especially volcanic tremor signals. Therefore, there is a need for a reliable signal processing technique that can separate the signal of earthquakes and other transients from the volcanic tremor signals in the recorded seismic waveforms during periods of volcanic activity. When the volcanic tremor signal is separated from other signals in the seismic record, it provides important information about volcanic activities that can be used for various studies such as the source investigation of volcanic tremors. Our first goal in this PhD was then to develop an algorithm to automatically extract volcanic tremors from the seismic waveform (with reliable features such as true amplitude and phase).

Although the general frequency ranges of volcanic tremors are limited to [0.5-10] Hz (McNutt and Nishimura, 2008), tremors can have very different characteristics at different volcanoes and in different situations. As such, different groups of volcanic tremors indicate different processes in the volcanic system. The features of a volcanic tremor, such as its specific frequency, amplitude, and duration, are related to its formation mechanism. During a volcanic eruption, different patterns of volcanic tremor can be seen in the seismic waveform (see Figure 1.3). For the analysis of eruptive activities, it is then important to analyze these different patterns and identify similar/dissimilar families. Grouping volcanic tremors helps to investigate the changes in the magmatic and volcanic system. Finding similar groups in different time windows of the volcanic activity could contribute to detect the repetition of the same process. Expert classification by visual inspection is however generally difficult given the amount of data. Moreover, it is unclear what level of temporal consistency can be expected from such an analysis/classification process by an individual or a group of observers. The second goal in this PhD was to introduce an approach that can automatically group/cluster different volcanic tremors in the continuous seismic recordings.

1.2 Approach of the study: signal processing using both classical and machine learning techniques

Seismic waveforms and acoustic signals generated by musical instruments are similar in some respects (Schlindwein et al., 1995; Johnson and Watson, 2019) (see Figure 1.1). Extensive research in music information retrieval has led to paradigms (e.g., Müller, 2015) that were largely unknown in the seismology community but could offer great potential for improving

current seismological signal processing. Improving information extraction would lead to the discovery of unanticipated patterns and relationships that could result in advanced seismological monitoring and a better understanding of the underlying volcanic process.

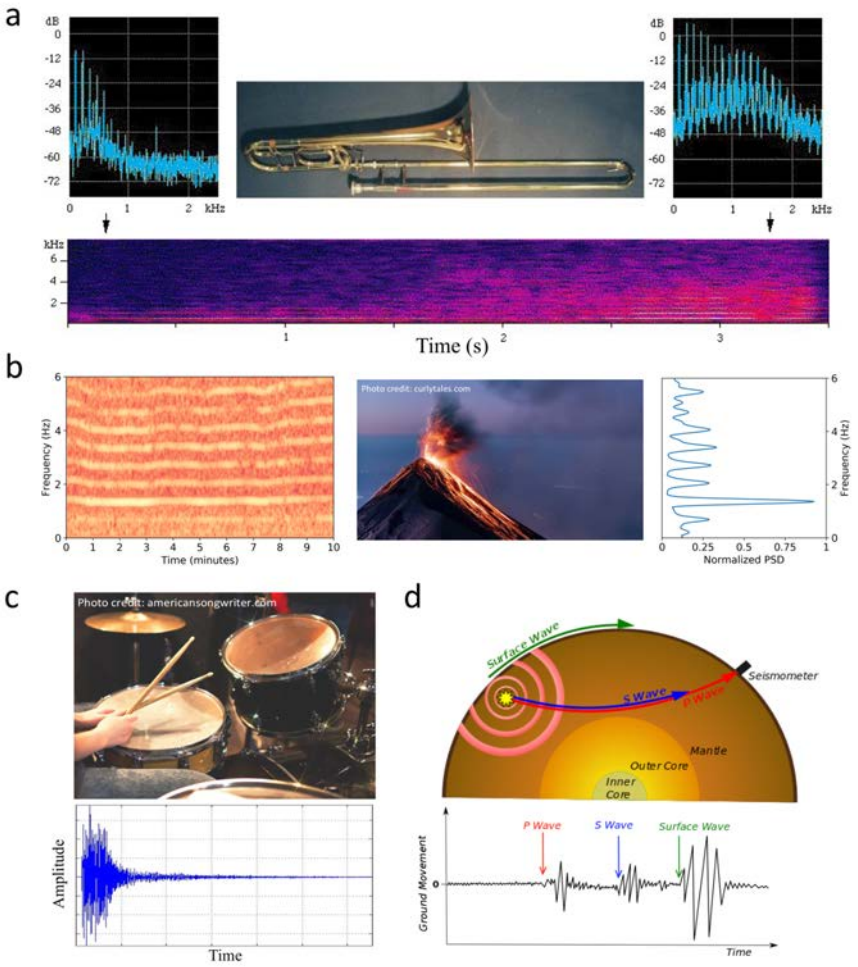

Figure 1.1. Similarities between musical and seismological signals. a, A trumpet producing harmonic sounds is shown. A harmonic spectrogram of the trumpet sound and spectrums related to two parts of the spectrograms are shown (picture from www.phys.unsw.edu.au). b, A volcano, a spectrogram of the harmonic volcanic tremor related to the period of volcanic unrest, and the power spectral density plot are shown. c, A drum which produce percussive sounds and an example of the generated signal are shown. d, The plot shows a seismic signal propagating through the earth and reaching the seismometer. An example of the seismic phases of an earthquake is also shown (Figure from www.esc.cam.ac.uk).

The continuously growing amount of seismic records makes detailed investigation of volcanic tremor signals challenging. Furthermore, in contrast to the significant amount of labeled earthquake signals, there are not many labeled volcanic tremor data. Labeled data are data that have already been assigned to a specific class by experts. For example, earthquake signals may be labeled as local or teleseismic events. Labeled data are needed for supervised machine learning algorithms. Due to the scarcity of labeled data sets for volcano monitoring, discrimination task studies in volcano seismology using machine learning were however limited to some classification approaches in supervised learning (Mousavi and Beroza, 2023). For example, Titos et al. (2019) and Lara et al. (2021) used inductive transfer learning by handwritten and natural images, respectively. The lack of labeled volcanic tremor signals, also favor the development and test of advanced clustering techniques based on unsupervised machine learning algorithms.

1.2.1 MIR in volcano seismology: volcanic tremor extraction and earthquake detection

Exploiting the idea of harmonic–percussive separation (HPS) from music information retrieval (MIR), we have developed an algorithm to separate the harmonic volcanic tremor signal from transient earthquake signals in the seismic waveforms. Harmonic–percussive separation methods decompose a signal into its harmonic and percussive components. The separation of harmonic and percussive components of sounds is of great interest in musical signal processing (e.g., Rafii and Pardo, 2011). Differences in the properties of harmonic and percussive sounds in the spectrogram domain (see Müller, 2015) enable this separation (FitzGerald and Gainza, 2010). Similarly, a seismic record of a volcano consists of (harmonic) volcanic tremors and transient signals. Long-lasting volcanic tremor signals, which last minutes to days and have a limited frequency range (0.5-10 Hz according to McNutt and Nishimura, 2008), contrast with transient seismic signals such as earthquakes, which have a broader frequency range (less than one thousandth Hz up to about 100 Hz). We then use the idea of HPS from the field of musical signal processing and bring it to the field of seismological signal processing. Figure 1.2 shows HPS both in the music and in the seismic domains.

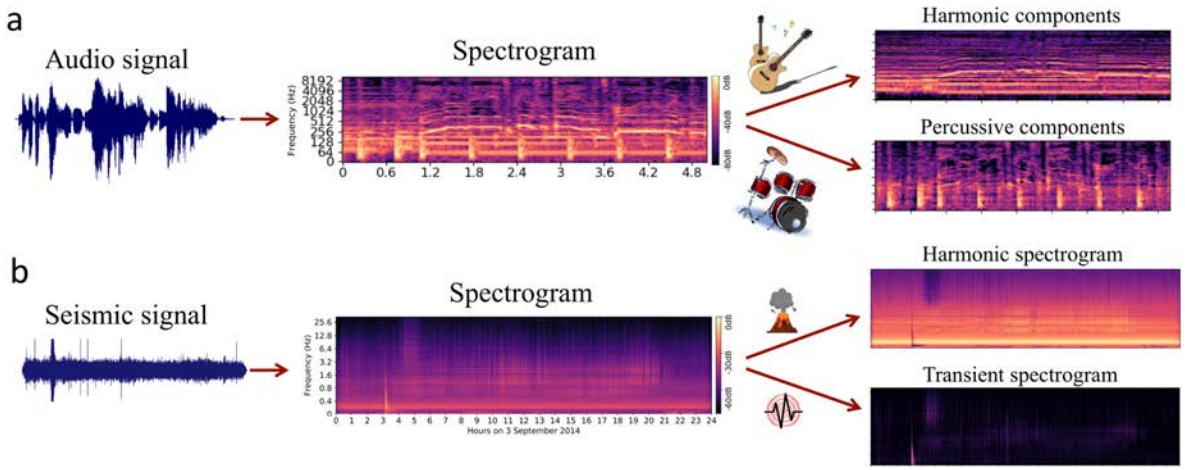

Figure 1.2. Harmonic-percussive separation in music/audio (a) and seismic (b) domains. The signal and spectrogram in (b) are related to the 2014-2015 Holuhraun eruption in Iceland. Using HPS it is split into two spectrograms; one shows harmonic patterns corresponding to volcanic tremors and the other shows transient patterns corresponding to earthquake signals. In subfigure a, Spectrograms are from Librosa.org and the instruments are from http://mir.ilsp.gr.

We have developed an algorithm based on a combination of two HPS techniques. In the first technique, we search for similarities in the time frames of the spectrogram using a similarity matrix (Rafii and Pardo, 2012) to detect repeating patterns. The similarity matrix calculates the cosine similarity between the time frames in the Short Time Fourier Transform (STFT) spectrogram. We separate the spectrogram into two spectrograms of repeating and non-repeating patterns. In the second technique, we use two sets of horizontal and vertical median filters to enhance the harmonic and percussive components, respectively (FitzGerald, 2010). This second technique allows us to remove the remnants of the percussive components from the repetitive spectrogram using a horizontal median filter and obtain a clean spectrogram consisting of harmonic patterns. Applying a vertical median filter to the non-repeating spectrogram results in a spectrogram with the percussive components. By inverting the STFT of the harmonic spectrogram, we extract the clean signal of the volcanic tremor. We use the percussive spectrogram to create a characteristic function suitable for detecting transient signals. Since the seismic waveforms are usually earthquakes, this function is used to detect

earthquakes. It is capable of detecting even small seismic events.

In the related work (Chapter 2), we evaluate the algorithm using real and semi-synthetic data for tremor extraction and earthquake detection. We measure the cross-correlation of the extracted tremor signal with different signal-to-noise ratios (SNR). The challenge of detecting long-period (LP) events with a longer duration narrowband signals compared to short duration broadband volcano-tectonic events is discussed. The result of this study provides a clean volcanic tremor signal that can be used in various studies related to eruptive activity analysis. At the same time, a technique for detecting earthquakes is presented.

1.2.2 MIR in denoising seismological data: noise reduction without earthquake distortion

The application of harmonic–percussive separation in seismological signal processing is not limited to volcanological studies. The separation of signals with different characteristics and sources is a general problem in signal processing and has applications in many scientific fields. A seismic waveform is created by the superposition of all the vibrations (energies) present at the location of the seismometer and these signals can be generated by a large variety of sources. Seismologists are interested in specific signals associated with specific processes in the earth, such as earthquakes, volcanic eruptions, and landslides. They are also interested in seismic noise, which is a relatively persistent vibration of the ground that contaminates seismic data. Seismic noise can be used for seismic imaging and monitoring (e.g. Brenguier et al., 2019 & Takano et al., 2019). It may happen that the signal of interest is completely masked by other signals due to low SNR. Separating the signal of interest from other signals in seismic records is required for a better study of the signals. Removing or reducing the energy of unwanted signals is known as the noise reduction problem.

Noise reduction results in a higher SNR of the interested signal. Detecting earthquake arrival time can for example benefit from such noise reduction since seismic phase arrivals have higher SNR in the denoised signals. There are various techniques for denoising seismic signals (e.g. Mousavi and Langston, 2017; An et al., 2021; Negi et al., 2021). Most noise reduction techniques introduce some sort of waveform changes to the interested signal. The new generation of deep learning based noise reduction algorithms can significantly improve the SNR of the interested signal (e.g. Zhu et al., 2019) and cause minimal changes in the signal. For detection tasks, small waveform changes are acceptable for detecting the arrival times. However, for other types of studies, the exact amplitude and frequency content of the analyzed signals are important. In particular, many passive seismological methods, such as the calculation of receiver functions or surface wave dispersion and polarization analysis, are based on the analysis of undistorted broadband waveforms. Preserving the earthquake signal from distortion after denoising is then crucial in seismology in particular, for Ocean Bottom Seismometer (OBS) data analysis. OBSs are indeed often more contaminated by noise compared to land stations, especially on the horizontal components. Previous studies on OBS noise reduction suggested different approaches to remove low-frequency noises from OBS recordings but mainly focused on the vertical component (Crawford and Webb, 2000; Bell et al., 2015). The records of horizontal components, which are needed for the analysis of body and surface waves, could not be much improved by previous analysis in the teleseismic frequency band.

We introduce a noise reduction method based on harmonic–percussive separation algorithms. Here, percussive components correspond to earthquake signals and harmonic components

correspond to noise signals. Our method separate long-lasting narrowband signals from broadband transients in the OBS signal and retrieve “cleaner” broadband earthquake waveforms. The method significantly reduces noise from OBS records on both the vertical and horizontal components and increases the earthquake SNR. This algorithm doesn’t introduce distortion to the broadband earthquake waveforms. This method can also be used in seismic noise studies by removing transient signals such as earthquakes from seismic recordings.

In the related paper (Chapter 3) besides presenting the method in details, we discuss the properties of noise signals, which are eligible for our noise reduction algorithm. We test the algorithm with both synthetic and real signals. We finally apply the algorithm, compare its efficiency with other noise reduction techniques and show the improvements for SH waves, surface waves (e.g. Love-wave group velocity analysis) and Receiver functions analysis.

1.2.3 Machine learning: feature extraction and clustering of high-dimensional volcanic tremor signals

Seismology is a data-rich and data-driven science. The application of machine learning (ML) techniques in seismology has a decades-long history (e.g., Dowla et al. 1990, Turhan Taner et al. 1988), however, it has been growing rapidly in the past few years (Beroza et al., 2021). ML is a branch of artificial intelligence (AI), that imitates the way that humans learn using data and algorithms and gradually improves its accuracy. Rapidly expanding seismological data volumes and the need for automated and fast algorithms for data analysis, information extraction, and interpretation have motivated scientists to develop various efficient algorithms for different seismological tasks. In recent years, considering the availability of massive labeled datasets in seismology deep learning has entered almost every subfield of seismology, outperformed classical approaches for many seismological tasks, and came to the forefront of seismological research (Mousavi and Beroza, 2022).

Deep learning can be used in semiology to discover patterns in continuous seismic records and has great potential for uncovering new insights in the data. Many deep leaning-based algorithms have been developed for various seismological studies such as seismic event discrimination (e.g. Mousavi et al., 2019 & Nakano et al., 2019 & Peng et al., 2020), seismic denoising (Kaur et al., 2020 & Saad and Chen, 2020 & Zhang et al., 2019), ground motion modeling (e.g. Khosravikia et al., 2019 & Lilienkamp et al., 2022), and ground motion characterization (e.g. Esfahani et al. 2021 & Esfahani et al., 2023). However, due to the scarcity of large-scale labeled volcanic datasets and the complexity of signals in volcanic activities, the application of deep learning in volcano seismology has been challenging.

Unsupervised learning is a ML technique that learns patterns from unlabeled data. This can be very useful in volcano seismology where there are not enough labeled data. Also, unsupervised learning can discover previously unknown patterns in data, which is not possible in supervised machine learning models. Clustering is a branch of unsupervised learning methods that partitions unlabeled data into groups of similar patterns. Grouping seismic signals of volcanic activity with similar patterns could provide the potential for a deeper understanding of the volcanic processes. In my third paper (Chapter 4) we worked on this problem and used seismic signals and machine learning algorithms. Figure 1.3 shows three months of the seismic signal during the 2021 Geldingadalir eruption and examples of different patterns that are seen in the seismic waveform.

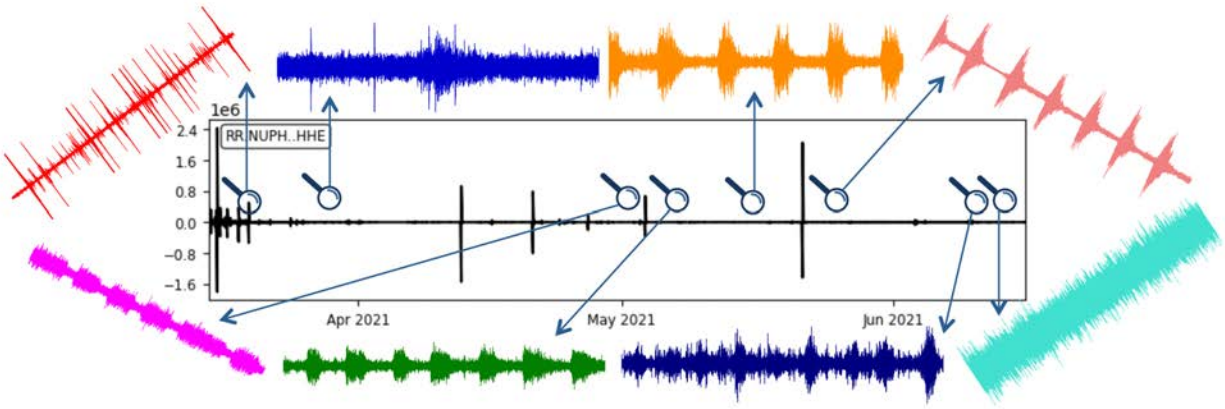

Figure 1.3. Different signals observed in the seismic record. Three months of the seismic signal during the 2021 Geldingadalir eruption and some of the patterns which are seen in the seismic waveform. Each colored signal has a duration of one hour.

Clustering high-dimensional data is computationally expensive and its effectiveness decreases as the dimension of data increases (Steinbach et al., 2004). Dimensionality reduction and feature extraction are useful before clustering of high dimensional data so the clustering will be done on feature space instead of data space. The ability of deep neural networks to automatically learn clustering-friendly features improves clustering performance (e.g. Xie et al., 2016 & Yang et al., 2017). We use an unsupervised deep learning technique named deep embedded clustering (DEC) which uses the latent representation of data extracted using an autoencoder for the clustering task (Xie et al., 2016). Autoencoders are neural networks that learn to compress their input data in the encoder part and decompress it in the decoder part (Vincent et al., 2010). The encoder learns to map the input to a latent representation through automatic feature extraction and a nonlinear transformation. The decoder reconstructs the input from the hidden representation by minimizing the reconstruction loss.

In the related paper (Chapter 4) we present our model, which consists of an autoencoder and a clustering layer attached to it. We discuss different aspects of the method and related parameters. We show some important findings about the volcanic activity that have resulted from our model. We reveal different eruptive phases, present an interpretation of the system changes mechanisms and discuss the possible precursors to the eruption.

1.3 Scope of this thesis

The signal processing algorithms and models developed in this thesis are all motivated by a same question: How can these techniques and models improve our understanding of the solid Earth? This question was my main driver to develop this thesis works and this study contributes to advancements in the understanding of volcanic processes.

Chapter 2 explains how we are inspired by the similarity between seismic and acoustic signals and bring advances from the field of MIR into the seismological signal processing domain. We exploit some of the algorithms in MIR, modify and tune them to be applicable to seismic data. Such new methods are specifically useful for the analysis of seismic waveforms in volcanic areas. We develop an algorithm based on harmonic–percussive separation (HPS) technique. In this chapter, we show how our algorithm contributes to a better understanding of volcanic processes.

Chapter 3 shows how source separation can be useful in the noise reduction of seismic data. We develop an algorithm, which is again derived from the idea of HPS. The advantage of this denoising technique is discussed in this chapter. We apply this algorithm and show how it can improve OBS data studies and contribute to better image of the Earth subsurface.

In Chapter 4 we extend our analysis of volcanic seismic waveform by using machine learning techniques. We develop an original unsupervised clustering technique for volcanic tremors. We show how our model can extract salient features from the seismic waveform. Clustering volcanic tremors using the extracted features helps to reveal different eruptive phases, which are exhibited through different patterns in the seismic signal. We finally discuss the detection of overlooked patterns in the seismic signal and the possible contribution of this new method to the forecast of volcanic eruptions.

Chapter 5 presents and discusses the main results of the previous chapters. Chapter 6 finalizes the thesis with conclusions and outlooks.

1.4 Author's publication and contributions

1. Chapter 2:
   Published as: **Zali**, Z., Ohrnberger, M., Scherbaum, F., Cotton, F., & Eibl, E. P. (2021). Volcanic Tremor Extraction and Earthquake Detection Using Music Information Retrieval Algorithms. *Seismological Research Letters*, 92(6), 3668-3681. https://doi.org/10.1785/0220210016
   Z.Z. initiated the study conception and design, developed the algorithm and conducted real and synthetic tests. Z.Z., M.O., F.S., and F.C. evaluated and discussed the results. The first manuscript draft was written by Z.Z. All the authors contributed to the writing of the final manuscript.

2. Chapter 3:
   Published as: **Zali**, Z., Rein, T., Krüger, F., Ohrnberger, M., & Scherbaum, F. (2023). Ocean bottom seismometer (OBS) noise reduction from horizontal and vertical components using harmonic–percussive separation algorithms. *Solid Earth*, 14(2), 181-195. https://doi.org/10.5194/se-14-181-2023
   Z.Z. developed the algorithm and designed the study. T.R. created the synthetic data, conducted the synthetic tests, and measured the receiver functions. F.K. conducted the group velocity analysis. Z.Z., T.R., and F.K. evaluated the results. Z.Z. and T.R. wrote the initial draft. All authors wrote the final paper and discussed the results.

3. Chapter 4:
   Submitted as: **Zali**, Z., Mousavi, S. M., Ohrnberger, M., Eibl, E. P., Cotton, F. Tremor clustering reveals precursors and evolution of the 2021 Geldingadalir eruption.
   Z.Z. initiated the study conception and design. Z.Z. developed the algorithm and S.M.M. contributed to the algorithm improvement. The first manuscript draft was written by Z.Z. All the authors contributed to the evaluation and discussion of the results and the writing of the final manuscript.

1.5 Open software publications

1. Zahra **Zali**. (2022a). TremorExtractor-EqDetector (v1.0.0). Zenodo. https://doi.org/10.5281/zenodo.7339603

Codes related to the algorithm in the first paper (Chapter 2) are freely available in my GitHub page. Users can simply run the code for their data. The input for this code is seismic record and the output will be the extracted volcanic tremor and a characteristic function, which can be used to automatically detect earthquake in the seismic record.

2. Zahra **Zali**. (2022b). ZahraZali/NoiseCut: NoiseCut (v1.0.0). Zenodo. https://doi.org/10.5281/zenodo.7339552

Codes related to the noise reduction technique presented in the second paper (Chapter 3) are freely available in my GitHub page. Furthermore, I created a python package named "NoiseCut" for denoising seismic signals based on my algorithm. NoiseCut can be easily installed in Python and simply be imported and run. It is totally automated. Therefore, it is not only useful for experts but also for users with no specific knowledge about coding or the algorithm. NoiseCut is also available as a tool in the Snuffler that eases its application for the Snuffler users. Snuffler is a seismogram browser and workbench based on Pyrocko.

1.6 Further relevant contributions

I have contributed to the two blow researches of other PhD students. I improved data by source separation and noise reduction. My work improved these studies significantly. The results are presented at the scientific conferences, which are mentioned below. The manuscripts are in preparation.

1. Theresa Rein, Zahra **Zali**, Frank Krüger, and Vera Schlindwein. "Receiver Function analysis of noise reduced OBS data recorded at the ultra-slow spreading Knipovich Ridge." In EGU General Assembly Conference Abstracts, pp. EGU22-3755. 2022. DOI: 10.5194/egusphere-egu22-3755

In this study I denoised seismic data of my colleague using my noise reduction technique, which is presented in Chapter 3. The analysis of the receiver functions shows that noise level below 1 Hz on all seismogram components significantly reduces using our techniques. Here the SNR increases by up to 3,7. The increased SNR on the denoised data allows for more reliable receiver function calculations and interpretations.

2. Leila Ehsaninezhad, Christopher Wollin, Zahra **Zali**, Charlotte M. Krawczyk Denoising of Rayleigh Waves to improve DAS processing of urban noise. Submitted abstract to IUGG 2023 conference.

This study analyses cultural noise along an urban road in Berlin using Distributed Acoustic Sensing (DAS) data. The goal is to image the subsurface using ambient noise as a source of excitation and DAS as sensors. Seismic noise in urban areas is complex and often of anthropogenic nature and dominated by traffic. The acquisition of long time series is needed to extract coherent signals from recorded noise. The recorded noise contains transient signals with frequencies between 1 to 40 Hz, which is related to the passage of trains. Considering the high energy of these signals the extraction of coherent Rayleigh Waves is complicated. I modified my noise reduction technique to be useful for denoising DAS data from transient noises. This method is based on harmonic–percussive separation techniques. Here I remove percussive or

transient signals (related to train passage) from the data. The comparison of results using original and denoised data shows that applying the denoising approach results in improved virtual shot gathers. This could imply the possibility of conducting shorter campaigns for acquiring equivalent results with respect to ambient noise analysis.

Chapter 2

Volcanic Tremor Extraction and Earthquake Detection using Music Information Retrieval Algorithms

Abstract

Volcanic tremor signals are usually observed before or during volcanic eruptions and must be monitored to evaluate the volcanic activity. A challenge in studying seismic signals of volcanic origin is the coexistence of transient signal swarms and long-lasting volcanic tremor signals. Separating transient events from volcanic tremors can, therefore, contribute to improving upon our understanding of the underlying physical processes. Exploiting the idea of harmonic–percussive separation in musical signal processing, we develop a method to extract the harmonic volcanic tremor signals and to detect transient events from seismic recordings. Based on the similarity properties of spectrogram frames in the time–frequency domain, we decompose the signal into two separate spectrograms representing repeating (harmonic) and nonrepeating (transient) patterns, which correspond to volcanic tremor signals and earthquake signals, respectively.

We reconstruct the harmonic tremor signal in the time domain from the complex spectrogram of the repeating pattern by only considering the phase components for the frequency range in which the tremor amplitude spectrum is significantly contributing to the energy of the signal. The reconstructed signal is, therefore, clean tremor signal without transient events.
Furthermore, we derive a characteristic function suitable for the detection of transient events (e.g., earthquakes) by integrating amplitudes of the nonrepeating spectrogram over frequency at each time frame. Considering transient events like earthquakes, 78% of the events are detected for signal-to-noise ratio = 0.1 in our semisynthetic tests. In addition, we compared the number of detected earthquakes using our method for one month of continuous data recorded during the Holuhraun 2014–2015 eruption in Iceland with the bulletin presented in Ágústsdóttir et al. (2019). Our single station event detection algorithm identified 84% of the bulletin events. Moreover, we detected a total of 12,619 events, which is more than twice the number of the bulletin events.[a]

[a] Published as: Zali, Z., Ohrnberger, M., Scherbaum, F., Cotton, F., & Eibl, E. P. (2021). Volcanic Tremor Extraction and Earthquake Detection Using Music Information Retrieval Algorithms. *Seismological Research Letters*, 92(6), 3668-3681. https://doi.org/10.1785/0220210016

2.1. Introduction

Volcanic tremors are long-lasting low-frequency seismic signals that frequently precede or accompany volcanic eruptions (McNutt, 1992). They can reveal information about eruptive activities (Alparone et al., 2003; Eibl, Bean, Jónsdóttir, et al., 2017; Eibl, Bean, Vogfjörd, et al., 2017) and are one of the most commonly studied signals in volcano seismology (Falsaperla et al., 2005) for use in eruption forecasting as well as investigating the physics of the underlying volcanic processes (Chouet, 1996; Yukutake et al., 2017).

Despite different hypothesis about the generation mechanisms of volcanic tremors, the details are not yet well understood (Davi et al., 2012; Eibl, Bean, Jónsdóttir, et al., 2017), and a variety of physical processes may explain the seismological evidence observed so far (Hellweg, 2000). Volcanic tremor signals are usually seen in the seismic records alongside many tectonic earthquakes or other transient signals occurring during a period of volcanic unrest (Dmitrieva et al., 2013; Hotovec et al., 2013; Eibl, Bean, Vogfjörd, et al., 2017), affecting the observability of the tremor signal. Both volcanic tremors and earthquakes may help better understand the underlying physical processes of volcanic eruptions; however, the superposition of signals makes it challenging to study the details of each signal separately. A reliable signal processing operation is, thus, required to separate earthquakes as well as other transient signals from the volcanic tremor signals in the recorded seismic waveforms during periods of volcanic unrest. There have been attempts in terms of the detection and discrimination of volcanic tremor and tectonic earthquake signals in previous studies. For example, an automatic P- and S-wave detection was used in Rouland et al. (2009) to identify volcanic tremors as events containing only P-type wave, and tectonic earthquakes containing both P and S waves. However, this study introduces for the first time the topic of extracting tremor signals from seismic waveforms and reconstructing the volcanic tremor signal with related phase information.

Inspired by similarities of seismic and acoustic signals, we take advantage of the expertise developed in the field of music information retrieval (MIR) and audio signal processing. A seismic waveform is the record of the Earth vibrations, which, in terms of signal properties and generation mechanism, can be seen to be similar to sound signals generated by musical instruments (including the human voice) (Schlindwein et al., 1995; Johnson and Watson, 2019). Exploiting the extensive research results in MIR (e.g., Müller, 2015), we have developed a seismological data processing scheme for the purpose of separating volcanic tremor signals from transient signals generated during a volcanic crisis.

The separation of harmonic and percussive components of sound is of great interest in musical signal processing (e.g., Rafii and Pardo, 2011). Pop music, for example, often consists of a repetitive percussive background and a vocal foreground, which is locally nonrepetitive (FitzGerald, 2012). In this type of music, the different characteristics of harmonic and percussive sounds in the spectrogram domain (see Müller, 2015) allow a separation of foreground vocals from the more percussive background sound (FitzGerald and Gainza, 2010). Similarly, a seismic waveform during an eruption may consist of (harmonic) volcanic tremor signals over which transient seismic signals are superimposed. The long-duration volcanic tremor signal that lasts minutes to days with a restricted frequency range (1–9 Hz according to McNutt, 1992) contrasts with transient seismic signals such as earthquakes with a wider range of frequencies (0.1–30 Hz in this study). In particular, harmonic volcanic tremor signals with distinct spectral lines are readily distinguishable from transient, short-duration (seconds) seismic events in the time–frequency domain. In musical signal processing, the goal of harmonic–percussive source separation is to decompose an input signal into the sum of two

signals— one consisting of all harmonic components and the other of all percussive components (Müller, 2015). The same algorithms could be implemented in the seismology domain to decompose a seismic signal into its harmonic components (harmonic volcanic tremors) and percussive components (transient events such as earthquakes). In musical signal processing, several methods for harmonic–percussive separation (HPS) have been suggested (Müller, 2015).

Here, in the first step of our method, we adopted the repetition/similarity (REPET-SIM) method (Rafii and Pardo, 2012; Rafii et al., 2014) to separate volcanic tremors from transient earthquakes. The advantage of this method is its ability to process music pieces with quickly varying repeating structures without the need to identify periods of the repeating structure beforehand. The approach evaluates the underlying repeating structure by looking for the similarities in the spectrogram time frames. This repeating part of the signal is then subtracted from the original spectrogram. The remaining time frames contain the percussive events. We use this approach and apply it to seismic data collected from a volcano. In this setting, repeating structures, which result in a harmonic spectrum, correspond to volcanic tremors and percussive (nonrepeating and impulsive) elements corresponding to transient events such as earthquakes. Another method similar to REPET-SIM for HPS was proposed by FitzGerald (2010), which we use in the second step of our method to remove remaining percussive components in the repeating spectrogram and vice versa.

The remainder of this paper is organized as follows. In the Method section, we describe existing methods in MIR for our problem (see the HPS Algorithms section) and explain how we developed our method based on these algorithms. Modifications to and the application of the REPET-SIM method (Rafii and Pardo, 2012; Rafii et al., 2014) and the HPS using median filtering (FitzGerald, 2010) for extracting seismic tremor signals are outlined in the Volcanic Tremor Extraction Approach section, whereas the Transient Signal Detection and Timing Estimation section describes the detection and timing of the remaining transient events (e.g., earthquakes). The Parameters Selection section outlines the selection of the method's parameters. The Datasets and Testing section presents the generation of semisynthetic data (see the Generation of Semisynthetic Data section), an evaluation of the proposed method based on a semisynthetic test on tremor extraction (see the Testing the Tremor Extraction Algorithm Using Semisynthetic Data section) and earthquake detection (see the Testing the Earthquake Detection Algorithm Using Semisynthetic Data section), as well as real data tests (see the Real Data Tests section). The feasibility of the method with respect to processing speed is discussed in the Feasibility of the Method with Respect to Processing Speed section. In the Conclusions and Outlook section, we discussed the results and provided our conclusions about the applicability of the method.

2.2 Method

2.2.1 HPS algorithms

HPS as an application of musical source separation (Cano et al., 2018) has attracted significant attention in MIR research in recent years (Rafii et al., 2018). HPS algorithms are based on the different characteristics of harmonic and percussive components in a music signal.

Harmonicity expresses the situation in which the complete signal can be seen as the superposition of spectral components (partials) for which frequencies are all integer multiples of a fundamental frequency. Harmonics form stable horizontal ridges in a short-time Fourier

transform (STFT) spectrogram, which means constant frequencies exist along the time axis. A percussive (impulsive) sound is short and similar to the sound of hitting a drum. Percussive signals form vertical ridges in an STFT spectrogram, corresponding to the existence of different frequencies in an instant, that is, a broadband characteristic of short duration.

To separate harmonic and percussive elements, one simple approach is to apply a median filter to the STFT spectrogram of the signal (FitzGerald, 2010). Median filters are usually used to remove noisy parts of a signal by replacing each sample by the median value determined from the neighboring samples within a specific window. Within the HPS, a median filter applied along the horizontal axis of the spectrogram (time) suppresses "short-lived" broadband percussive components interrupting the long-lasting horizontal narrowband ridges. This results in a "denoised" harmonic spectrogram. Similarly, applying a median filter along the vertical axis of a spectrogram (frequency) emphasizes short-lived broadband features, while suppressing long-lasting narrowband horizontal frequency lines (harmonic components) and results in a "denoised" percussive spectrogram. These two median filters are used separately to generate the related spectrograms with dominant harmonic or percussive content, respectively.

Another promising approach for our purpose is REPET-SIM, which treats repetition as a basic property in generating and perceiving structure in music (Rafii & Pardo 2012; Rafii et al., 2014). The main step in this method is to identify similar patterns using a calculated similarity matrix. Given a music signal, first its complex STFT is calculated, which is named X here. Considering V as the amplitude spectrogram V = |X|, the similarity matrix S is calculated to measure the cosine similarity (the similarity between two vectors of an inner product space) between time frames of the spectrogram V. As shown in equation (2.1), the cosine similarity is calculated through the multiplication of the transposed V by V with normalization of the V time frames.

$$S(j_a,\mathrm{j}_b) = \frac{\sum_{\mathrm{i}=1}^{n} V(\mathrm{i},\mathrm{j}_a)V(\mathrm{i},\mathrm{j}_b)}{\sqrt{\sum_{\mathrm{i}=1}^{n} V(\mathrm{i},\mathrm{j}_a)^2}\sqrt{\sum_{\mathrm{i}=1}^{n} V(\mathrm{i},\mathrm{j}_b)^2}} \tag{2.1}$$

where $\forall j_a,\mathrm{j}_b \in [1,\mathrm{m}]$, where m is the number of time frames and n equaling $N/2+1$ is the number of frequency channels for each time frame of length N (samples). $S(j_a,j_b)$ is then the cosine similarity between the time frames j_a and j_b of the spectrogram V.

For all the frames j in V, similar frames are identified using a threshold in the similarity matrix and stored in an array J. A repeating spectrogram model (W) is then derived using the similar frames. For all the frames j, the corresponding frame in W is derived by taking the median of J for each frequency. Repeating time-frequency bins are captured by the median and build the repeating spectrogram model W. A refined repeating spectrogram model W' is created by taking the minimum between W and V. The rationale is that the non-negative spectrogram V is the sum of two non-negative spectrograms of repeating and non-repeating patterns, hence, W is less than or at most equal to V.

In the following, a time-frequency mask M is derived by normalizing W' by V. Time-frequency bins with repeating patterns will have values close to 1 in M and time-frequency bins without repeating patterns will have values close to 0. The mask M is applied to STFT X and the repeating spectrogram will be created. Finally, the harmonic signal in music is obtained by inverting the repeating spectrogram into the time domain. The percussive signal is obtained by subtracting the harmonic signal from the input signal (Rafii & Pardo 2012).

2.2.2 Volcanic tremor extraction approach

Among the different tremor observations in volcanic seismology, the so-called harmonic tremor is a special signal showing a band-limited harmonic spectrum. It has been observed at many volcanoes and has been reported often during times of increased volcanic activity, and is thought to be connected to fluid flow or (de-)pressurization of the volcanic system (e.g., Montegrossi et al., 2019). This is the motivation for using HPS algorithms to separate harmonic volcanic tremor signals from earthquake signals representing the percussive event type. Being able to extract this special kind of tremor signal from seismic waveforms provides the opportunity to improve the observations and analyses of harmonic tremors. In particular, extracting low-amplitude harmonic tremor signals that are hidden in the background seismic noise or overprinted by earthquake sequences accompanying volcanic activity may allow new insights into the generation processes and their relationships to volcanic eruptive activity.

In this study, we analyze the seismic waveforms of the Holuhraun 2014–2015 eruption in Iceland (FLUR station from network 7Z; White, 2010) to separate the harmonic and percussive components. Figure 2.1 shows the eruption site and the station location in Iceland with an example of one day of seismic waveforms (Figure 2.1a,b), the power spectral density (PSD), and the spectrogram (Figure 2.1c,d). The PSD and spectrogram of the extracted harmonic components are shown in Figure 2.1e,f.

Our method is derived from a combination of the REPET-SIM method (Rafii and Pardo, 2012; Rafii et al., 2014) and the HPS algorithm given by FitzGerald (2010), after tuning parameters to adapt it to seismic data. For building our method, we used Librosa—a Python package for audio and music signal processing (McFee et al., 2020). Furthermore, we implement a phase reconstruction procedure for the volcanic tremor signal. A detection algorithm for earthquakes as transient signals has been derived as a by-product of the applied processing.

The REPET-SIM, as described in section 2.2.1, is used to create a similarity matrix and to derive a time-frequency model of repeating patterns. We derive the non-repeating spectrogram model by subtracting W' from V. Once the model spectrograms are calculated, they are used to derive two time-frequency masks for repeating and non-repeating patterns.

We modified the REPET-SIM algorithm by using a soft mask via Wiener filtering (Vaseghi, 1998) instead of a binary mask. The calculation of the soft mask M1 and M2 are shown below as equations (2.2) and (2.3):

$$M1_{n.m} = \frac{{W'}_{n,m}{}^{P}}{{W'}_{n,m}{}^{P} + \left(V_{n,m} - {W'}_{n,m}\right)^{P}} \tag{2.2}$$

$$M2_{n.m} = \frac{\left(V_{n,m} - {W'}_{n,m}\right)^{P}}{\left(V_{n,m} - {W'}_{n,m}\right)^{P} + {W'}_{n,m}{}^{P}} \tag{2.3}$$

where M1 is a repeating mask and M2 is a non-repeating mask. A power factor *P* is applied to the model spectrograms to further enhance the signal-to-noise ratio. We use a power factor of 2 in our calculations.

Once we have constructed the masks, we multiply them with the input amplitude spectrograms to separate the components. Equation (2.4) shows the element-wise multiplication of the repeating mask (M1) and the input amplitude spectrogram (V).

$$\mathrm{R}=\mathrm{M1}\otimes\mathrm{V}, \tag{2.4}$$

where R denotes the repeating amplitude spectrogram. The same element-wise multiplication operation is applied for the non-repeating mask and the input amplitude spectrogram as it is shown is equation (2.5):

$$\mathrm{NR}=\mathrm{M2}\otimes\mathrm{V}, \tag{2.5}$$

where NR denotes the non-repeating amplitude spectrogram.

From this we obtain two spectrograms, one for repeating patterns and one for non-repeating patterns. The harmonic and percussive components of the signals are then separated into their respective masked spectrograms, although small traces of percussive components are still visible in the repeating spectrogram, whereas remnants of the harmonic components can be recognized in the non-repeating spectrogram. Therefore, a second HPS approach is subsequently applied to the resulting spectrograms from the first processing step by using the median filtering method of FitzGerald (2010). In particular, we use median filtering along the time axis, enhancing the harmonic components within the spectrogram. Applying another median filtering along the frequency axis results in a denoised spectrogram of the percussive components. Following the above notation, each spectrogram of R and NR will be decomposed into two spectrograms of their harmonic and percussive components. Equation (2.6) and (2.7) show this separation:

$$R = H1 + P1, \tag{2.6}$$

$$NR = H2 + P2, \tag{2.7}$$

where H1 and P1 are harmonic and percussive components of the repeating spectrograms, and H2 and P2 are harmonic and percussive components of the non-repeating spectrograms. We create a soft mask using H1 and multiply it the R spectrogram, which results in the final harmonic spectrogram, which we name HARM. Another soft mask is created using P2 and is multiplied by the NR spectrogram to derive the final transient spectrogram that we have named TRAN (see Figure 2.2).

Figure 2.2 shows the flowchart of the method with an example of a seismic waveform from 3 September 2014 during the Holuhraun 2014-2015 eruption in Iceland (FLUR station from network 7Z (White, R. 2010)). On this day we were 4 days into a 6-month long fissure eruption accompanied by tremors and long-period and volcano-tectonic earthquakes (Eibl et al. 2017a). For further details on the background of the Holuhraun eruption event, the reader is referred to Sigmundsson et al. (2015) and Gudmundsson et al. (2016). For details on the events on 3 September 2014, the reader is referred to Eibl et al. (2017a) and Woods et al. (2018).

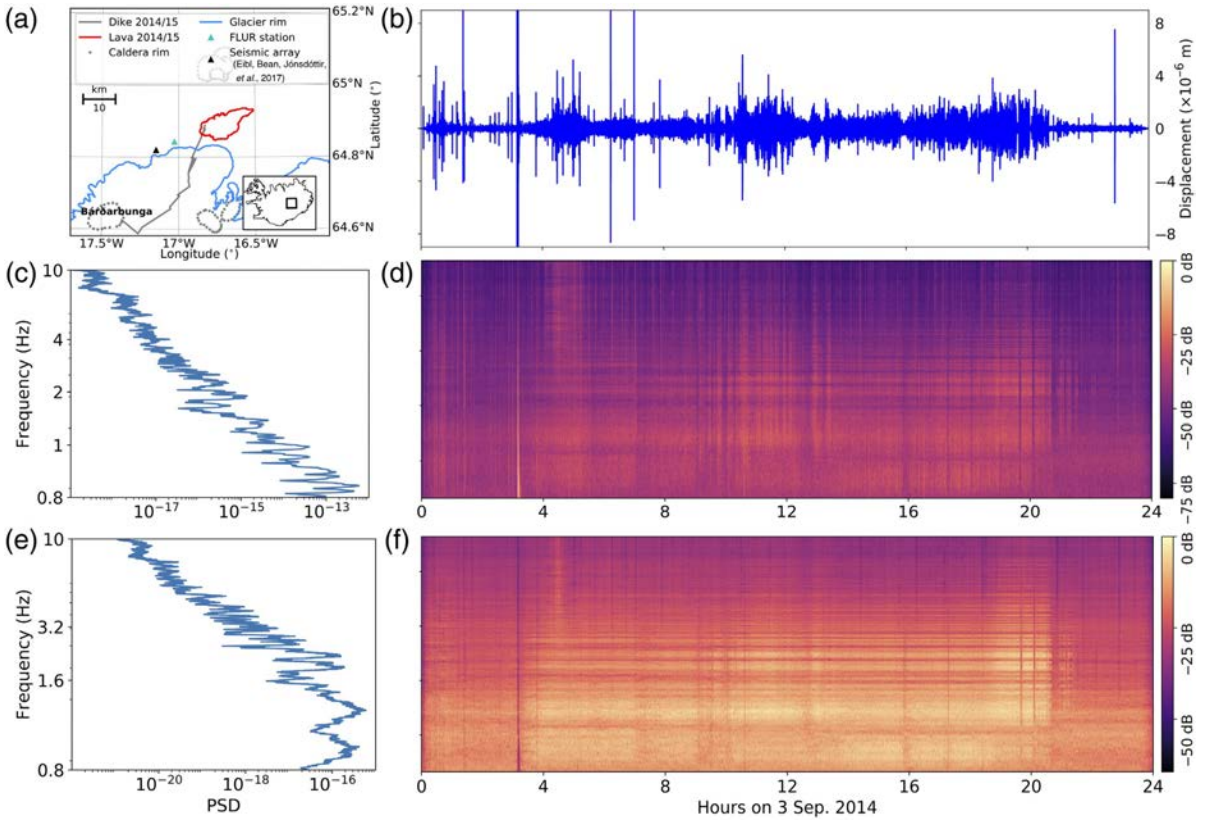

Figure 2.1. Aspects of the Holuhraun 2014–2015 eruption data and the application of the proposed method. (a) The eruption site and the station location. Glacier, the 2014 formed dyke segments as described in Sigmundsson et al. (2015), FLUR station, the erupted lava flow field in Holuhraun, Bárdarbunga volcano, and the seismic array (Eible, Bean, Jónsdóttir, et al., 2017) are marked. The inset map in the bottom right shows the location in Iceland. (b) An example of real data from 3 September 2014 (HHZ component of FLUR station from network 7Z; White, 2010). (c) The power spectral density (PSD) and the (d) spectrogram of this day for the raw seismic data. (e) The PSD and the (f) spectrogram for the extracted tremor signal using the proposed method. The color version of this figure is available only in the electronic edition.

Besides describing the processing steps (Figure 2.2a), we show an input waveform and its spectrogram, which is decomposed in two steps (Figure 2.2b). In the first step using the modified REPET-SIM algorithm, we decompose the X spectrogram into a 'repeating' spectrogram (R spectrogram) and a 'non-repeating' spectrogram (NR spectrogram). Each of these two spectrograms are then decomposed into their harmonic and percussive components in the subsequent step, following the algorithm of FitzGerald (2010). The harmonic component of the repeating spectrogram shows the final result for the harmonic spectrogram (HARM spectrogram) and the percussive component of the non-repeating spectrogram shows the final result for the transient or percussive spectrogram (TRAN spectrogram). The HARM spectrogram corresponds to the tremor spectrogram according to our assumptions of the generating process. From the tremor spectrogram in the frequency domain, the tremor signal can be reconstructed in the time domain. The problem of reconstructing a signal from its modified STFT has varieties of applications in audio signal processing, where modifications are applied to the amplitude STFT and the phase information is lost (Sturmel & Daudet, 2011). The standard phase reconstruction Griffin-Lim algorithm (Griffin & Lim., 1984) which is based on random phase initialization followed by the minimization of the squared error between the STFT of the estimated signal and the modified STFT, shows poor performance for our seismological test signals. The random initialization of phase is an inadequate starting model for the inversion procedure and results in an unreliable signal estimate. The problem of this

inadequate signal reconstruction is illustrated by an example (Figure 2.3d) and is described at the end of this section.

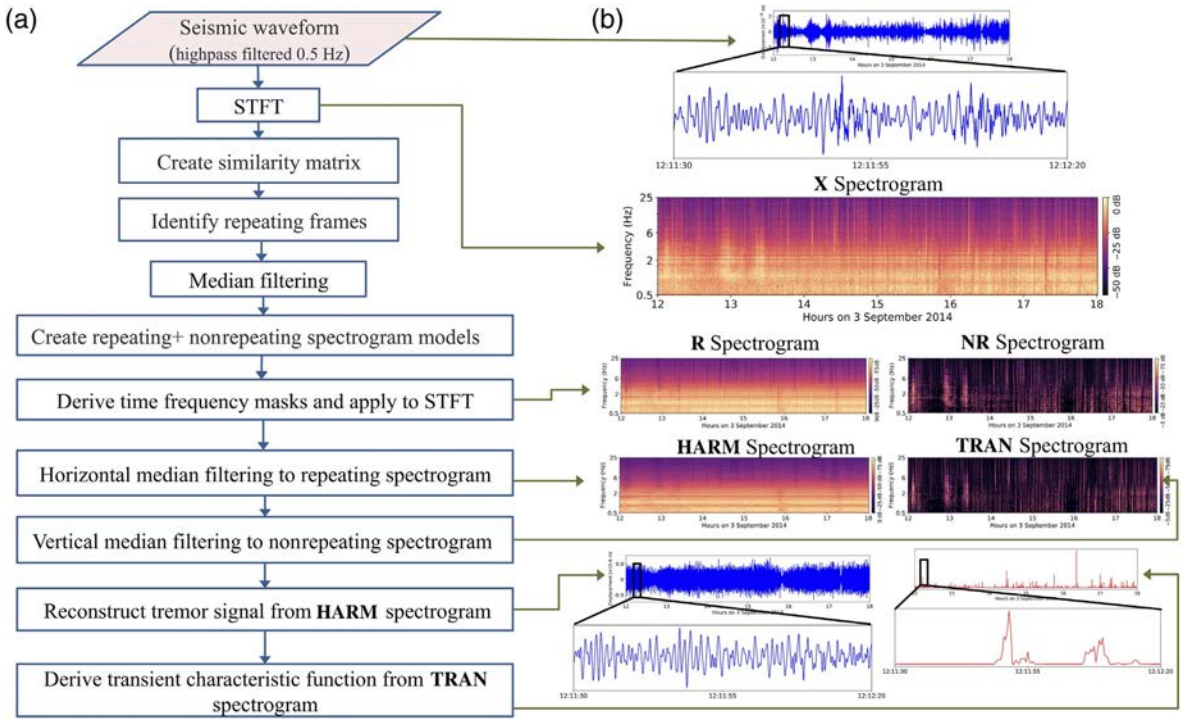

Figure 2.2. Tremor extraction and earthquake detection flowchart. (a) Processing steps of the method and (b) illustration of the processing steps with a real data example. STFT, short-time Fourier transform. The color version of this figure is available only in the electronic edition.

We must use phase information of the original STFT X in order to reconstruct the signal in the time domain. Considering the notation in section 2.2.1, we calculate the similarity matrix based on V as the amplitude spectrogram. Therefore, we need to separate the complex-valued spectrogram X into its amplitude (V) and phase components using equation (2.8).

$$X = V * exp(1j * \varphi), \tag{2.8}$$

where φ denotes the phase of X and j is the imaginary unit. The procedure of using the initial phase matrix is more problematic than it might seem at first glance. Simply using the phase information of X can lead to a noisy reconstructed signal due to the noise contributions in the phase matrix of the seismic waveform. Therefore, we use the values of the phase matrix only in the dominant frequency band of the HARM spectrogram. We do so by integrating the HARM spectrum amplitude squared for all time frames and determine the starting frequency as the 5% quantile of the total energy in the spectrum and the stop frequency as the 95% quantile, respectively. The dominant frequency band is between the start and stop frequencies. Then, we add this modified phase information (weighted phase information) named φ_t to the HARM spectrogram using equation (2.9).

$$T = HARM * exp(1j * \varphi_t), \tag{2.9}$$

where T is the complex tremor spectrogram and HARM is the harmonic amplitude spectrogram.

Finally, we reconstruct the tremor signal time series from the complex spectrogram T, using the inverse short-time Fourier transform. The inversion process is done using the Griffin-Lim algorithm (Griffin & Lim., 1984) for converting a complex-valued spectrogram to a time series by minimizing the mean squared error between the complex STFT of the estimated signal and the modified STFT T. Note that using a part of the phase information sees the Griffin-Lim algorithm converging to a reasonable time domain signal, whereas it won't if starting with randomly selected phases.

Figure 2.3 shows the seismic signal (Figure 2.3a blue) and a comparison of the reconstructed volcanic tremor signal for one minute of seismic waveform from 3 September 2014 using our approach (Figure 2.3a green and 3b) and two other methods (Figure 2.3c and d) described below. As shown in Figure 2.3 (b) the reconstructed tremor signal using our method is not noisy and shows almost no trace of transient signals. Figure 2.3 (c) shows the reconstructed signal using the inverse short-time Fourier transform, after applying horizontal median filtering (FitzGerald 2010) on the STFT spectrogram with the aim of separating and extracting the harmonic tremor signal. In this case, the tremor signal is reconstructed by adding the phase of the original seismic waveform to the modified STFT. Transient signal energy still exists in the reconstructed harmonic signal, which demonstrates that horizontal median filtering is not sufficient for extracting a clean tremor signal without signs of transient events.

In Figure 2.3 (d), we show the estimated tremor signal using the original Griffin-Lim algorithm for phase reconstruction. The effect of earthquake signals is almost eliminated, as in Figure 2.3 (b), which is reasonable as both Figure 2.3 (b) and (d) are extracted from the HARM spectrogram. However, a significant difference compared to the seismic signal is visible in Figure 2.3 (d) in terms of the shape of the signal. Also, the phase is not reconstructed correctly. Therefore, this signal (Figure 2.3d) is not applicable for seismological purposes. This shows the importance of using appropriate phase information for reconstructing a seismic signal in the time domain.

We note that a prefiltering of the original seismic data is necessary to remove microseismic signals before applying our algorithm. Indeed, microseisms are harmonic signals, which may have a dominant energy in the tremor spectrogram. Therefore, the amplitude and the phase of the reconstructed tremor signal could be significantly affected by such microseism signals if they are not filtered out beforehand. We applied a high-pass filter with a cut-off frequency of 0.5 Hz on our real dataset.

2.2.3 Transient signal detection and timing estimation

In a second step, we use the transient spectrogram to locate the occurrence of transient signals in time. We do so by integrating he spectral amplitudes over the full frequency band at each time frame, thus deriving a characteristic function suitable for detecting transient events. At the time of transient events, this function has large values compared with zero or very small values in other parts of the function.

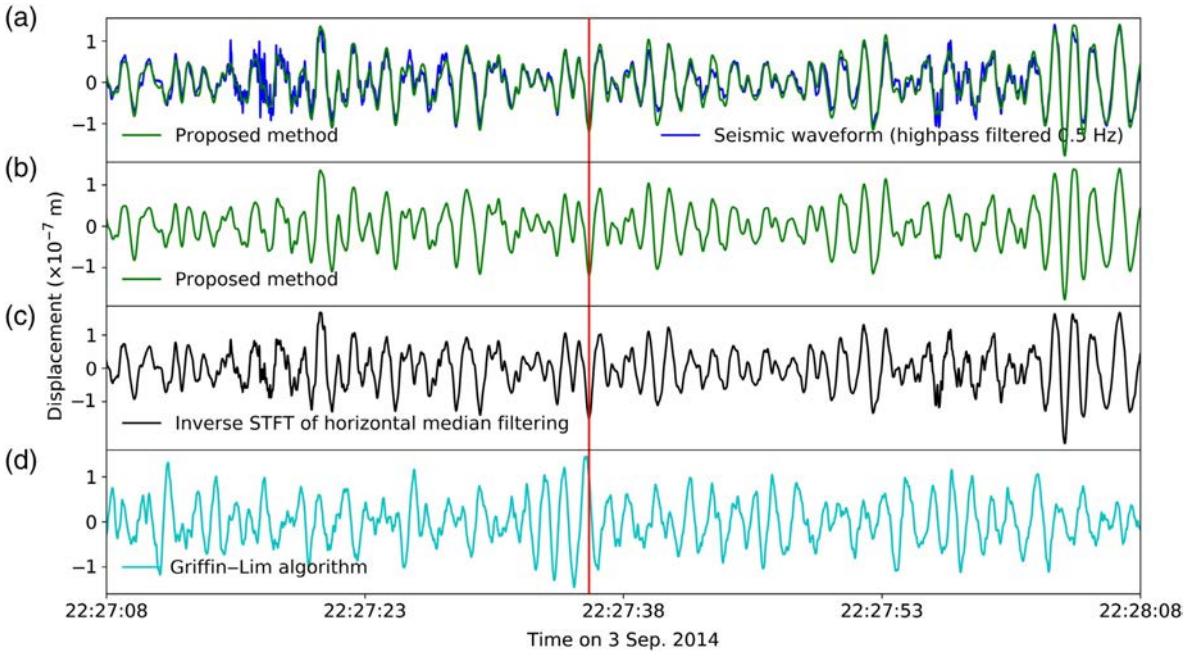

Figure 2.3. Comparison of the extracted tremor signal using the proposed method and two other methods. It is visualized for a short time window of data from 3 September 2014 (HHZ component of FLUR station from network 7Z; White, 2010). (a) The raw seismic signal (blue) and the reconstructed tremor signal using our method (green). (b) Same as the green trace in (a). (c) The reconstructed tremor signal using horizontal median filtering. The traces of transient events still exist in this signal. (d) The estimated tremor signal using the Griffin–Lim algorithm for phase reconstruction. The vertical red line is drawn to illustrate the phase alignment of the signals. The color version of this figure is available only in the electronic edition.

Most observed transient signals in the seismic recordings can be interpreted as seismic-wave arrivals of earthquakes. A standard task in observational seismology is then to estimate arrival times of wave groups from timing the onset of transient signals. Proposing the detection of transient signals with the characteristic function described earlier, we further aim to extract an accurate onset time of the transient signals. For detection, we use a local maximum (peak) search on the transient characteristic function. Two thresholds are applied to the characteristic function—the upper threshold and the lower threshold. The upper threshold is used for transient signal detection, and the lower threshold is used for accurate onset timing. The upper threshold prevents picking up minor local maxima representing coda waves or other fluctuations in the earthquake records. This threshold is determined by visually analyzing the peak value distribution on some smaller test set in the data. The local maxima, which are larger than the threshold, are then considered to represent detected earthquakes. The maximum peak of the characteristic function corresponds mostly to S-wave arrivals, whereas the P-wave onset can be associated with the earliest break in the characteristic function. We have, therefore, developed a straightforward procedure to find the first-arrival onset of the transient events by considering amplitude and amplitude derivatives of the characteristic function for the prepeak interval time window from the largest local maximum found in the characteristic function (Figure 2.4). We used a 5 s prepeak interval time window, because most of the earthquakes in this study are local, and $t_S - t_P$ difference times are less than 5 s. This time window is shown in Figure 2.4. It is recommended to use a larger prepeak interval time window for regional earthquakes. We shorten this prepeak interval time window preceding each peak using the following criterion. First, we adjust the lower threshold visually to the level of residual signal energy from the harmonic signal component remaining after the separation process. The lower threshold is the smallest nonzero number in the characteristic function, which does not correspond to the transient signals. This allows the removal of minimal amount of residual energy due to the

separation process. Using the lower threshold improves the accuracy of onset time picking. We set all values of the characteristic function below the lower threshold to zero. Second, we check if there are some neighboring zero samples in the time window and change the starting point of the window to one sample after the last zero sample to prevent mixing with a very close preceding event. Indeed, neighboring zero samples means that there is no transient signal, and shortening the window avoids confusion with a close preceding event. We skip the samples following a local maximum within the window, if there are any. Then, we calculate the slope between each two neighboring samples, and, we skip the samples following a slope reduction, if there are any. Finally, the starting point of the transient signal (P-wave arrival) is the point showing the maximum slope increase (see Figure 2.4).

2.2.4 Parameters selection

Although the separation process creates a harmonic and percussive spectrogram, the process must be repeated twice with different fast Fourier transform (FFT) window lengths, if both tremor signals and the timing of the transient events are to be determined. Because of the uncertainty principle in Fourier analysis, it is impossible to increase both the temporal resolution and the frequency resolution. A better frequency resolution requires a longer time window for the spectral analysis (longer FFT length), which implies a reduced temporal resolution. Similarly, using a shorter FFT window increases the temporal resolution, whereas the frequency resolution will be reduced. For extracting the tremor signal, we need a high resolution in the frequency domain, and, therefore, a large number of FFT points is chosen. We use an FFT window length of 81.92 s with an overlap of 75%, corresponding to an FFT size of 8192 at a sampling frequency of 100 Hz. To detect transient events, a high resolution in the time domain is needed, and a small number of FFT points and short hop size (number of samples between each successive FFT window) are chosen. We use an FFT size and FFT window length of 1.28 s, with an overlap of 75%. Considering the data's 100 Hz sampling frequency, neighboring FFT windows are spaced in time by an interval of 0.32 s (3.125 samples per second). Fourier transforms with a narrower FFT size are not recommended for our algorithm due to the resulting limited frequency resolution.

There are two sets of median filter procedures used in our method. The first one, which is described in the HPS Algorithms section, is part of the REPET-SIM algorithm and is depicted in the flowchart of Figure 2.2a. After identifying the similar frames and storing them in the array J, the median of J is taken for each frequency to construct W.

The second median filter procedure is described in the section 2.2.2 where a second harmonic-percussive separation approach is applied by using the median filtering method of FitzGerald (2010). Both a horizontal and a vertical median filter are applied separately to the spectrograms of R and NR (see the flowchart in Figure 2.2(a)). We use a standard kernel size of 31 for both the horizontal and vertical median filters, as it has been shown by Driedger et al. (2014) that the choice of this parameter is not critical if not choosing extreme values. Both R and NR are decomposed into two spectrograms, i.e., containing harmonic and percussive signal components. The harmonic component of the R spectrogram is the final harmonic spectrogram (HARM, see figure 2.2b). The percussive component of the spectrogram is the final spectrogram of the transient components (TRAN, see Figure 2.2b).

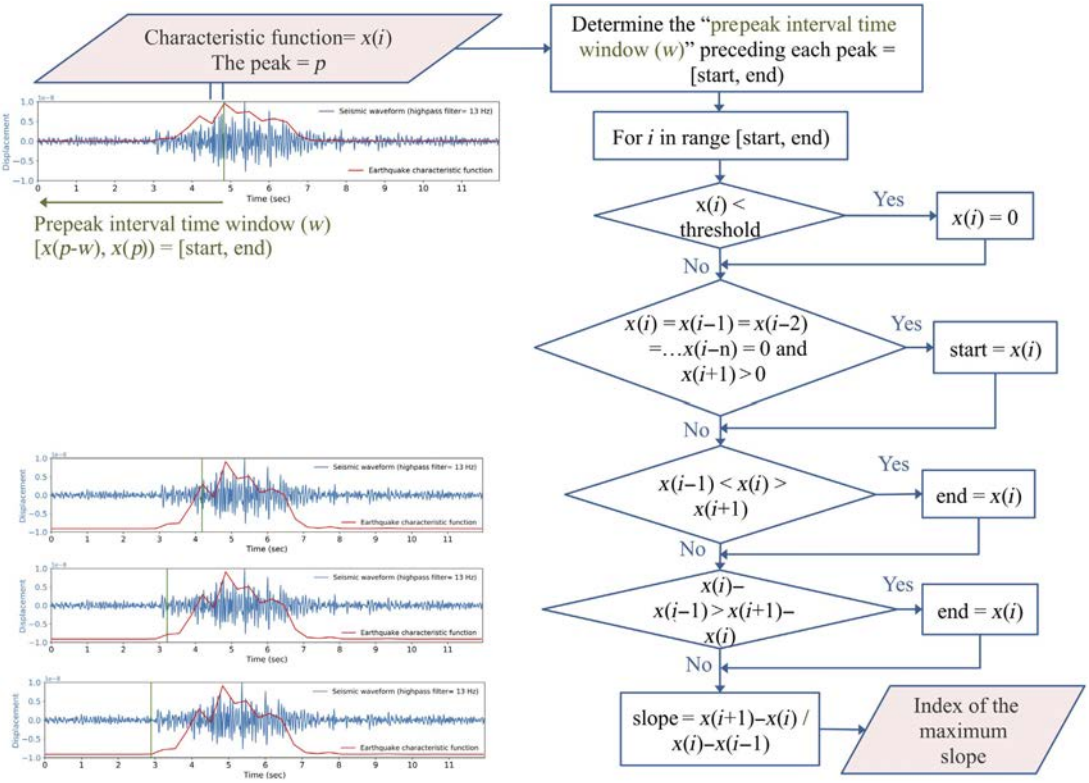

Figure 2.4. Flowchart for backtracking the peaks to the arrival time. The example shows an earthquake time history and its characteristic function. The vertical green line in the top left figure shows the first selected peak, which is sent back in time to the P- arrival time step by step. In the top left, the prepeak interval time window is demonstrated as [start, end). The bracket means including the start point in the time window, and the parentheses means excluding the end point from the time window. The uncertainty of the P-arrival time in this example is 0.1 s through visual inspection. The color version of this figure is available only in the electronic edition.

2.3 Datasets and Testing

2.3.1 Generation of semisynthetic data

We created a synthetic harmonic signal, convolving equally spaced spikes with a real-valued Morlet wavelet (Figure 2.8a, available in the appendix). In this way, we can model the basic features of a harmonic spectra (Schlindwein et al., 1995). Instead of using exact constant repetition intervals and a fixed amplitude, which produces a perfect harmonic tremor signal, we varied the interval times as well as the amplitude of the spikes according to a normally distributed random variable around some mean value with about 10% variance. This results in slightly broadened peaks of the harmonic spectrum and reproduces the variation that we observe in seismic records of volcanic tremors (Eibl, Bean, Vogfjörd, et al., 2017; Figure 2.8b). After creating the harmonic signal, colored noise resembling Peterson's low-noise model (LNM, Peterson, 1993) is added to the signal. The colored noise is synthesized by computing coefficients of a zero-phase finite-impulse-response (FIR) filter via inverse FFT from the spectral representation of the LNM. Then, we apply the FIR filter to a random time series of arbitrary length and multiply it with an amplitude factor to adjust the SNR of the tremor versus colored noise (Figure 2.9). Finally, we add real earthquake recordings randomly in time to the resulting time series of synthetic tremor and noise (Figure 2.10). Each earthquake signal, which is used for semisynthetic data creation, is cut from the beginning of the P wave until the signal amplitudes return to the pre-event noise level after the S- or surface-wave coda part. We used different types of the earthquakes' signals, that is, both LP and volcano-tectonic events within the time period from 15 September to 20 September 2014 show significantly different signal

durations. In total, we created 24 hr of semisynthetic data by combining 500 real earthquake recordings with synthetic harmonic waveform and a seismic noise series. More details about the semisynthetic data generation can be found in Figures 2.8–2.10. Figure 2.5a–c shows the components of the semisynthetic signal, and Figure 2.5d shows the created semisynthetic signal.

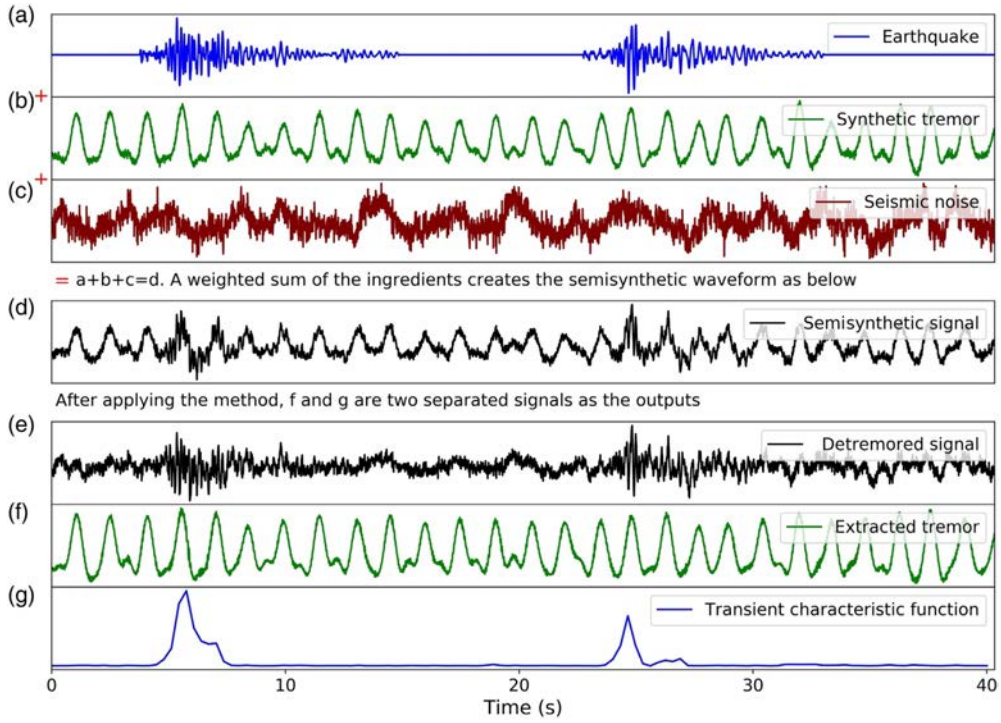

Figure 2.5. Testing the method with semisynthetic data.(a) Earthquake signals, (b) synthetic tremor signal, and (c) seismic noise signal are the elements for creating semisynthetic data. Each of these three signals is normalized by dividing by their standard deviation. (d) Weighted sum of the data in (a–c), which is used as an input for our method. The signal-to-noise ratio (SNR) of the earthquakes is 0.2, and the harmonic SNR is equal to 2. (e) The detremored signal derived by subtracting the extracted tremor signal from the semisynthetic signal. (f) Extracted tremor signal and (g) transient characteristic function as outputs of our method. The color version of this figure is available only in the electronic edition.

We applied our method to this semisynthetic dataset. The synthetic harmonic signals were extracted, and the earthquakes were detected via the characteristic function. Figure 2.5e shows the semisynthetic signal after subtracting the extracted tremor signal from it, and we name it the detremored signal. As shown in Figure 2.5e, this signal has a larger earthquake SNR, and an improvement in the first-motion piking is seen. This is useful when we need to remove a harmonic noise from the seismic waveform. Figure 2.5f-g shows the extracted harmonic signal and the earthquake characteristic function as outputs of the method.

2.3.2 Testing the tremor extraction algorithm using semisynthetic data

To evaluate the ability of the method for tremor signal extraction, we use the created semi-synthetic data with different SNR of the harmonic signal. In order to set different SNRs, we normalize each component of the semi-synthetic data by dividing it by its standard deviation and then we weight them based on the desired SNR. Our harmonic signal extraction process is performed on the semi-synthetic data and the harmonic signal is then reconstructed. The cross-correlation of the synthetic harmonic signal and the reconstructed harmonic signal using our method is measured (Figure 6). Cross-correlations measure the similarity of two time series, so

we calculate them to evaluate how similar the reconstructed harmonic signal is to the synthetic harmonic signal. If the two time series are identical, the cross-correlation coefficient will be 1 and if they are completely different, the cross-correlation coefficient will be 0. We can reconstruct the tremor signal for a SNR of at least 0.4 with a cross-correlation of more than 0.8. The synthetic harmonic signal and the reconstructed signal match well in both phase and shape (see Figure 5b and f). The differences between these two signals is usually related to small fluctuations in the input harmonic signal, which shows a random pattern instead of a repetitive pattern. The similarity matrix is not able to identify random patterns, therefore, they are not reconstructed in the output signal. Figure 6 shows the SNR and related cross-correlation of input and output harmonic signal.

2.3.3 Testing the tremor extraction algorithm using semisynthetic data

To evaluate the capacity of our method for earthquake detection, we use the created semisynthetic data with different earthquake SNR. We report the local SNR here, which refers to the ratio between the variance of the earthquake signal and the variance of the local related segment of the semisynthetic data. The local related segment is the time window that contains the earthquake signal as well as synthetic tremor signals and seismic noise in the background. The segment has a variable length that corresponds to the earthquake signal duration. The advantage of the semisynthetic signals is that we can measure and control the individual components. The results show that for SNR = 0.1, we can detect more than 78% of the events; however, below SNR = 0.3, there is a significant number of false picks (up to 30% of all events), whereas the average percentage of false picks is 6% for SNR between 0.3 and 1. For SNR higher than 0.1, 42% of the missed events are LP events. The SNR and related detection rates are reported in Figure 2.7a. Some examples of semisynthetic data with different earthquake SNR and different SNR of harmonic signal component are presented in Figures 2.11–2.14.

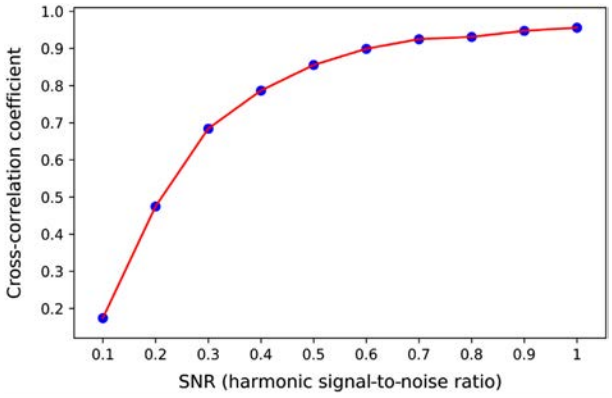

Figure 2.6. Cross correlation of the semisynthetic harmonic signal and the reconstructed harmonic signal versus the SNR of harmonic signal. The color version of this figure is available only in the electronic edition.

Most missed events are similar to that shown in Figure 2.7b, which are classified as LP events (Woods et al., 2018). Figure 2.7c shows a typical volcano-tectonic event for comparison. That LP events that are often not detected can be explained by the properties of the detection characteristic function. This function is derived from summing all frequencies in the transient spectrogram for each time frame. Thus, the characteristic function is sensitive to broadband signals. However, LP events are narrow-band, which results in a poor performance, although the signals are contained in the transient spectrogram. Also, if LPs persist longer, it becomes more difficult to detect them because of the basic structure of the method. Indeed, to create the repeating spectrogram, for all time frames, we derive the corresponding frame (in the repeating

spectrogram) by taking the median of the similar frames (which are identified using the similarity matrix) for each frequency bin. For a transient (short duration in time) event, there are a few numbers of similar frames in the spectrogram, so it is identified as a nonrepeating pattern. Therefore, it will show a short-lasting sharp peak in the transient characteristic function. In contrast, for a long-lasting event, there are some adjacent similar frames, which will be replaced in the repeating spectrogram by the median of them. Therefore, it shows some long-lasting, less sharp, adjacent peaks in the transient characteristic function, which is less likely to be detected by the local maximum finder compared with sharper peaks.

2.3.4 Real data tests

In a final step, we applied the method to a dataset of the Holuhraun 2014–2015 eruption and extracted volcanic tremor signals from the seismological records. As discussed in the Volcanic Tremor Extraction Approach section and showed in Figure 2.3a,b, the reconstructed tremor signal matches well with the original seismological records and has no trace of transient, earthquakes-related signals. This dataset consisted of one month (September 2014) of recordings by the FLUR station, and we use a single vertical component to detect earth- quakes. We compared our detected earthquakes with the bulletin presented in Ágústsdóttir et al. (2019). For the station location with respect to the eruption fissures, please see Figure 2.1 and Woods et al. (2018). About 84% of the total of 5071 events listed by Ágústsdóttir et al. (2019) were detected by our proposed approach.

We detected a total of 12,619 events, which is more than twice the number of listed events in the bulletin. The bulletin is made based on an automatic detection method using Coalescence Microseismic Mapping (Drew et al., 2013) with the velocity model used in Ágústsdóttir et al. (2016, their figure S2c). The bulletin earthquakes were relocated (Ágústsdóttir et al., 2019) using cross-correlated, subsample relative travel times following the method of Woods et al. (2019). A dense local seismic network comprising 72 three-component broadband instruments was used to create the 1 yr bulletin. Our detection process currently uses only one component of seismic recording from a single station. In the future, the result could be improved using three-component signals and additional stations, because some of the smaller events may have larger amplitudes on the other components or stations. An event with a larger amplitude shows a larger peak in the characteristic function, and hence the probability of its detection using our algorithm will increase.

Our method can detect two adjacent earthquakes with a minimum interval of around 10 s. This interval is defined by the number of samples, which must be waited after picking a peak in the local maximum finder. The interval value depends on the number of FFT points, the hop size, and the type of earthquake. In our dataset, earthquakes are mostly local, where shorter waiting time values will result in the detection of more than one peak for one event.

Using the algorithm described in the Transient Signal Detection and Timing Estimation section, we are able to find P-wave arrival times using the detected peaks via the local maximum finder. The uncertainty in the example shown in Figure 2.4 is 0.1 s through visual inspection. The pattern of the characteristic function for different types of events is, however, not always similar to the simple shape we have assumed, which mostly corresponds to the energy shape of a local event and could have more fluctuations; thus, the uncertainty in detecting the P arrivals could be higher. We compared the P-arrival-time residuals of our method and those given by the bulletin of Ágústsdóttir et al. (2019) for one month. For 52% of the events, the time difference is less than 1 s, whereas 48% of the events show a time difference of between 1 and 6 s. A significant part of large time differences is related to LP events, in which the duration of the

event is long compared with volcano-tectonic events in the characteristic function, in which the first arrival is outside of the prepeak interval time window. In this case, the algorithm is able to send the first selected peak back in time to the starting point of the window and shorten the time difference; however, the emergent onset of the LP event is still earlier in the time axis. This algorithm (finding P-wave arrival times using the detected peaks) could be improved upon by assigning different parameters for different event types.

The algorithm that is proposed here is a simple way to attribute the peaks to the starting point of changes in the characteristic function. This could be applied in different fields when a function has not only rather stable values but also experiences sudden changes, and finding the first point of the starting changes is important. One could develop the algorithm by adding more criteria based on the information about the phenomena that are attributed to the changes to decrease the uncertainty in finding the starting point of change.

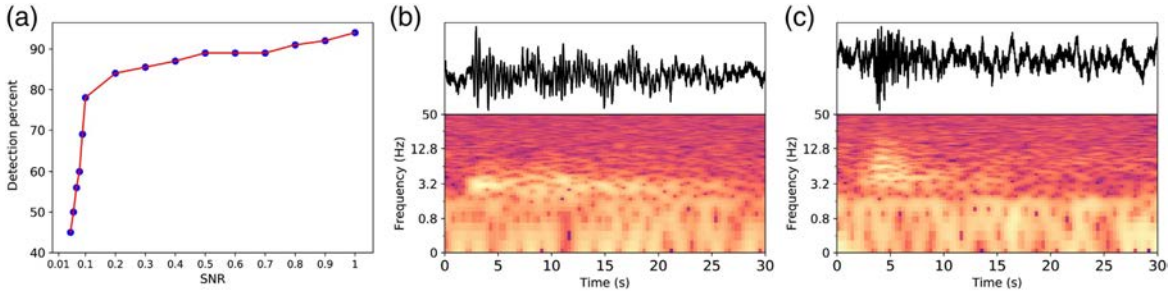

Figure 2.7. Detection rate of earthquakes in the semisynthetic data as well as two earthquakes as samples of detected and not-detected events by our method. (a) Detection rates for semisynthetic data as a function of the SNR. (b) Seismic waveform and spectrogram of a not-detected long-period (LP) event on 16 September 2014. (c) Seismic waveform and spectrogram of a detected volcano- tectonic event on 16 September 2014. The color version of this figure is available only in the electronic edition.

2.3.5 Feasibility of the method with respect to processing speed

The average computation time for the tremor extraction of a one-day-long record with an FFT window length of 81.9 s, overlap of 75%, and a sampling frequency of 100 Hz, is about 70 s, when implemented in Python using Librosa on a PC with an Intel core i7 (six-core) processor of 2.2 GHz and 16 GB of RAM. For transient signal detection with an accuracy of 0.32 s, the computation time is about 34 min with an FFT window length of 1.28 s and an overlap of 75%. The significant difference in the computation time between the tremor extraction and transient signal detection is due to the different FFT window lengths of the two processes. Reducing the FFT length and using the same overlap of 75% increases the number of FFT windows for the overall data time range and the associated computation time.

2.4. Conclusions and Outlook

In this work, we have developed a method to extract and reconstruct volcanic tremor signals, as well as to detect transient signals from seismic waveforms. We used a combination of two HPS algorithms from the field of MIR to separate harmonic and percussive elements of the seismic waveform in the time–frequency domain. This combination leads to a better separation of the components and results in clean tremor and transient spectrograms. The tremor signals are reconstructed in the time domain using weighted phase information of the initial seismic complex spectrogram at each time frame through the energy contribution of the tremor spectrogram. We showed that it is important to use phase information to reconstruct a signal in the time domain for seismological purposes to provide an accurate phase reconstruction. We

also discussed how to use a weighted phase matrix based on the dominant frequency band of the tremor spectrogram that can almost eliminate the noise contributions in the phase matrix of the seismic waveform. The reliability of the reconstructed signal was shown using semisynthetic tests. The cross correlation between the synthetic harmonic signal and the reconstructed harmonic signal using our method was higher than 0.8 for SNRs of the synthetic harmonic signal above 0.4. In addition, more than 78% of earthquake signals in the semisynthetic data with SNR = 0.1 can be detected using our method.

The capability of the method for earthquake detection was also evaluated in comparison to a real earthquake catalog. The detection of more than twice the number of the Ágústsdóttir et al. (2019) bulletin events demonstrates the ability of the proposed method for detecting smaller seismic events, even when only a single station and component is available.

The developed method is able to extract harmonic tremor signals and is applicable to other volcanoes that exhibit such phenomena. A possible application of the proposed method is to extract volcanic tremor signals using a network or an array during a period of heightened volcanic activity. In particular, the clean tremor signal can be used for tremor source location using array analysis, given that the tremor signal reconstruction provides the true phase of the signal. This may provide an improved analysis of the spatial and temporal evolution of volcanic tremors during active volcanic periods.

Another application of this method is in the field of earthquake analysis research. Here, we suggest using the seismic waveform after subtracting the tremor signals (if tremors are present). We named this signal as the “detremored” signal in the Generation of Semisynthetic Data section (see Figure 2.5e). The advantage of using the detremored signal is the resulting increase in the earthquake SNR and improvements in the first-motion picking.

In our opinion, the transient signal detection algorithm introduced in this study is a useful tool for detecting seismic events and is especially applicable for detecting small events during an earthquake swarm. Although we used one component of one station for earthquake detection in this study, the results could be improved using three components and additional station, because some events with low amplitude on the current component and station may show larger amplitude on the other components or stations.

In conclusion, the presented method could provide a basis for tremor source investigations as well as research into eruptive activity, because it provides simultaneous information about tremors and earthquakes and allows the extraction of a clean signal of the tremor for detailed investigations.

Data and Resources

All data used in this article are openly available at Incorporated Research Institutions for Seismology (IRIS; network code 7Z, White, 2010). The Python code related to the proposed method is freely available from https://gitup.uni-potsdam.de/zali/harmonic-tremor-extraction-and-transient-signal-detection (last accessed March 2021). A Jupyter notebook with all the Python codes and parameters related to the proposed method is available as a supplemental material to this article. The supplemental material related to this article also contains illustrations of the semisynthetic data generation. The application of the method using some examples of semisynthetic data with different earthquake signal-to-noise ratios (SNRs) and different SNRs of the harmonic signal component are also presented in the supplemental material.

Acknowledgments

Zahra Zali is grateful for the support by the German Academic Exchange Service (DAAD) through the Graduate School Scholarship Programme under Reference Number 91721165. This work was also supported by the German Research Foundation (DFG MU 2686/13-1, SCHE 280/20-1), and the Daimler Benz Foundation (32-02/18). The dataset is openly available at Incorporated Research Institutions for Seismology (IRIS; network code 7Z, White, 2010). The authors thank Tom Winder for sharing the P-wave arrival times of the bulletin in Ágústsdóttir et al. (2019). The authors thank Diana Roman and an anonymous reviewer for their constructive comments. The authors thank Kevin Fleming for proofreading this article and for his spelling corrections and editorial improvements.

2.5 Appendix

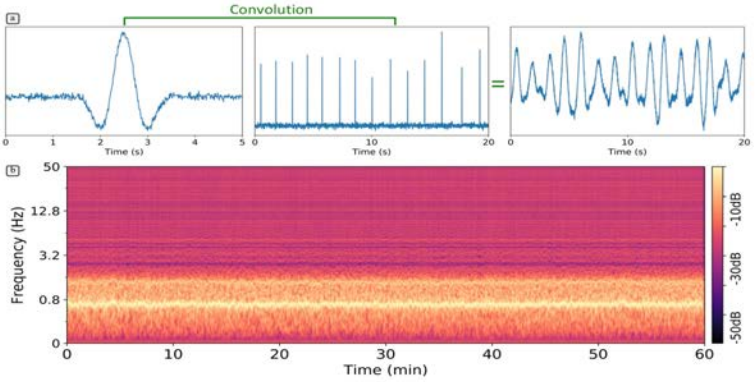

Figure 2.8. The process of synthetic harmonic signal generation. (a) shows the convolution of equally spaced spikes with a real-valued Morlet wavelet which results in the synthetic harmonic signal. The spikes are separated with inter-event times that are fluctuating around a mean value of 1.45 seconds with about 10 % variance. The spectrogram of the synthetic harmonic signal is shown in (b).

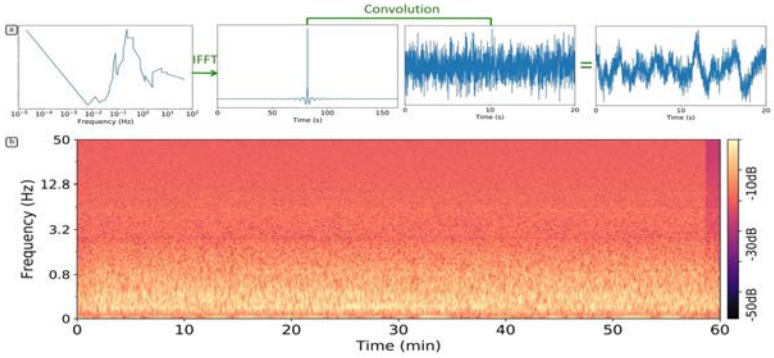

Figure 2.9. The process of the colored noise (Peterson 1993) generation. (a) Peterson's original Low Noise Model (LNM) amplitude spectrum is used to create FIR (Finite-Impulse-Response) filter coefficients by inverse FFT operation. The zero phase filter is applied to a random time series resulting in a synthesized colored noise resembling LNM's amplitude spectrum. The spectrogram of the colored noise signal is shown in (b).

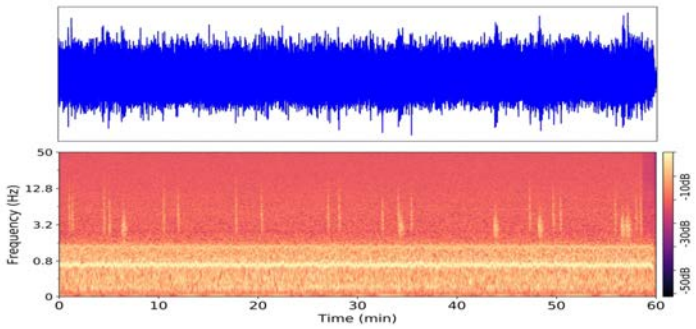

Figure 2.10. One hour of semi-synthetic signal and corresponding spectrogram.

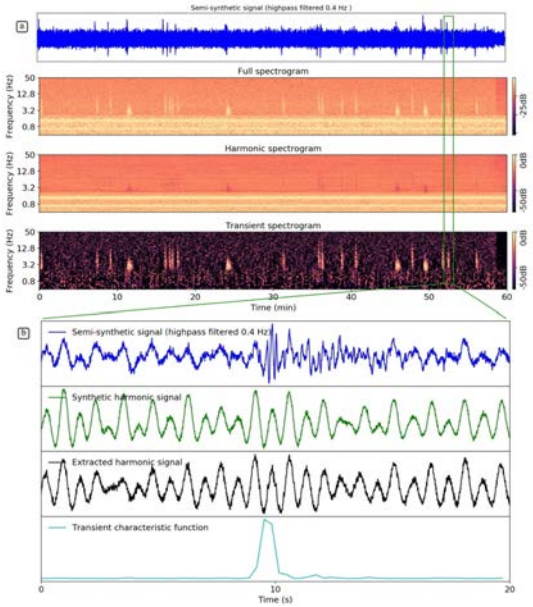

Figure 2.11. An example of a semi-synthetic signal with an earthquake signal (SNR=0.7) and harmonic signal (SNR=1). (a) shows one hour of the semi-synthetic signal, the spectrogram of semi-synthetic signal, the tremor spectrogram and the transient spectrogram which are derived after applying the method. (b) shows 20 seconds of the semi-synthetic signal, the synthetic harmonic signal which is used and the extracted harmonic signal through the method. We can see how the extracted harmonic signal and the synthetic harmonic signal are similar. The transient characteristic function is shown at the bottom. We see a clear peak in the characteristic function at the time of earthquake.

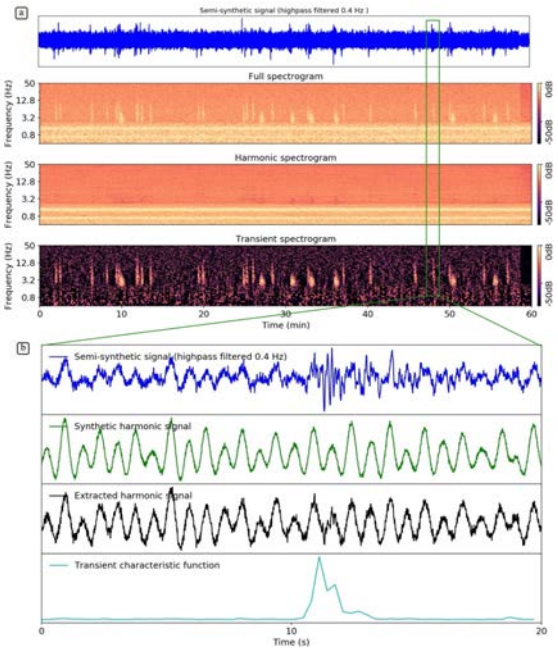

Figure 2.12. An example of a semi-synthetic signal with earthquake signal (SNR=1) and harmonic signal (SNR=0.7). (a) same as subfigure 2.11a. (b) shows 20 seconds of the semi-synthetic signal, the synthetic harmonic signal which is used and the extracted harmonic signal through the method. We can see that for this harmonic signal (SNR=0.7) the extracted harmonic signal is almost similar to the synthetic harmonic signal. The transient characteristic function is shown at the bottom. We see a clear peak in the characteristic function at the time of earthquake.

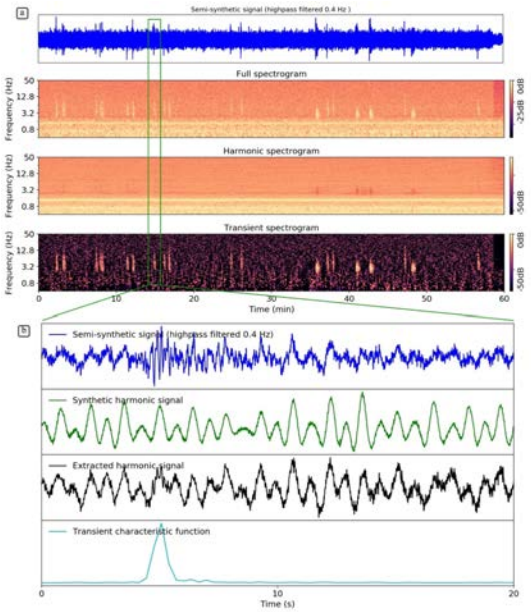

Figure 2.13. An example of a semi-synthetic signal with earthquake signal (SNR=0.5) and harmonic signal (SNR=0.5). (a) same as subfigure 2.11a. (b) shows 20 seconds of the semi-synthetic signal, the synthetic harmonic signal which is used and the extracted harmonic signal through the method. We can see the extracted harmonic signal is following the general shape of the synthetic harmonic signal for this harmonic signal (SNR=0.5), but some differences are visible. The transient characteristic function is shown at the bottom. We see a clear peak in the characteristic function at the time of earthquake.

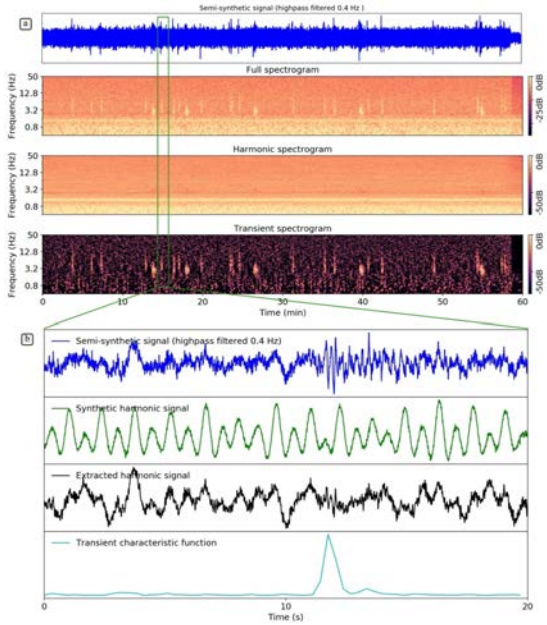

Figure 2.14. An example of a semi-synthetic signal with earthquake signal (SNR=0.3) and harmonic signal (SNR=0.3). (a) same as subfigure 2.11a. (b) shows 20 seconds of the semi-synthetic signal, the synthetic harmonic signal which is used and the extracted harmonic signal through the method. We can see that the harmonic signal is not well reconstructed here because of low SNR of harmonic signal. The transient characteristic function is shown at the bottom. Although the earthquake SNR is low, we see a clear peak in the characteristic function at the time of earthquake.

Chapter 3

OBS noise reduction from horizontal and vertical components using harmonic-percussive separation algorithms

Abstract

Records from ocean bottom seismometers (OBS) are highly contaminated by noise, which is much stronger compared to data from most land stations, especially on the horizontal components. As a consequence, the high energy of the oceanic noise at frequencies below 1 Hz considerably complicates the analysis of the teleseismic earthquake signals recorded by OBSs.

Previous studies suggested different approaches to remove low-frequency noises from OBS recordings, but mainly focused on the vertical component. The records of horizontal components, crucial for the application of many methods in passive seismological analysis of body and surface waves, could not be much improved in the teleseismic frequency band. Here we introduce a noise reduction method, which is derived from the harmonic-percussive separation algorithms used in Zali et al., (2021) in order to separate long-lasting narrowband signals from broadband transients in the OBS signal. This leads to significant noise reduction of OBS records on both the vertical and horizontal components and increases the earthquake signal-to-noise ratio (SNR) without distortion of the broadband earthquake waveforms. This is demonstrated through tests with synthetic data. Both SNR and cross-correlation coefficients showed significant improvements for different realistic noise realizations. The application of denoised signals in surface wave analysis and receiver functions is discussed through tests with synthetic and real data.[a]

[a] Published as: Zali, Z., Rein, T., Krüger, F., Ohrnberger, M., & Scherbaum, F. (2023). Ocean bottom seismometer (OBS) noise reduction from horizontal and vertical components using harmonic–percussive separation algorithms. *Solid Earth*, 14(2), 181-195. https://doi.org/10.5194/se-14-181-2023

3.1 Introduction

Ocean bottom seismometer recordings are generally difficult to analyze because the noise level is usually much higher compared to land stations. At frequencies below 1 Hz, the effect of the ocean noise often dominates the data and hinders the seismological analysis (e.g., Webb et al., 1991; Crawford, 1994). Signals of interest, i.e., transient signals, especially from teleseismic events, can be masked by the oceanic noise. Here, the horizontal components are most strongly contaminated by low-frequency noise. To illustrate the noise on OBS data, we exemplary show the records of the station D10 of the DOCTAR array (see Figures 3.1 and 3.7 in the Appendix). Various studies have tried to identify and characterize the different sources of noise recorded at the ocean bottom (e.g., Webb, 1998; Crawford and Webb, 2000; Corela, 2014; Stähler et al., 2018; Essing et al., 2021; An et al., 2021). In our study, we focus on noise sources that especially affect teleseismic horizontal recordings in the frequency band of 0.02–2 Hz. Generally, the dominant natural noise signals in the oceanic environment are secondary oceanic microseisms (Rayleigh–Scholte waves at the ocean bottom) caused by the interaction of wind-generated water waves, infragravity waves (compliance noise), and tilt noise; the latter originates from the turbulent interaction between currents and the instrument (e.g., Crawford et al., 1998; Corela, 2014). Primary oceanic microseism originates from the interaction of water waves incident at steep coastlines and/or rough seafloor (Hasselmann, 1963; Webb, 1998; Bell et al., 2015). Its spectral peak is around 0.07Hz (Friedrich et al., 1998) in the northern Atlantic. The secondary microseism has frequencies above 0.1–0.25 Hz, with the highest spectral peak around 0.14 Hz (Friedrich et al., 1998, Figure 3.1). It is caused by wind or swell waves propagating in opposite directions. The primary and secondary microseisms affect both the vertical and horizontal seismometer components, whereas the compliance noise is solely observed on the vertical component and the hydrophone. Compliance noise, which is dominant in the frequency band of 0.01–0.04 Hz, is only significant if its wavelength exceeds the water depth (Crawford et al., 1998; Crawford and Webb, 2000; Bell et al., 2015).

Below frequencies of 0.01 and 0.1 Hz, the vertical and especially the horizontal components are highly contaminated by tilt noise generated by ocean bottom currents (Webb, 1998; Crawford and Webb, 2000; Stähler et al., 2018, Figure 3.1). The tilt noise level increases with signal period (see Figure 3.1). The ocean bottom currents in many regions of the oceans are mostly driven by tidal force and often create a signal with the strongest amplitudes below 1 Hz, appearing every 6–12 h (e.g., Brink, 1995; Crawford and Webb, 2000; Ramakrushana Reddy et al., 2020; Essing et al., 2021). The ocean bottom currents passing the instrument create local eddy currents, deform the seafloor beneath the sensor, and tilt the whole instrument frame, to which the seismometer is fixed (e.g., Duennebier and Sutton, 1995; Webb, 1998; Romanowicz et al., 1998; Crawford and Webb, 2000; Corela, 2014; Stähler et al., 2018). Since the noise sources often act at frequencies of teleseismic earthquakes, it is crucial to improve the signal-to-noise ratio (SNR) on OBS recordings for the analysis of the Earth's crustal and mantle structure. Various studies discussed the improvement of OBS recordings through different approaches, either by suggesting a better OBS instrument design (Stähler et al., 2018; Corela, 2014; Essing et al., 2021) or by removing significant amounts of noise from the contaminated data by signal processing (Crawford and Webb, 2000; Bell et al., 2015; Janiszewski et al., 2019). Our study follows the latter approach.

Crawford and Webb (2000) developed a method to remove noise from the vertical OBS component. Calculating the linear transfer function between the horizontal and the vertical component allows estimating the tilt noise, which can then be subtracted from the vertical component. Pressure data measured in parallel to the seismometer recordings allow reducing the influence of infragravity waves on the vertical seismometer component recordings. For

better results, Bell et al. (2015) propose first rotating the horizontal components in the direction of the highest coherence between the horizontal and vertical component before calculating the linear transfer functions. The mentioned methods solely improve the SNR on the vertical component, whereas the noise contamination on horizontal components is often larger. Other recent studies have also attempted to reduce noise on the horizontal components (Mousavi and Langston, 2017; Zhu et al., 2019; An et al., 2021; Negi et al., 2021). An et al. (2021) tried to reduce the noise on the horizontal components by applying the reversed procedure of Bell et al. (2015). Rotation of one horizontal component in the direction of the principle noise indeed results in an improvement of the orthogonal horizontal component, but the other horizontal component became noisier (An et al., 2021). Results of a recent study applying a polarization filter to reduce the noise on all components show strong changes in the broadband waveforms (Negi et al., 2021). The automatic noise attenuation method developed by Mousavi and Langston (2017) is a time–frequency denoising algorithm using the wavelet transform and synchrosqueezing. It can be used to keep the signal and remove the noise or vice versa. The decomposition method DeepDenoise from Zhu et al. (2019) is based on a deep neural network. DeepDenoise decomposes the waveform into signal and noise in the time–frequency domain. The latter methods both improve the SNR but mainly focus on local and regional earthquake detection. They result in changes in the waveform shape if the noise amplitude directly ahead of the signal is significant in comparison to the signal amplitude in a specific frequency. However, the analysis of undistorted broad- band waveforms on the horizontal components is crucial for many passive seismological structure analysis methods, e.g., the calculation of receiver functions or surface wave dispersion and polarization analysis.

Here we introduce a method inspired from music information retrieval (MIR) research, which is adapted to seismological data and used for noise reduction on both the vertical and the horizontal components.

Seismic waveforms and acoustic signals generated by musical instruments are similar in some respects (Schlindwein et al., 1995; Johnson and Watson, 2019). The extensive research in the field of music information retrieval has resulted in advances (e.g., Müller, 2015) that may be useful in seismic signal processing as well. Exploiting the idea of harmonic– percussive separation (HPS) in MIR, Zali et al. (2021) developed an algorithm to separate harmonic volcanic tremor from earthquakes in seismic waveforms. In the present study we use this algorithm after some modifications in order to separate “harmonic” (long-lasting narrowband signals) and “percussive” (broadband transients) components of an OBS data set aiming at noise reduction and retrieval of clearer broadband earthquake waveforms. Throughout this study we will make use of the term noise for any signal other than earthquake signal in the data set. In the context of OBS noise reduction using HPS algorithms, percussive components correspond to earthquake signals and harmonic components correspond to noise signals. Long-duration OBS noise signals that last a few hours to days (depending on the noise type) with a restricted frequency range contrast with transient seismic signals such as earthquakes with a wider range of frequencies.

The algorithm introduced in Zali et al. (2021) is a combination of two HPS approaches that leads to the desired signal separation. Here we also use the two approaches in sequence in order to separate different types of noise signals from the earthquake signals. In the first step we use a similarity matrix (Rafii and Pardo, 2012; Rafii et al., 2014) to separate monochromatic and harmonic noises. In the second step we use median filtering (FitzGerald, 2012) in order to separate the remaining narrowband signals. With this two step approach we can separate and remove much of the OBS noise contamination from the earthquake signals.

3.2 Data

In this study, we discuss the noise recorded by a LOBSTER (Long-term OBS for Tsunami and Earthquake Re- search) OBS instrument from the DEPAS pool, which is equipped with a Güralp CMG-40T seismometer and an MCS (marine compact seismic) recorder (for technical specification see Stähler et al., 2018). We show data recorded during the DOCTAR deployment using DEPAS LOBSTERs located around the Gloria Fault in the northern Atlantic. A total of 12 DEPAS LOBSTERs form the array; they were deployed between 2011 and 2012 and recorded data with a sampling frequency of 100 Hz (Hannemann et al., 2016, 2017).

We observed a continuous harmonic signal at a frequency of 0.04 Hz, partially with one or two overtones on a subset of the array (see Figure 3.1). This signal was observed at 30 % of the stations from the DOCTAR project (e.g., Hannemann et al., 2016, 2017) and at 43 % of the stations from the KNIPAS project (Schlindwein et al., 2018), both using the mentioned DEPAS LOBSTER design. We cannot identify the source of this signal yet, but based on its continuity, we assume an electronic source from the instrument itself.

The hydrophone and especially the horizontal components are highly affected by the strumming of the head buoy, which is attached to the DEPAS LOBSTER frame, causing a "current-induced harmonic tremor signal" (Stähler et al., 2018; Essing et al., 2021, Figure 3.1). These "tremor events" last over up to 4 h and appear every 6–12 h. These presumably tidal-driven tremor events are harmonic signals with a fundamental period of 0.4–1 s and various overtones (1–10 Hz) (Stähler et al., 2018; Essing et al., 2021, Figure 3.1). Regarding the frequency band, tremor events mainly affect the analysis of teleseismic body waves, especially on the horizontal component (Figure 3.1).

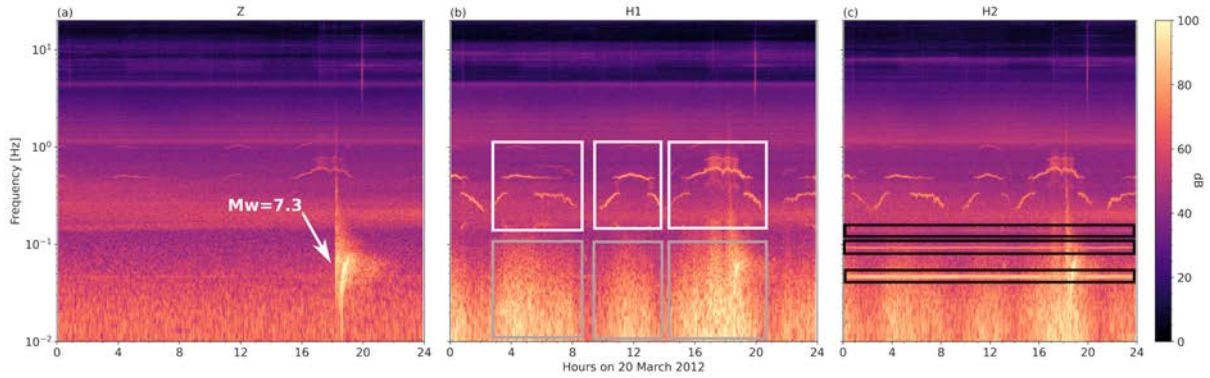

Figure 3.1. Spectrogram of a 1 d OBS signal showing ocean bottom noise on Z (a), H1 (b), and H2 (c) components. The data were recorded by the station D10 of the DOCTAR array with a sampling frequency of 100 Hz. The spectrograms were calculated using a window length of 216 samples and an overlap of 75 %. The signal of an earthquake (Mw = 7.3) on 20 March 2012 at around 18:00 at the station D10 is shown in (a). The tidal cycle of the current-induced noise is clearly visible during the high-tilt-noise episodes (gray box in b). The white box in (b) highlights the tremor episodes caused by the head buoy strumming. On H2 (c) we see instrument-related, presumably electronic noise (black boxes). The high energy of the secondary microseism band at around 0.2 Hz is visible on all components.

3.3 Noise reduction methodology

3.3.1 Harmonic–percussive separation (HPS)

Harmonic–percussive separation refers to the problem of decomposing a signal into its harmonic and percussive components. This topic has received much attention in recent years (Rafii et al., 2018) and has numerous applications in the field of MIR and musical signal processing.

Within a general context harmonic signals show an overtone structure in the spectral domain. We call overtones one or more clear narrowband frequency peaks that are integer multiples of the fundamental frequency (the first frequency peak in the spectrum). Harmonic signals have relatively stable behavior over time and can be identified in a short-time Fourier transform (STFT) spectrogram by horizontal structures referring to constant frequencies along the time axis.

In contrast, percussive signals form vertical structures in an STFT spectrogram that contain energy in a wide range of frequencies. Therefore, it is a straightforward strategy in most HPS algorithms to try to separate the horizontal structure from the vertical structure in the spectrogram corresponding to harmonic and percussive components, respectively. The horizontal lines in the spectrogram could correspond to either harmonic signals or monochromatic signals.

3.3.2 HPS using median filtering (MED)

One of the simplest and fastest HPS approaches is median filtering (FitzGerald, 2010). For simplification we name this algorithm MED in this study. Median filters are usually used to remove noise from an image or a signal. Using a median filter a sample will be replaced by the median of neighboring samples within a window of a specific length (the specific length is the kernel size of the median filter). The entire signal is processed using a sliding window analysis. Within the HPS, two median filters are applied to the amplitude of the STFT spectrogram of a signal. One median filter is performed along the time axis of the spectrogram to suppress percussive events and enhance harmonic components. Another median filter is applied along the frequency axis in order to enhance percussive events and suppress harmonic components. The two resulting spectrograms are then subsequently used to create two masks, which are applied to the original signal spectrogram separately to generate two spectrograms of harmonic and percussive components, respectively. For creating the harmonic and percussive signals in the time domain the phase of the original signal is added to each spectrogram, and the time domain signals are reconstructed using the inverse STFT.

3.3.3 HPS using the similarity matrix (SIM)

Another powerful approach in HPS proposed by Rafii and Pardo (2012) is based on calculating a similarity matrix. We name this algorithm SIM here. This approach is a repetition-based separation, which identifies repeating elements in the spectrogram by looking for similarities by means of a similarity matrix. Within the SIM algorithm, first similar time frames in the spectrogram are identified through a similarity matrix. Then a median filter is applied only to the frames identified as similar to constitute the repeating spectrogram model that corresponds to harmonic components. The non-repeating spectrogram that corresponds to the percussive component of the data is obtained by subtracting the repeating spectrogram from the original spectrogram. For creating repeating and non-repeating signals in the time domain, the phase of the original signal is added to each spectrogram and the time domain signals are reconstructed using the inverse STFT. Details of this approach are discussed in the following section.

3.3.4 HPS noise reduction algorithm for OBS data

The motivation for using HPS for noise reduction of OBS data stems from the different characteristics of earthquake and OBS noise signals as described in Section 3.2. Earthquakes are broadband transient signals, while the signals of OBS noises are more narrowband compared to earthquakes. We combine two modified HPS algorithms to separate those signals in a two-step procedure. We divide the frequency content of the signal into two frequency ranges: the MED frequency range covers the frequency range between 0.1 and 1 Hz, whereas the SIM frequency range contains the complementary frequency range, i.e., all frequencies except the band between 0.1 and 1 Hz. Then two different algorithms are applied to these ranges. In the first step, we use the SIM algorithm and separate only harmonic or monochromatic signals from the original records in the SIM frequency range. The reason is related to the frequency content of the noise and earthquake signals and how the SIM algorithm separates them. For a better understanding, we first explain how the algorithm works and then present more detail about this selection. In the second step, to reduce noise from MED frequency range we apply MED. There we target harmonic (or monochromatic) as well as narrowband signals with gliding frequencies named current-induced harmonic tremor signal in Section 3.2. The overall schematic diagram of our HPS noise reduction algorithm along with an example is shown in Figure 3.2.

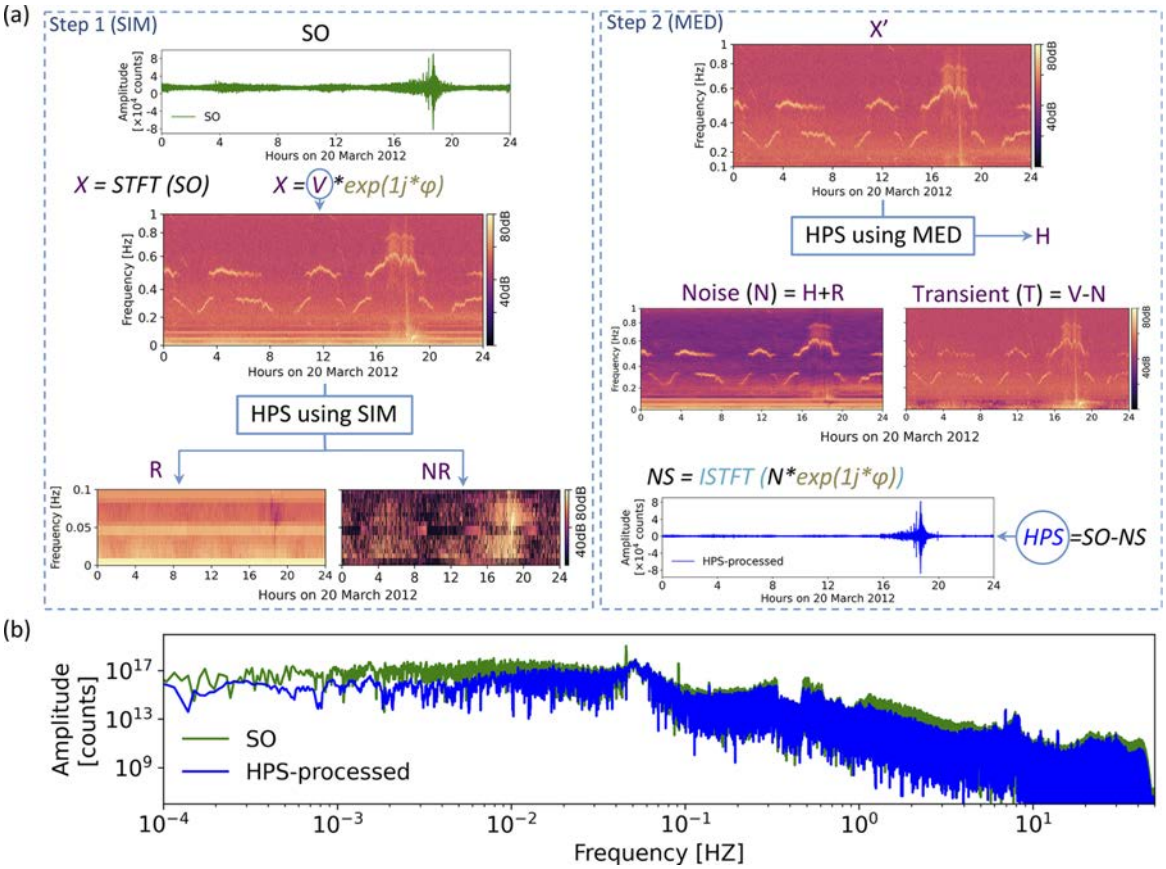

Figure 3.2. Noise reduction method flowchart (a) with an illustration of the processing steps with a real data example. The left panel shows the first step of the method; using the similarity matrix (SIM) in the frequency range below 0.1 Hz and above 1 Hz, we divide the spectrogram (X) of the original signal (SO) into two spectrograms of repeating (R) and non-repeating (NR) patterns. The right panel shows the second step of the method wherein we apply a median filter (MED) to the frequency range of 0.1 to 1 Hz (spectrogram X′) in order to remove noises from this frequency range. It results in the harmonic spectrogram (H). As the interesting frequency range for OBS signals is below 1 Hz, the spectrograms show only this frequency range. Finally, the noise spectrogram (N) is created by summing the separated noises derived from two steps, and the noise signal (NS) is derived using ISTFT. We obtain the noise-reduced signal (HPS) by subtracting the NS from the input OBS signal (SO). STFT: short-time Fourier transform. HPS: harmonic–percussive separation. SIM: similarity matrix.

MED: median filtering. ISTFT: inverse short-time Fourier transform. (b) Spectrum of the original signal (SO) and the HPS noise-reduced signal.

The SIM algorithm is explained in the following: From the original OBS record SO (SO represents the original restituted OBS signal) we derive the STFT named *X* being a complex-valued spectrogram.

The complex-valued spectrogram *X* is separated into its amplitude and phase components using equation 3.1.

$$X = V * exp(1j * \varphi), \tag{3.1}$$

where φ is the phase of *X*, $V = |X|$ is the amplitude of *X* and *j* is the imaginary unit.

All of the spectrogram modifications will be applied to the amplitude spectrogram *V*. The cosine similarity (the similarity between two vectors of an inner product space) between the STFT time frames is calculated through the multiplication of the transposed *V* by *V* with the normalization of the *V*. This is shown in equation 3.2.

$$S(k_a,\mathrm{k}_b) = \frac{\sum_{\mathrm{i}=1}^{n} V(\mathrm{i},\mathrm{k}_a)V(\mathrm{i},\mathrm{k}_b)}{\sqrt{\sum_{\mathrm{i}=1}^{n} V(\mathrm{i},\mathrm{k}_a)^2}\sqrt{\sum_{\mathrm{i}=1}^{n} V(\mathrm{i},\mathrm{k}_b)^2}}, \tag{3.2}$$

where *S* is the similarity matrix. Each point (k_a, k_b) in *S* is the cosine similarity between time frame k_a and k_b of *V*, $\forall k_{a,b} \in [1,\mathrm{m}]$, where *m* is the number of time frames and *n* is the number of frequency channels for each time frame. Once the similarity matrix is calculated we use it to determine the most similar time frames to each single time frame. For time frame k_a we compare all the values in $S(k_a, \mathrm{k}_i)$ for $i \in [1,m]$. We identify similar frames for time frame k_a, by choosing the upper 2% of the all time frames with the highest similarities.
Finally, all similar time frames to any frame *k* in *V* are stored in a temporary array *K*. Those similar time frames are used to create a repeating spectrogram model *W*. The corresponding frame in *W* is obtained by taking the median of *K* for each frequency at each time frame *k*. Those time-frequency bins, which are similar with little deviations between repeating frames, are captured by the median and constitute the repeating spectrogram model. This spectrogram contains only similar and repeating patterns. The time-frequency bins with large deviations between repeating frames would constitute nonrepeating transient patterns and would be suppressed by median filtering.

The nonnegative spectrogram *V* is the sum of two nonnegative spectrograms of repeating and nonrepeating patterns, hence, *W* (the repeating spectrogram model) should always have smaller values or at most be equal compared to *V*. To ensure this, a repeating spectrogram model $\widetilde{W}$ is defined by taking the minimum between *W* and *V*. The nonrepeating spectrogram model is derived by subtracting $\widetilde{W}$ from *V*.

We use these two (the repeating and the nonrepeating) spectrogram models to create two time-frequency masks for repeating and nonrepeating patterns, respectively. Instead of the binary mask, which is used in Rafii & Pardo (2012), we use soft mask via Wiener filtering (Vaseghi, 1996) which is more flexible and usually leads to a better result. The calculation of the soft masks is shown in the following equations:

$$M1 = \frac{\widetilde{W}^2}{\widetilde{W}^2 + \left(V - \widetilde{W}\right)^2}, \tag{3.3}$$

$$M2 = \frac{\left(V - \widetilde{W}\right)^2}{(V - \widetilde{W})^2 + \widetilde{W}^2}, \tag{3.4}$$

in which *M1* and *M2* are repeating and nonrepeating masks respectively. We multiply the masks with the input amplitude spectrogram *V* to separate the repeating and nonrepeating components. The element-wise multiplication of the masks by the input amplitude spectrogram *V* is shown in the following equations:

$$\mathrm{R}=\mathrm{M1} \otimes \mathrm{V}, \tag{3.5}$$

$$\mathrm{NR}=\mathrm{M2} \otimes \mathrm{V}, \tag{3.6}$$

in which *R* and *NR* denote repeating and nonrepeating amplitude spectrograms respectively.

The resulting *R* and *NR* spectrograms are shown in Figure 3.2a for a specific/typical example of an OBS recording. As can be observed in the *R* spectrogram, in particular the low frequency harmonic or monochromatic signals below 0.1 Hz are well captured. We applied the SIM algorithm only to the frequency band below 0.1 Hz and above 1 Hz. In the frequency band from 0.1 Hz to 1 Hz the signals remain unchanged by this procedure. This is the first constraint we consider for the SIM algorithm. In the field of noise reduction using signal processing techniques, a very important point is to not modify the signals of interest for analysis. P and S waveforms in the teleseismic earthquake signals have often frequency content in the range of 0.1 Hz to 1 Hz with a dominant frequency around 0.3 Hz. Oceanic microseism noise, which is usually present in the OBS data, has a dominant frequency around 0.1 Hz to 0.3 Hz. As P and S phases have similar dominant frequency as the microseism noise wavefield, superposition of both wavefields could happen in this frequency range. They could interfere constructively or destructively so the resulting amplitude could be higher or lower compared to the original P or S phase amplitudes. Considering these interferences, using the SIM algorithm, may result in creating fake higher amplitude for these phases or losing part of their amplitude in the noise reduced signal. But this could be problematic only when the amplitude of the noise is changing over the time. For a noise signal with almost constant amplitude, the SIM algorithm can extract the true amplitude of the noise even in the interference moments. However, the microseism noise has slightly varying amplitude over time.

Before moving to the second step we introduce a second constraint parameter, which we use in the SIM algorithm. Surface waves of teleseismic events show usually a dispersed narrow-band signal and correspond to mainly horizontal patterns of short duration (on a daily scale) in the spectrogram. Given the way the HPS separates harmonic from transient signals, the surface wavetrain may be erroneously recognized as harmonic component and thus be separated as noise signal. In order to prevent this and preserve the whole frequency content of the earthquake, we define a so-called waiting factor for the similarity calculation introducing a minimum time distance between two consecutive similar frames. For the problem of retaining teleseismic surface waves we found that a waiting factor of at least two hours prevents the algorithm to prune surface waves from the transient signal part. The rationale is that the duration

of a teleseismic event is usually less than two hours whereas the noise components have longer duration. Using this waiting factor prevents separating any harmonic component of the earthquake signal as noise component. As a side effect this constraint causes that short-duration harmonic/monochromatic noise signals won't be well captured, too. However, these types of signals are not common in OBS data (see section 3.2).

In the second step of our algorithm, to target noise signals in the frequency range of 0.1 Hz to 1 Hz, we use MED as it is described in section 3.3.2. We apply this second part of the noise removal procedure only to a restricted frequency band of 0.1 Hz to 1 Hz. The dominant noise in the MED frequency range is the current-induced harmonic tremor signal (see section 3.2). First we create the X' spectrogram which is equal to X in the MED frequency range and is equal to zero outside of this band. Then we apply a horizontal median filter to X' in order to separate harmonic components. This results in the harmonic spectrogram H, which contains near-horizontal patterns captured by the median filter.

Now we have two separated spectrograms for noise signals: R, which is derived from the first step, and H, which is derived from the second step. Summing these two spectrograms will build the noise spectrogram N. Subtracting N from the input amplitude spectrogram V will construct the transient spectrogram T.

As can be seen in Figure 3.2a in step 2, the dominant energy of the narrow-band signals with gliding frequencies in the range of 0.1 Hz to 1 Hz (the current-induced harmonic tremor noise as introduced in the section 3.2) is captured in the noise spectrogram N, but part of it remains in the transient spectrogram T. Signals with changing frequency which don't form complete horizontal lines in the spectrogram, are difficult to capture by our HPS algorithm, so part of their energy remains in the final spectrogram.

3.3.5 Reconstruction of the denoised signal

In order to reconstruct the noise-removed signal in the time domain we must add phase information to the spectrogram. We had separated the complex-valued spectrogram X into its amplitude V and its phase component using Equation 3.1 and all the further modifications have been applied to the amplitude spectrogram V. The phase of input signal SO is mostly affected by the phase of noise signals as they have the dominant energy in the signal. Therefore, we use the phase information of SO in order to reconstruct the noise signal. We add this phase to the noise spectrogram N using the following equation:

$$N' = N * exp(1j * \varphi), \tag{3.7}$$

where N' is the complex-valued noise spectrogram. We reconstruct the noise signal NS from the complex spectrogram N', using the inverse STFT. Finally the OBS denoised signal HPS (HPS here represents the SO signal after the HPS processing) is obtained by subtracting the noise signal from the input OBS signal SO using the following equation:

$$HPS = SO - NS, \tag{3.8}$$

3.3.6 Parameter selection

Many typical noise signals observed in OBS recordings are harmonic, monochromatic, or

narrowband signals with gliding frequencies (see Section 3.2). In order to extract the expected narrowband noise signals from the STFT we require a high-frequency resolution in the spectral domain, therefore making it necessary to use sufficiently long time windows for the spectral analysis. Here we use a fast Fourier transform (FFT) window length of 163.84 s with an overlap of 75 %, corresponding to an FFT size of 16 384 at a sampling frequency of 100 Hz, which corresponds to a frequency resolution of 0.006 Hz.

We use a kernel size of 80 for the median filter in the MED algorithm. The larger the kernel size, the more noise signal would be captured. However, using very large sizes could introduce waveform distortions. As discussed in Driedger et al. (2014), the kernel size is not critical as far as not using extreme values. Our tests show that a kernel size of 80 is the largest size which leads to a safe separation without capturing any energy of the teleseismic signal.

The values of parameters, which we used for this study, are presented in Table 3.1. These are our recommendations for noise reduction of teleseismic earthquakes. One can tune the parameters based on other specific applications such as denoising local earthquakes or extracting specific signals like microseism signal.

3.4 Results and discussion

3.4.1 General results

In this section we aim to demonstrate the reliability of our HPS noise reduction algorithm and evaluate the improvement of the OBS data. We applied the method to synthetic and real teleseismic earthquake data recorded by the OBS station D10 of the DOCTAR array (e.g., Hannemann et al., 2016 2017). The synthetics were calculated for a source-receiver epicentral distance of 40° (focal depth: 45 km, fcal mechanism: double couple, source duration: 4 s) by using the full wave field software qseis (Wang, 1999) and a modified average ak135 velocity model including a water layer (Kennett et al., 1995). The crustal structure of the velocity model is adapted to the oceanic crust (crustal thickness is 6.6 km) in that area, and the water depth is fixed to 4.9 km. Real oceanic noise of the vertical, radial, transverse (ZRT) components recorded by the station D10 is added to the corresponding components of the synthetic teleseismic signal. We created synthetics for three different noise situations at the beginning (N1), during (N2), and after (N3) tidal currents (Figure 3.3), each with a theoretical SNR of 1–10 between noise and P onset on pure synthetic Z. Throughout the whole paper the SNR is defined as the root mean square (rms) of the signal divided by the rms of the noise. For further details of synthetic data creation see Figure 3.8. For the comparison with real data, we selected 46 teleseismic events in total with magnitudes $M_W > 5.6$ and epicentral distances of 30– 160° (see Figure 3.7). Here only events for which a P onset could be visually identified were used. The pre-selection of the events is taken from Hannemann et al. (2017) and expanded by some events with low magnitudes (see Table S1 in the Supplement). In the following, we will discuss the improvement of the records by comparing the seismograms and spectrograms of synthetic and real data. We also illustrate the improvement for two seismological applications (teleseismic surface wave group velocity analysis and receiver function analysis). For some observations, e.g., checking the phase arrival of the teleseismic body waves, we rotated the arbitrarily oriented horizontal components of the real data into the ZRT system. The orientation angles are taken from the previous study on the DOCTAR array (Hannemann et al., 2016).

Comparing the spectrograms and waveforms of the synthetic example we see a significant improvement of SNR in the HPS processed data set on all components (e.g., Figures 3.3 and

3.9–3.11 for the real data). The continuous spectral lines of the assumed electronic noise are removed from the data, as are most of the spectral lines related to tremor episodes of head buoy strumming. During the tides, we observe a reduction of the spectral amplitudes for the tilt noise, as well as for the general background noise (Figures 3.3 and 3.9–3.11) on the horizontal components. The results from the spectrograms are confirmed by the spectra (Figure 3.2b), which show the removal of the spectral peaks of the electronic noise (0.05, 0.1, 0.15 Hz) and the tremor episodes (0.5–1 Hz). The amplitude and phase information of the synthetic earthquake is preserved in the HPS signal (see Figure 3.3).

To quantify the improvements obtained when using our method, we calculated the cross-correlation of the teleseismic waveform, the SNR of the teleseismic body-wave phases, and the rms of the teleseismic waveform before and after denoising. Because most of the oceanic noise occurs at frequencies below 1 Hz, which is also the most interesting frequency range for the OBS analysis, a 1 Hz low-pass filter is applied to the signals before all result calculations.

Table 3.1: Parameters values used in our study

Parameters	FFT window size	FFT overlapping percentage	SIM frequency range	SIM waiting factor	SIM upper threshold	MED frequency range	MED kernel size
Values	16384 samples	75%	[0-0.1] & above 1 Hz	2 hours	2%	[0.1-1] Hz	80

We calculated the correlation coefficient for synthetic SO and HPS compared with the synthetic earthquake signal for different SNR and noise realizations and plotted it in Figure 3.4a. The high correlation coefficients for HPS and synthetic compared with SO and synthetic in all cases demonstrate a significant noise reduction. Furthermore, they indicate that the HPS denoising preserves the earthquake signal and does not introduce significant waveform distortions since the HPS is more similar to the synthetics compared to SO. In the following we show other measures that confirm the preservation of the earthquake signal.

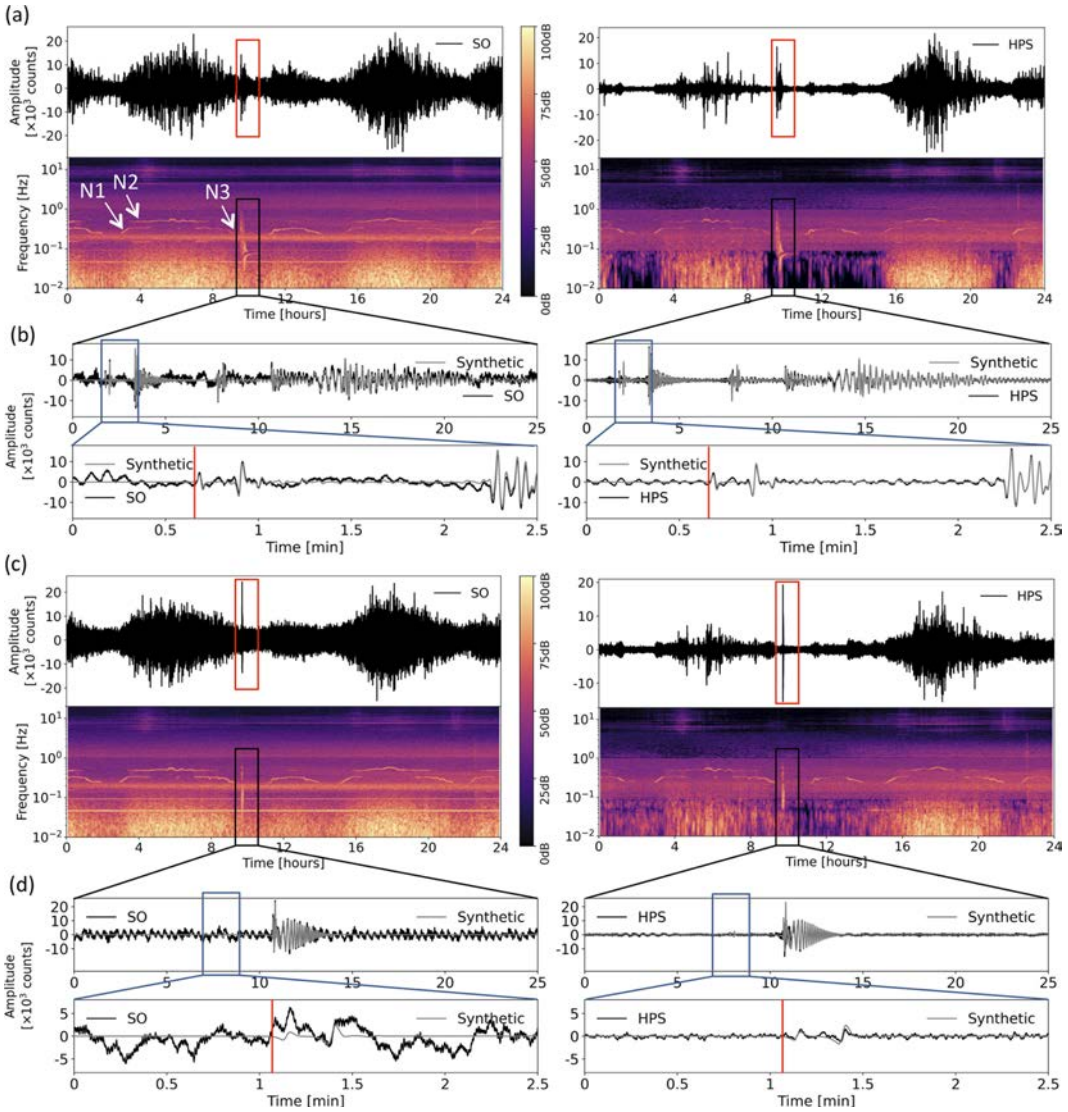

Figure 3.3. Comparison of the synthetic seismograms and spectrograms of the original signal SO and the HPS noise-reduced signal on the R and T components for a synthetic signal with SNR = 1.5 before denoising. Panels (a) and (c) show 1 d seismograms and spectrograms for R and T components, respectively. Squares show the earthquake section. The arrows in (a) show three noise situations (N1–N3). Panels (b) and (d) show seismograms of the earthquake section on SO and HPS signals, with a detailed view of the P arrival (on component R in b) and SH arrival (on component T in d). Red lines show P arrivals in (b) and SH arrival in (d).

For the SNR calculation we used a signal window of 30 s starting from the theoretical onset (direct P on Z component, direct S on R and T component, and Love wave on the T component) and a noise window of 60 s starting 70 s before the theoretical onset. For the Love wave, the SV phase (R component), and P phase (Z component) the SNR increased significantly (Figure 3.4b). We find that the noise type properties influence the perceived SNR improvement. It appears that there is no SNR improvement on the T component for noise situation N1 (Figure 3.4b, the second panel). N1 is taken from the tidal current event's beginning, where there is a significant variation in noise frequencies over time. In this instance, the signal and noise have comparable frequency ranges. Despite the SNR showing no increase, a visual check of the matching trace reveals a definite improvement in the waveform for the SH wave on the T component. The results from the cross-correlation (Figure 3.4a) confirm the improvement and preservation of the waveform. The SNR should not be utilized alone to assess the improvement by the HPS noise reduction approach since we are concentrating on the preservation of the

waveform and the SNR comparison strongly depends on the noise situation. The improvement of the traces by the HPS noise reduction approach is confirmed by the study of the cross-correlations, rms (which is explained in the following paragraph), and the pure waveforms, even though the SNR does not improve in all instances.

The rms amplitudes of noise-free R-component synthetic, SO, and HPS signals are estimated over 8 s windows with 80 % overlap and plotted in Figure 3.4c. Comparing the rms amplitude of the synthetic, SO, and HPS we see that the synthetic and HPS have similar amplitude ranges, while SO has a much higher amplitude. This shows a significant noise reduction in HPS along with preserving the energy of the earthquake and all the phase arrivals. As there is some noise remaining after denoising we see some differences in the overall shapes of the rms amplitude of the synthetic and HPS (especially after minute 24, which is almost at the end of the energy of the synthetic signal). However, HPS shows peaks on the arrival times of seismic phases of the synthetic, which means that the energy of seismic phases is preserved after denoising. The minor changes in seismic phase shapes of the synthetic and HPS are also due to the remaining noise. The seismograms and spectrograms related to this example are presented in Figure 3.3. Figure 3.4d shows a comparison of the rms amplitude of the original noise in SO (blue curve), the remaining noise in HPS after denoising (red curve), and the synthetic earthquake (green curve) signals. Besides a high noise reduction in HPS, the plot shows that the remaining noise is independent of the pattern of the synthetic earthquake, which confirms that the denoising process does not affect the earthquake energy in the HPS signal.

3.4.2 Applications

By applying our HPS noise reduction algorithm, we aim to improve seismological analyses, especially those involving the analysis of teleseismic body and surface waves. Valuable constraints of the Earth's structure in oceanic regions can be taken from the analysis of the SH wave field like Love waves, which are not influenced by the water column, but often cannot be analyzed due to strong noise on the horizontal components. SV waves are also often masked by noise but are, for instance, important for tomography studies or S and SKS shear wave splitting analysis (e.g., Silver and Chan, 1991). Other techniques using the SV wave field like the Z / R ratio of the teleseismic Rayleigh waves (Tanimoto and Rivera, 2008) or receiver functions (RFs) (Langston, 1979) also rely on clear radial component readings. In the following we will show the improvement which was achieved for the SH arrivals and for the group velocity analysis of teleseismic Rayleigh and Love waves, as well as for the receiver function analysis.

3.4.2.1 SH waves

Since SH waves are weak in energy and displayed on the noise-contaminated transversal horizontal component (T), they are sparsely observable on OBS recordings and are mostly masked by the high noise level. However, on the HPS processed data we see an improvement of the SNR on the T component (see Figure 3.4b). In many cases the SH phase is clearly identifiable on the HPS T component (see Figure 3.3d for a synthetic data example and Figure 3.12 for a real data example).

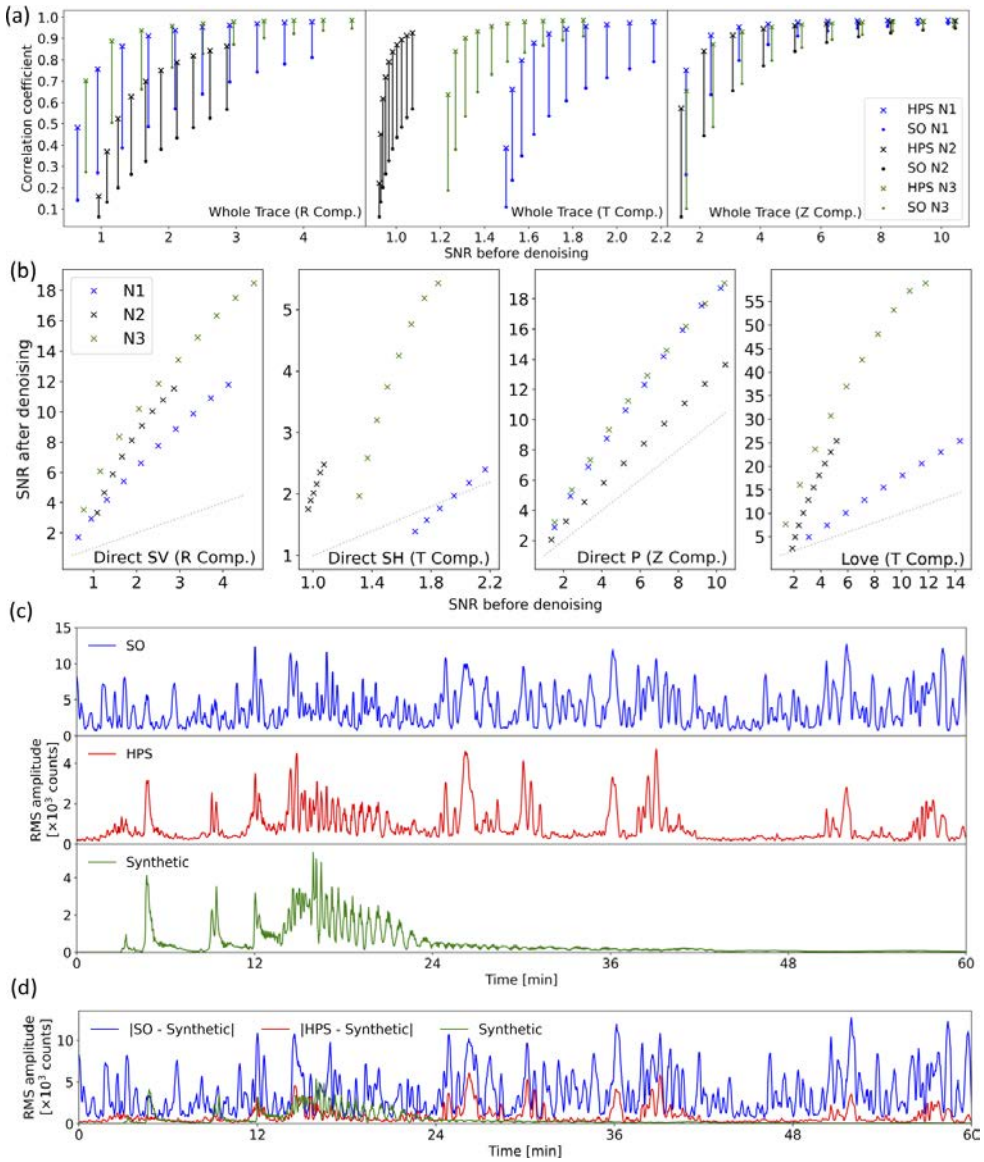

Figure 3.4. Comparison of the synthetic SO and HPS signals (both are low-pass-filtered at 1 Hz). (a) Correlation coefficients (for the whole trace) for different SNRs and three realistic noise realizations for Z, R, and T components (component is abbreviated as Comp.). (b) Improvement of SNR for direct body-wave phases and the Love wave. The gray dotted lines in (b) mark the line with gradient 1 (no improvement of SNR). (c) Comparison of the root mean square (rms) amplitude of one example of the SO, HPS, and synthetic earthquake signals. This signal is the same example shown in Figure 3.3 (R component, SNR = 1.5 before denoising). (d) The rms of the original noise (blue trace: | SO – synthetic |) and the remaining noise after denoising (red trace: | HPS – synthetic |) compared to the synthetic earthquake signal.

3.4.2.2 Surface waves

Rayleigh waves in deep oceanic domains are strongly influenced by the water column because most of the wave energy is traveling in the water. This poses a problem if the water depth changes along the travel path. Love waves are not influenced by the water column but are recorded only on horizontal components, and their recordings on OBS systems are therefore more disturbed by strong noise sources like tilt-inducing tidal currents. To test the performance of the HPS noise reduction algorithm in the low-frequency range, we performed a measurement of group velocities of Love and Rayleigh waves with the multiple filter technique (MFT) (Dziewonski et al., 1969). Figure 3.5 shows group velocity curves for the synthetic Love wave train for the three noise situations N1–N3. For the MFT analysis we used the software mft96

(Herrmann, 2013). The unfiltered seismograms in the top panels (Figure 3.5a–c) correspond to the P-wave SNR = 1 scenario. In all three cases the clarity of the dispersion curve is greatly enhanced in the images resulting from the HPS-processed traces (Figure 3.5e–g) in comparison to the noise-free image (Figure 3.5d). Also, the seismogram traces improved greatly. The dispersion images show how noise energy is successfully removed from the frequency range of 0.05 to 0.2 Hz, which is the event frequency range. The lower-frequency range, which is weakly visible in the noise-free image (Figure 3.5d), cannot be recovered. The corresponding results for the Rayleigh wave train on the radial component are shown in Figure 3.13. For the N3 case the low-frequency range down to 0.025 Hz can also be successfully denoised.

For an evaluation of the HPS denoising technique on real surface wave data we selected 23 events with magnitudes larger than M_W 6.0 in the distance range between 47.5 and 159.6° and added one event with M_W = 5.6 at a distance of 37.9° (see Figure 3.7). Figure 3.14 shows seismograms and MFT analysis examples for three events with different magnitudes and in different distances. The resulting group velocity dispersion curves for all 24 events for the original and processed data are shown in Figure 3.15. For all components we find that the improved signal-to-noise ratio of the processed data allows the analysis of more events and of a broader frequency range than in the original data.

3.4.2.3 Receiver functions

Receiver functions have been proven to be a valuable tool to observe the Earth's structure using teleseismic events (e.g., Langston, 1979; Ammon et al., 1990; Kind et al., 1995; Rondenay, 2009). Separating the source site from the receiver site by deconvolution allows estimating the Earth's structure beneath the station. Here, we compare the receiver functions calculated from the synthetic examples and from real data before and after denoising (Figure 3.6). The synthetics used for the receiver function calculation are pure synthetic signals contaminated by real noise (N1, N2, N3). On the synthetics, the SNR for P ranges between 1 and 10 (for a detailed description of the synthetic creation, see Section 3.4.1, Figures. 3.3 and 3.8). Receiver function analysis and the observation of the Earth's structure beneath the DOCTAR array were already conducted by Hannemann et al. (2017). Here, we do not aim to estimate the crustal and mantle structures; instead, we aim to compare the P-receiver functions of the radial component calculated from the original synthetic and real data (SO R- RF) with receiver functions of the radial component from the HPS processed synthetic and real data (HPS R-RF). To calculate the receiver functions, we applied the iterative deconvolution in the time domain (Ligorría and Ammon, 1999). We corrected the data for the Ps phase, quality-controlled (e.g., P onset at 0 s on Z of HPS R-RF), stacked, and low- pass-filtered the synthetic data at 2 Hz, and bandpass-filtered the traces between 0.05 and 0.5 Hz for the real data with a zero-phase Butterworth filter. For both the synthetic and real receiver function, the noise level strongly decreased, and we observe a significant decrease in variance on the HPS traces compared to the SO traces (Figure 3.6).

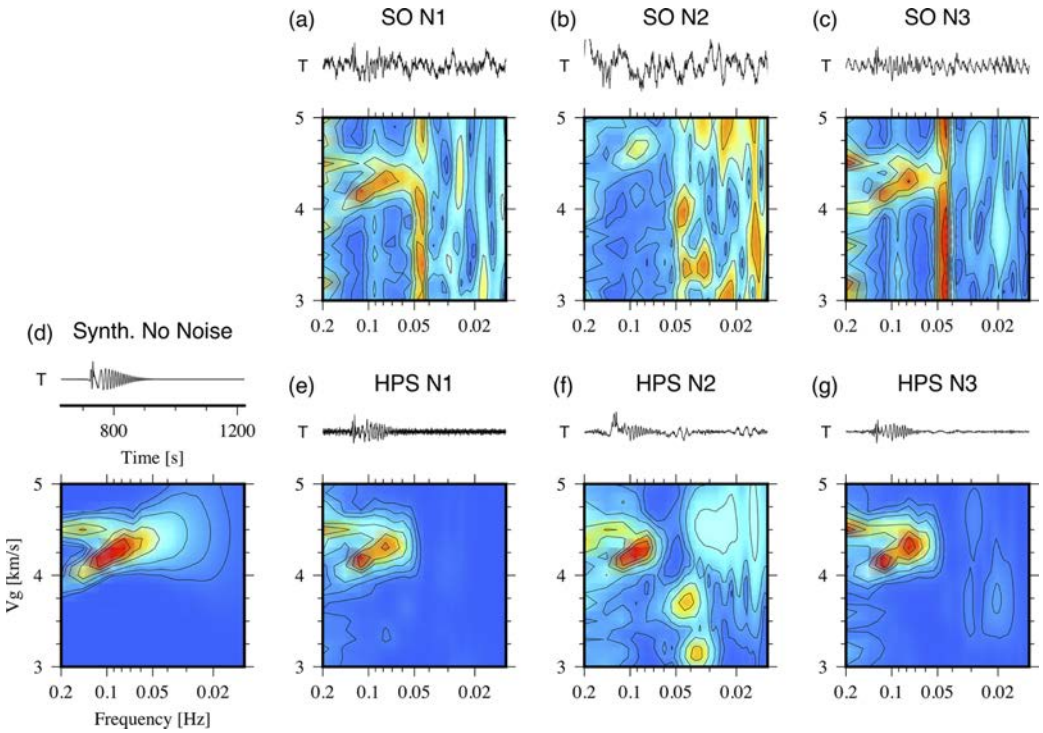

Figure 3.5. Love-wave group velocity analysis for unfiltered and HPS-processed synthetic Love wave trains contaminated by three real-world OBS noise signals (noise situations N1–N3, station D10, DOCTAR experiment, see Section 3.2 for more details). Lower panels in (a)–(c): unfiltered synthetic signal (SO) MFT analysis results. Top panels: seismogram time windows corresponding to the range of group velocities shown on the y axis. (d) Noise-free synthetic case. (e)–(g) HPS-processed input traces for noise situations N1–N3 (lower panel: MFT analysis result, top panel: HPS processed seismogram).

Our result shows that determination of the crustal and mantle phases is more reliable on the HPS R-RF stack than on the SO R-RF stack for both synthetic and real data (Figure 3.6). We observe more distinct Ps-phase arrivals on the HPS R-RF than on the SO R-RF stack. The Ps phases are caused by the P-to-S conversion at the Mohorovic˘ic´, 410, and 660 km discontinuity (hereafter referred to as Moho, 410, and 660, respectively; e.g., Deuss, 2009). For the synthetic example, we expect the P-to-S conversion at the Moho at depths of 11.5 km to arrive at 0.8 s, which is better resolved in the synthetic HPS R-RF than in the synthetic SO R-RF; the same is true for its multiple (P_{MsPp}) and the water multiples every 6.5 s (M_{WATER}, Figure 3.6a).

Assuming ak135 velocities we would expect the $P_{410}s$ phase (Ps conversion at the 410) to arrive at around 43 s and the $P_{660}s$ phase (Ps conversion at the 660) at around 66.8s delayed compared to the direct P arrival (see Figure 3.6a and b).

Instead of a rather weak peak on the SO R-RF real data stack we observe a strong peak at around 43 s, with a good SNR on the HPS R-RF stack, indicating the sharp velocity contrast at the 410 (Figure 3.6b). Comparing SO RF and HPS RF real data stacks, the amplitudes of the P660s phase on the HPS decreased and became a broader peak. This aligns with our expectations from a conversion at a gradual velocity contrast as at the 660. These results are in line with the analysis of the crustal and mantle structure beneath the DOCTAR array presented by Hannemann et al. (2017). The negative phase (X1 in Figure 3.6b) arriving at around 5 s is stronger on the HPS R-RF real data stack than on the SO R-RF real data stack and might indicate either the PpSs multiple of the Ps phase at the Moho or the direct P-to-S lithosphere–asthenosphere boundary (LAB). On the HPS R-RF real data stack we observe a strong positive phase (X2) arriving at 12 s (Figure 3.6b). This phase was not identified by Hannemann et al.

(2017), and a detailed analysis of its origin is beyond the scope of this study, but it might be related to the water multiples.

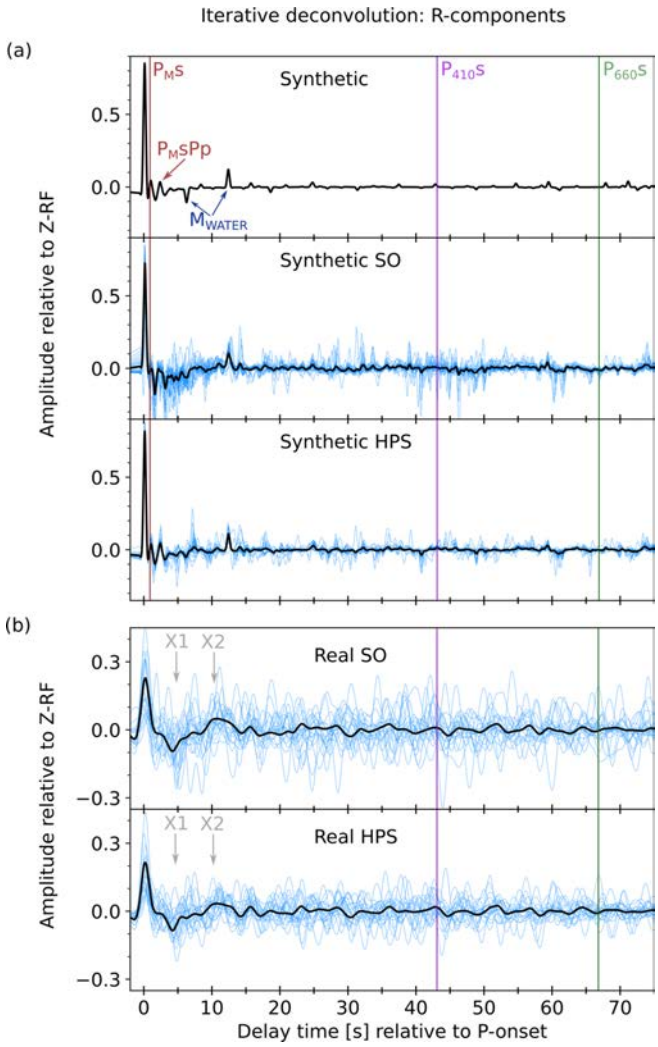

Figure 3.6. R-receiver function comparison of synthetic and real data examples. (a) Comparison of the synthetic data examples, low-pass-filtered at 2 Hz. The pure synthetic R-RF is shown in the upper-most panel, followed by the synthetic SO and the synthetic HPS R-RFs. The black lines show the summed individual R-RFs (blue waveforms). The theoretical onset times for this specific model are marked. Red line: Ps arrival of the Moho (PMs) and its multiple (PMsPp), violet line: Ps arrival of the 410 (P410s), green line: Ps arrival of the 660 (P660s), dark blue arrows: multiples in the water column of 4.9 km (MWATER), repetitive every 6.5 s. (b) Comparison of the real data, bandpass-filtered at 0.05–0.5 Hz. The upper panel shows the R-RFs of the real SO traces and the lowermost panel the R-RFS of the real HPS traces. The individual traces (blue) are shown as a stack (black line), and the theoretical onset times based on the average ak135 velocity model are shown as a violet line (P410s) and green line (P660s). The origin of the phases X1 and X2 (gray) remains unclarified, since their interpretation is beyond the scope of this study.

3.5 Conclusions

In this work we have developed a method to separate the signals of teleseismic earthquakes from other signals in OBS recordings, resulting in noise reduction of OBS data. Our method is a combination of two HPS algorithms from the field of music information retrieval (MIR) to separate harmonic and percussive components of OBS data. Earthquake signals as percussive components are separated from noise signals as harmonic components. The noise signal is reconstructed using the phase information of the original signal. Subtracting the noise signal

from the original signal derives the noise-reduced signal. Our two-step HPS approach results in a cleaner, noise-reduced signal wherein the teleseismic broadband earthquake waveforms are preserved with their whole frequency content. Our synthetic tests show that the SNR of HPS noise-reduced signal significantly increases in most cases; however, the apparent SNR improvement depends on the noise type characteristics. The types of noise signals, which are eligible for our noise reduction algorithm, contain most of the OBS noise energy.

The extracted noise signal contains some different signals; each can be derived by applying a bandpass filter to the extracted noise signal in a proper frequency band. The derived signal may be used in research related to that signal. For example, the microseism signal can be extracted and used for investigation of the source generation area of microseisms.

From our analysis of the broadband seismograms, we find that the improvement is significant and allows a broader and more reliable analysis of teleseismic earthquake data. Applications like the receiver function technique as well as SH-wave and Love-wave analysis are considerably improved after applying the HPS noise reduction algorithm.

Group velocity analysis of teleseismic surface wave trains showed that application of the HPS noise reduction technique allows analyzing more events and analyzing them in a broader frequency range. More and wider Love-wave dispersion curves could be recovered. The noise reduction algorithm improves the horizontal components significantly, which allows the OBS community to apply a broader range of seismological methodologies, including the horizontal components, to the OBS data.

Code and data availability

A Python package named NoiseCut (https://doi.org/10.5281/zenodo.7339552, Zali, 2022) and the code related to the proposed method along with an example of real data are freely available from https://github.com/ZahraZali/NoiseCut (last access: November 2022). The average computation time for this example (1 d OBS signal with a sampling frequency of 100 Hz) is about 7min on a PC with an Intel core i7 (six-core) processor of 2.2 GHz and 16 GB of RAM. A Jupyter notebook with all the Python codes and parameters related to the proposed method is available as an electronic Supplement. The seafloor seismological data were archived by the Alfred Wegener Institute (AWI), Helmholtz Centre for Polar Research, Bremerhaven, Germany, and are available upon request. The Supplement related to this article contains a list of all earthquakes used in this study and a map showing their location. The illustrations of the semi-synthetic data generation are presented in the Supplement as well. Examples of a three-component seismogram and spectrogram before and after applying the HPS noise reduction algorithm to real data, Rayleigh-wave group velocity analysis for a synthetic example, MFT analysis for three real events, and group velocity curves for some real events are also presented in figures in the Supplement. For building our method, we used Librosa, a Python package for audio and music signal processing (https://doi.org/10.5281/zenodo.7657336, McFee et al., 2023). The data processing was done using obspy (Beyreuther et al., 2010) and pyrocko (Heimann et al., 2017); the receiver functions were calculated using the rf package (Eulenfeld, 2020).

Acknowledgements

The seafloor seismological data were archived by the Alfred Wegener Institute (AWI), Helmholtz Centre for Polar Research, Bremerhaven, Germany, and are available upon request. We acknowledge the DEutscher Geräte-Pool für Amphibische Seismologie (DEPAS) (Schmidt-Aursch and Haberland, 2017) that is currently the largest European OBS pool. We acknowledge Sebastian Heimann for helping package the code related to the method. The authors would like to thank the editor Simone Pilia and two anonymous reviewers for their insightful comments.

3.6 Appendix

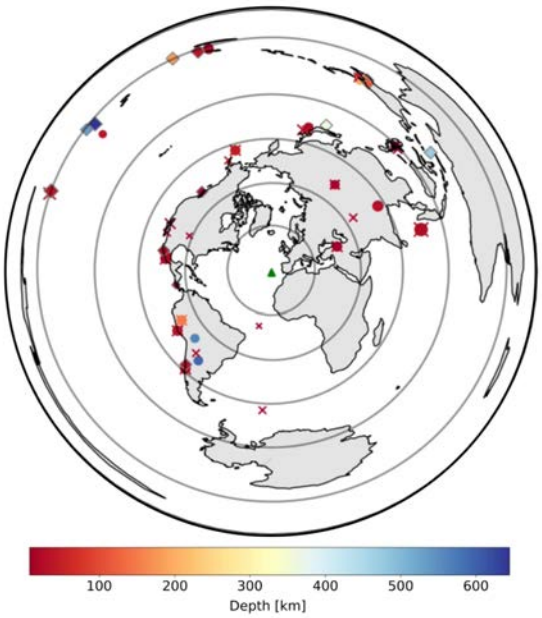

Figure 3.7. Location map of the events used in this study. The 46 events are colorized according to their magnitude Mw. Events used for the Receiver Function analysis (20 events) are marked by colorized circles and events used for the Surface-wave analysis (24 events) are marked with colorized crosses. Other events are marked by colorized diamonds. The D10 station (green triangle) is located in the center and the grey circles indicate the epicentral distances (30-160°) from the D10 station. The D10 station is one of in total 12 stations of the DOCTAR array around the Gloria fault in the North Atlantic.

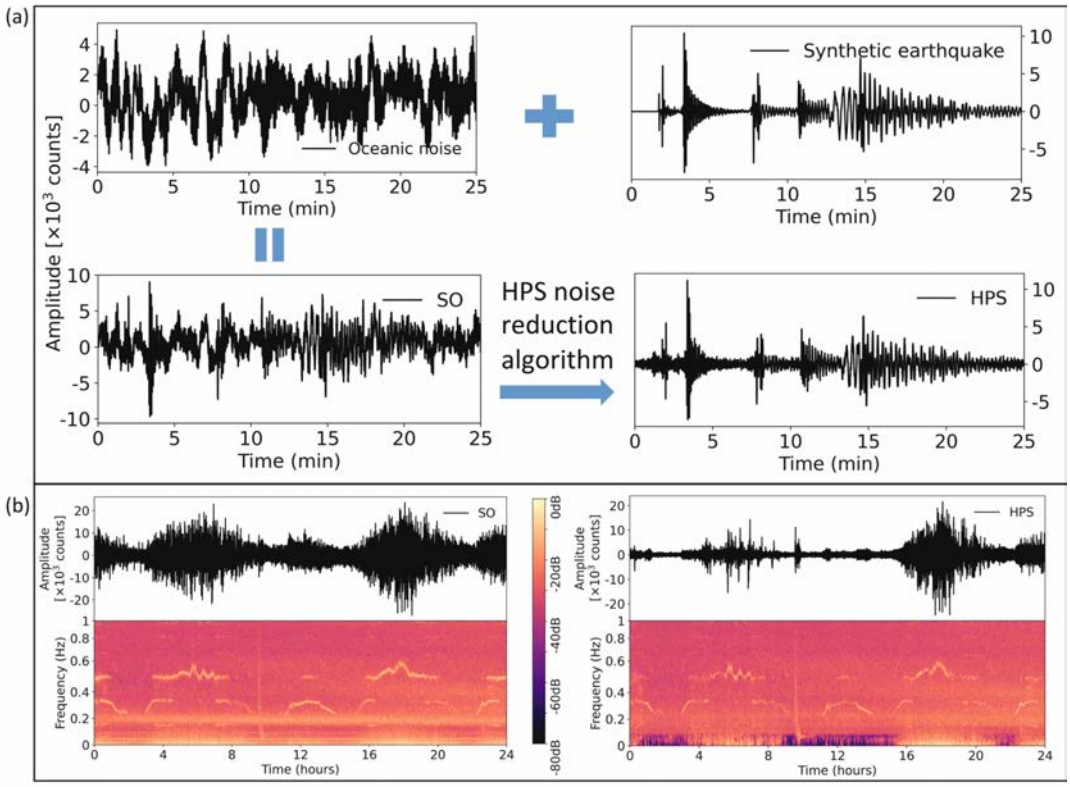

Figure 3.8. The process of synthetic signal generation with an example of the method application on synthetic data. (a) Shows a synthetic earthquake signal, which is summed with a real world oceanic noise waveform and resulted in the synthetic SO signal. The SNR of SO is 1 in this example. After applying the HPS noise reduction algorithm the HPS noise reduced signal is generated. (b) Shows one day synthetic signal (SO) and HPS noise reduced signal (HPS) along with their spectrograms.

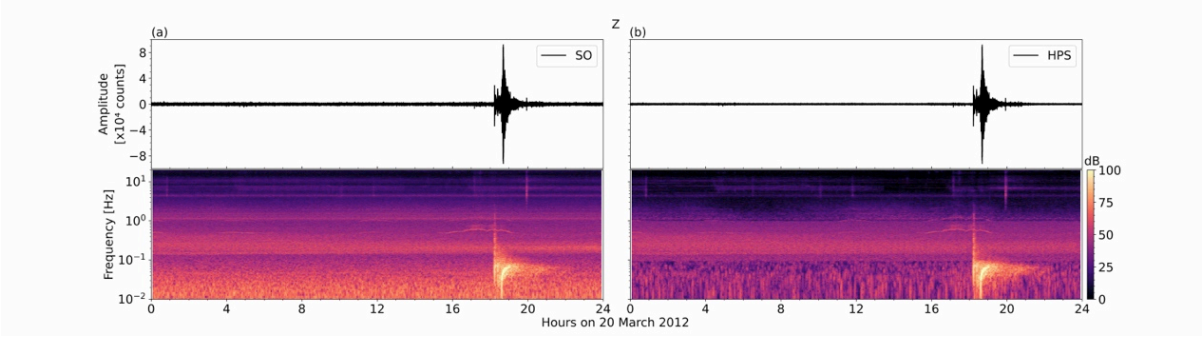

Figure 3.9. Comparison of the seismograms and spectrograms of the original signal SO (a) and the HPS noise reduced signal (b) on the Z component for real data. The upper panels show the seismograms and the lower panels show the spectrogram. The sampling rate of the data was 100 Hz and the spectrogram was calculated with a window length of $\mathbf{2^{16}}$ samples. The spectrogram clearly shows the reduced noise level on the HPS signal.

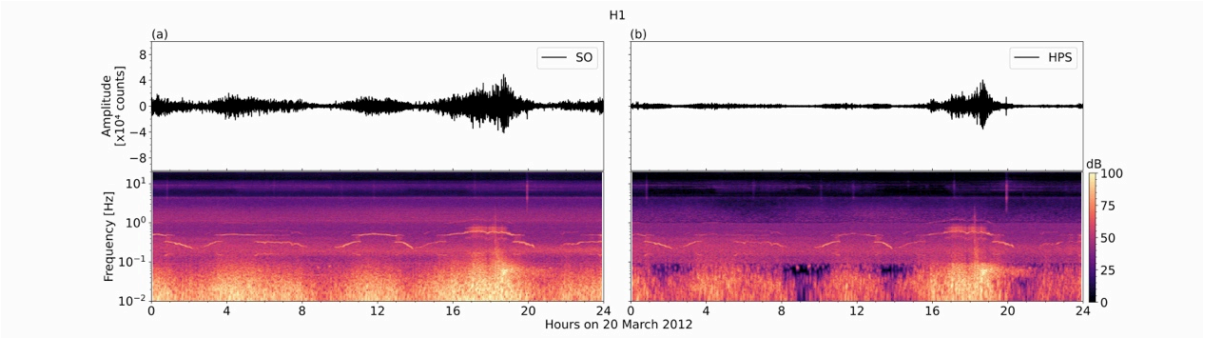

Figure 3.10. Comparison of the seismograms and spectrograms of the original signal SO (a) and the HPS noise reduced signal (b) on the H1 component for real data. The upper panels show the seismograms and the lower panels show the spectrogram. The sampling rate of the data was 100 Hz and the spectrogram was calculated with a window length of $\mathbf{2^{16}}$ samples. The spectrogram clearly shows the reduced noise level on the HPS signal.

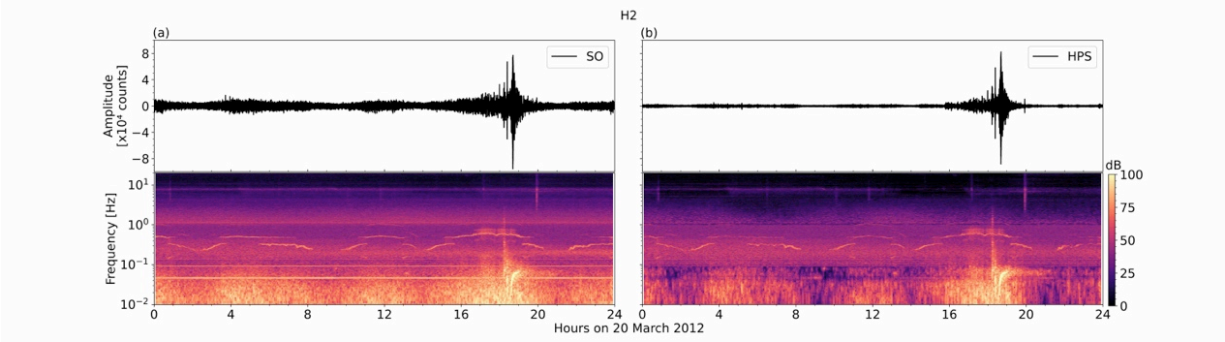

Figure 3.11. Comparison of the seismograms and spectrograms of the original signal SO (a) and the HPS noise reduced signal (b) on the H2 component for real data. The upper panels show the seismograms and the lower panels show the spectrogram. The sampling rate of the data was 100 Hz and the spectrogram was calculated with a window length of $\mathbf{2^{16}}$ samples. The spectrogram clearly shows the reduced noise level on the HPS signal.

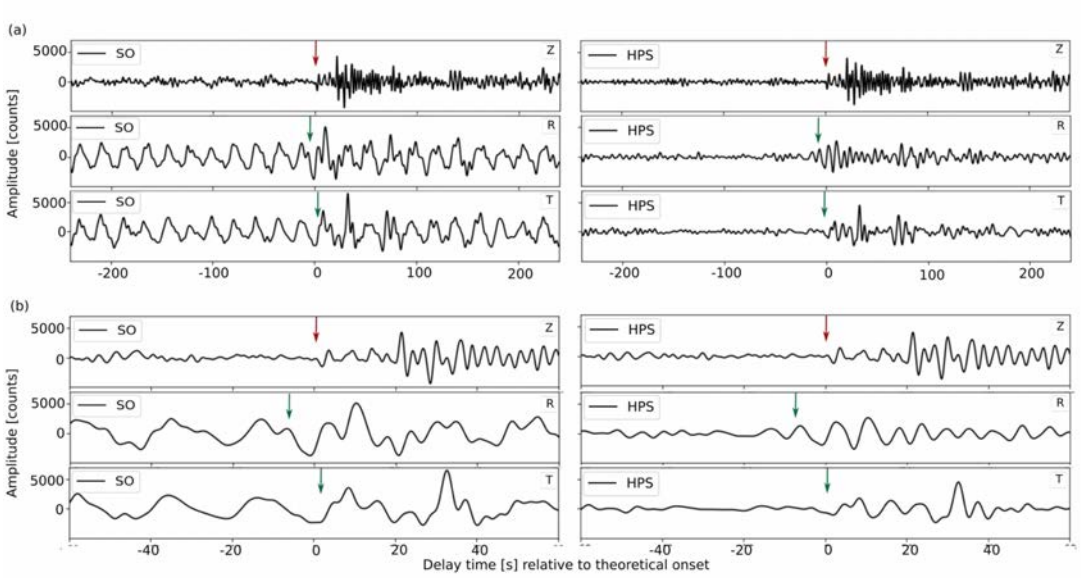

Figure 3.12. Comparison of the real data ZRT traces of the input SO and the resulted HPS noise reduced signal. The traces are zerophase bandpass filtered between 0.025-0.25 for S waveform (R- and T-component) and 0.025-0.5 for P waveform (Z-component). (a) Seismogram of SO and HPS noise reduced +/- 4 minutes from the theoretical P-onset. (b) Detailed view of the P- and S-arrivals (red and green arrows, respectively). It shows unchanged waveforms of the P- and S-phases on Z, R and T, respectively. The traces are plotted +/- 1 min from the theoretical P- and S-arrival on Z, R and T, respectively.

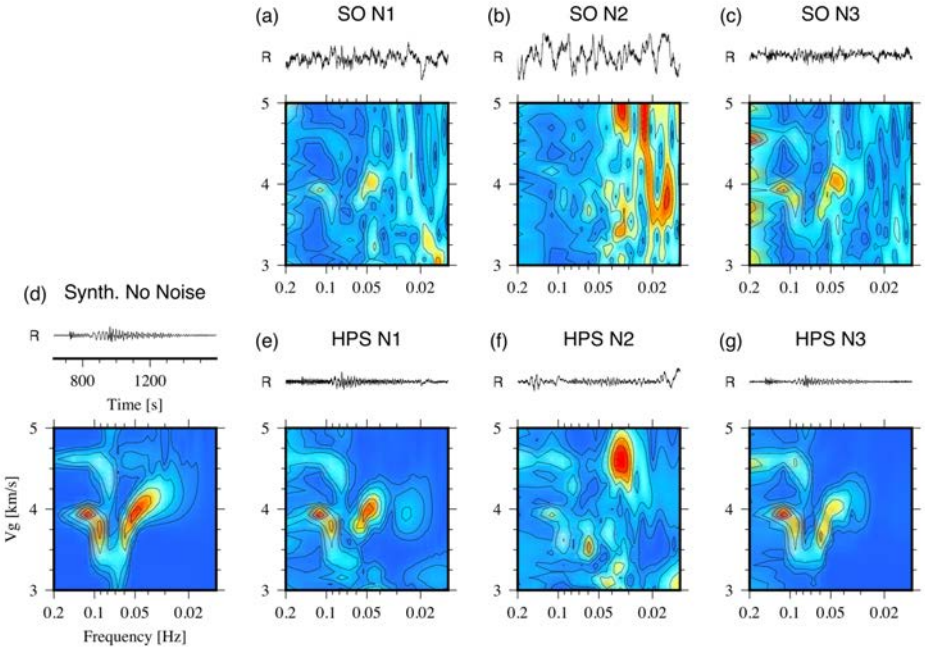

Figure 3.13. Rayleigh wave group velocity analysis for unfiltered and HPS processed synthetic Rayleigh wavetrains contaminated with three real world OBS noise signals (noise signals N1-N3, station D10, DOCTAR experiment, radial component, see section 3.2 for more details). (a)-(c): Lower panels: Unfiltered synthetic signal (SO) MFT analysis results. Top panels: seismogram time windows corresponding to the range of group velocities shown on the y-axis. (d) Noise free synthetic case. (e)-(g): HPS processed input traces for noise situations N1-N3 (lower panel: MFT analysis result, top panel: HPS processed seismogram).

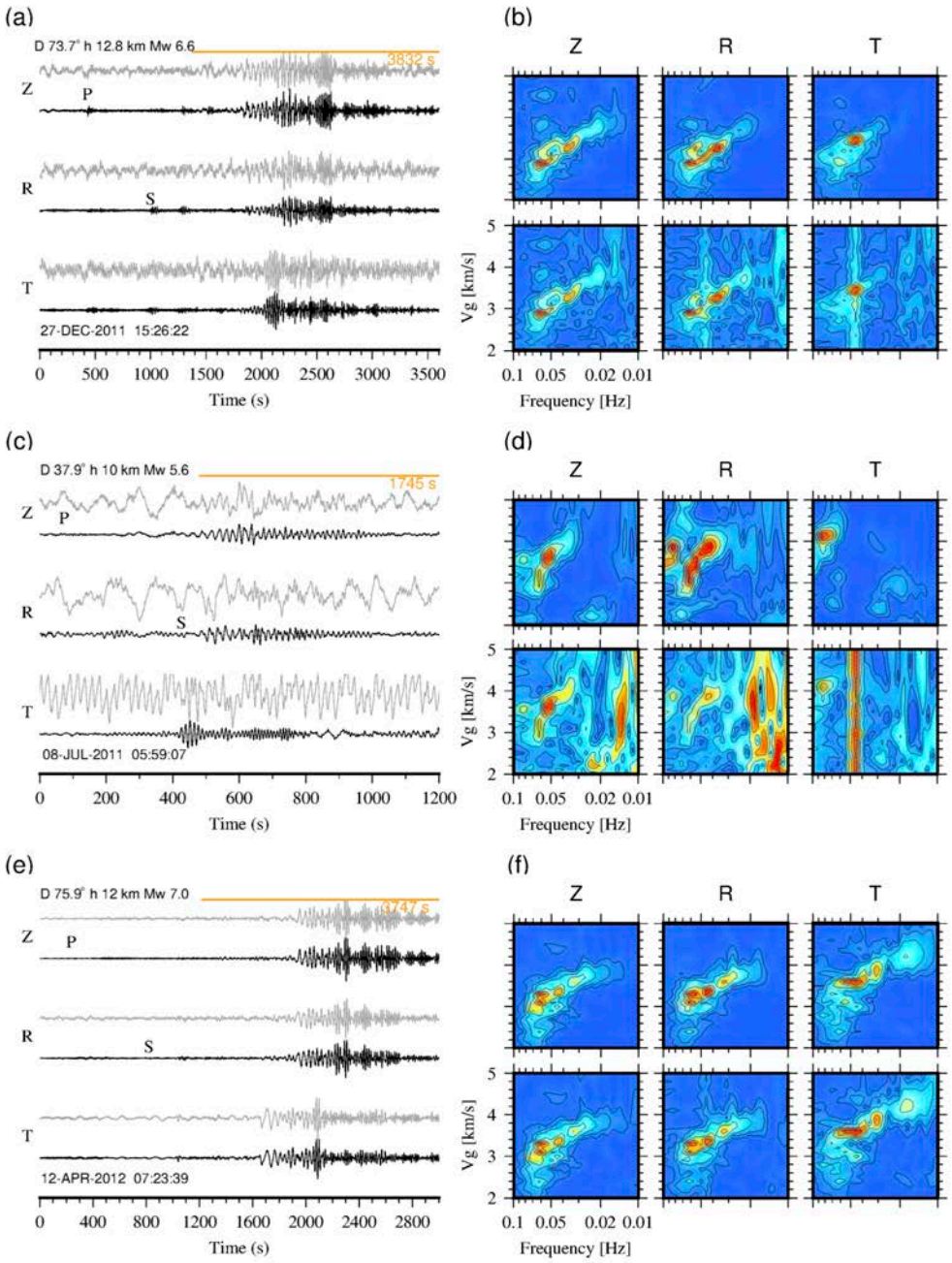

Figure 3.14. Seismogram and MFT analysis examples (similar to the software mft96 (Herrmann, 2013)) for real data. Panels (a), (c), (e) on the left show ZRT seismograms for three events (see table S1 for the event parameters). Traces were restituted to true ground velocity up to 100 s period and subsequently low pass filtered with a 3rd order Butterworth filter at 10 s. Unprocessed traces are shown in grey, HPS-processed traces are shown in black. The start time of the seismogram is marked on the lower left of each panel, event parameters are marked on the top left of each panel. An orange bar marks the time window encompassing the group velocity range used in the MFT analysis (the end time of the analysis window is given as number in orange). Panels (b), (d), and (f) on the right show the corresponding MFT results normalized to the maximum amplitude. In (b), (d), and (f) the panels in the upper row correspond to unprocessed and the panels in the lower row correspond to HPS-processed traces.

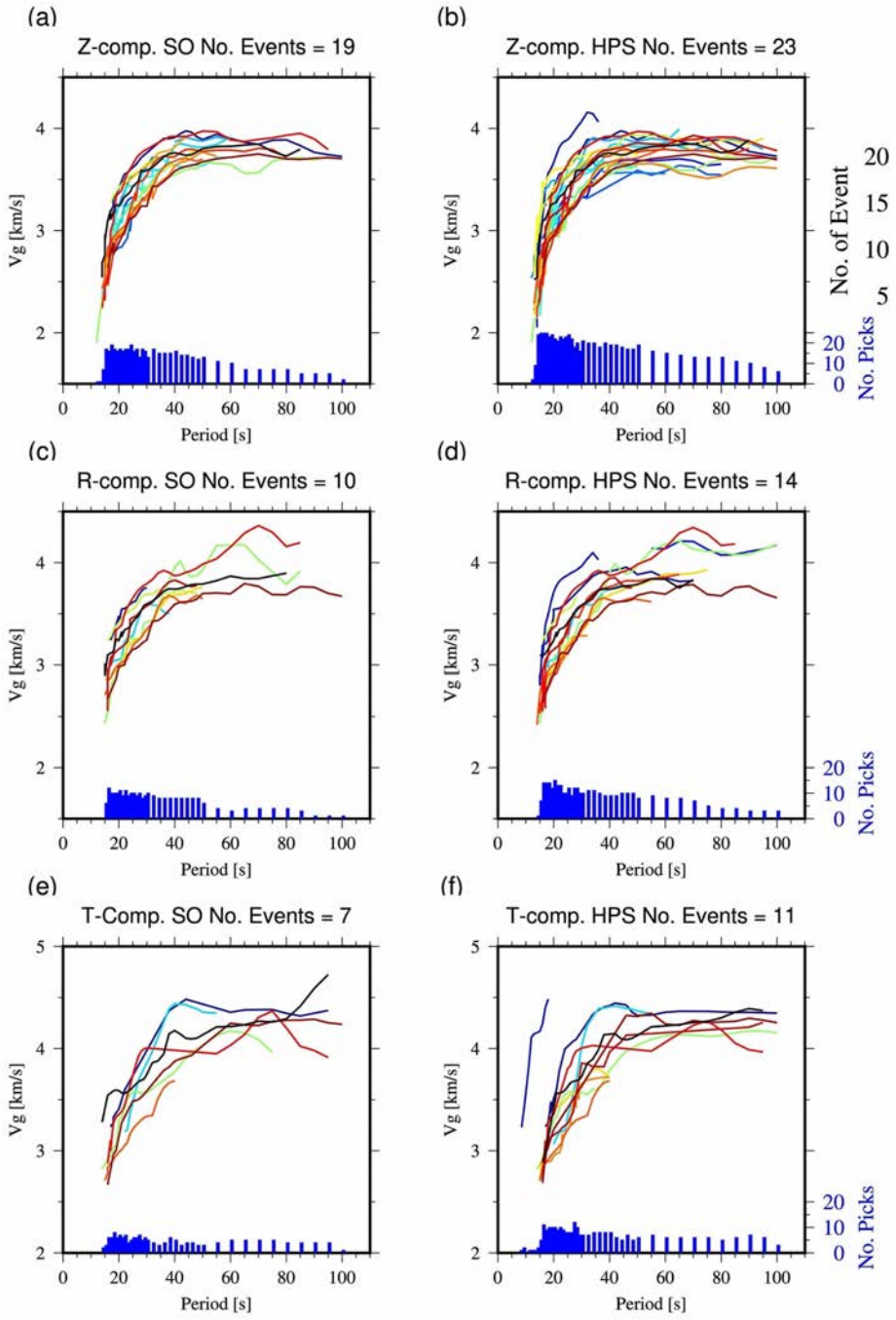

Figure 3.15. Picked group velocity curves for the events in Figure 3.7 (real data). The event number is color coded according to Table S1. (a) and (b) show results for unprocessed and HPS processed vertical component input traces, respectively. The histogram on the lower end of the panels displays the overall number of picks for a specific wave period. (c) and (d) are same for radial component. (e) and (f) are same for transversal component.

Chapter 4

Tremor clustering reveals precursors and evolution of the 2021 Geldingadalir eruption

Abstract

Timely manner seismic data processing and analyses are essential for potential eruption prediction and early warning in volcanology. However, the complexity of eruption processes and precursory activities makes the analysis challenging. Here, we show that advanced machine learning techniques can provide an effective and efficient tool for extracting overlooked information from continuous seismic signal recorded during the 2021 Geldingadalir eruption in Iceland and reveal the temporal evolution of the eruptive activity. We identify the major phases of the eruption based on observed seismic signals throughout the eruptive activity. We distinguish unrest activities, continuous lava extrusion, and different levels of lava fountaining. We discover a precursory volcanic tremor sequence starting three days prior to the eruption, which could be used as an indicator of imminent eruptive activity. Based on the extracted patterns of seismicity and their temporal variations we provide an explanation for the transition mechanism from vigorous outflow to lava fountaining. Our observation suggests that the transition to episodic tremors in the seismic signal in early May, could be a result of an increase in the discharge rate in late April.[a]

[a] In review as: Zali, Z., Mousavi, S. M., Ohrnberger, M., Eibl, E. P., Cotton, F. Tremor clustering reveals precursors and evolution of the 2021 Geldingadalir eruption, 05 May 2023, PREPRINT (Version 1) available at Research Square. https://doi.org/10.21203/rs.3.rs-2716246/v1

4.1 Introduction

With the development of new monitoring technologies and artificial intelligence, seismologists could detect the preparatory phase of volcanic eruptions and document the succeeding eruption phases. This study contributes to such an effort: continuous seismological data associated with the Geldingadalir 2021 eruption are analyzed with deep learning methods to discover overlooked patterns which were not reported using classical approaches, revealing the upcoming eruption and its evolution.

After 781 years of quiescence on the Reykjanes Peninsula, Iceland, a fissure opened near Fagradalsfjall on 19 March 2021 (Jonsson, 1983; Sæmundsson et al., 2020; Sigurgeirsson, 1995). The eruption was preceded by a sequence of seismic swarms and intrusion events on the Reykjanes Peninsula (Çubuk-Sabuncu et al., 2021, Geirsson et al., 2021) started by a week-long earthquake swarm on December 2019 (Sigmundsson et al., 2021). A magnitude 5.7 earthquake initiated the latest seismic unrest on 24 February 2021 (Fischer et al., 2022; Sigmundsson et al., 2021). After three weeks, the intrusion reached the surface, and the eruption began. Earthquake swarms often precede volcanic eruptions (Flóvenz et al., 2022). However, they also can occur due to non-eruptive activities (Benoit and McNutt, 1996; Farrell et al., 2009; Moran et al., 2011; Shelly et al., 2015). Contrary to the reported intense seismicity prior to the Geldingadalir 2021 eruption, no precursory volcanic tremor has been reported before this study (Barsotti et al., 2023). Persistent seismic signals precede and/or accompany most volcanic eruptions (Konstantinou & Schlindwein, 2003); hence, volcanic tremors can be seen as a geophysical precursor to predict eruptions.

Eruption forecasting as one of the ultimate goals of many volcanological studies is challenging due to the complexity and diversity of precursory activities (Chardot et al., 2015). Finding reliable precursory signals for volcanic eruption is thus a major topic in volcano seismology (Bean et al., 2014). Hence, detecting and analyzing the precursory volcanic tremors is of particular value for eruption forecasting and for a better understanding of the physical processes of volcanic eruptions (Chouet, 1996; Sparks, 2003). To highlight the temporal changes announcing the upcoming events, it is necessary to identify the main groups (clusters) of signals present in the continuous stream of recordings and to detect the relative presence of different groups over time.

Our result demonstrates that an autoencoder-based method can extract the salient feature of the seismic signals and potentially reveal hidden weak precursory volcanic tremors before the eruption. We use a Deep Embedded Clustering (DEC) approach (e.g. Mousavi et al., 2019 & Xie et al., 2016). This processing technique results in well-separated clusters of individual seismic signals associated with different phases of the volcanic system. Our clustering method provides an automatic distinction of different patterns in the seismic signal ranging from earthquake sections, different continuous tremors, and episodic tremors. This could provide valuable information about the temporal evolution of the volcanic system and times of the major changes such as the start of the eruption, discharge rate changes, and sequences of the system evolving and stabilizing. Here we focus on the pre and initial phases of the eruption (12 March to 24 June 2021).

4.2 Identifying seismic signature of different eruption phases

The 2021 Geldingadalir eruption features different volcanic processes such as pre-eruptive activities, continuous lava extrusion, and episodic lava fountaining. Our approach directly

explores the seismic signatures of major changes in the system status and introduces a chronology of the distinguished volcanic activities. We use seismic data from the east component of station NUPH (9F seismic network in Eibl et al. 2022b) located at 5.5 km southeast of the eruption site in Geldingadalir, Iceland (Figure 4.1a).

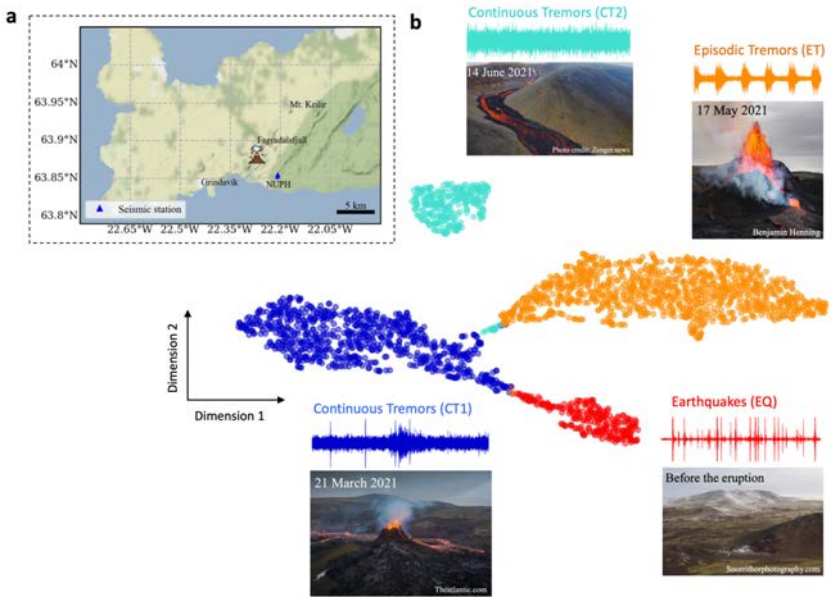

Figure 4.1. Overview of the eruptive site and different eruptive phases. a, Location of the eruptive site on the Reykjanes peninsula, Iceland and the seismometer. b, t-sne (t-distributed stochastic neighbor embedding is an unsupervised machine learning algorithm for visualizing high-dimensional data in a two or three-dimensional map) visualizations of seismic event clusters in feature domain resulted from deep embedded clustering. Seismic events in each cluster correspond to a specific phase of the eruptive activity. A sample 1-hour waveform (filtered 1-4 Hz) and a photo of the eruptive site in each cluster are shown with their corresponding cluster names.

We compute the Short Time Fourier Transform (STFT) of one-hour windows of the continuous seismic data filtered from 1 to 4 Hz. The salient features of the spectrogram are automatically extracted by the convolutional layers in an autoencoder. This autoencoder first maps the input STFT window to a low-dimensional latent representation in the feature domain and then uses these sparse feature representations to reconstruct the same STFT in the output layer. We apply a DEC technique in which the latent representation of the spectrogram is used for clustering. This approach ensures the extraction of the most useful features of the data for the clustering task by simultaneous optimization of feature extraction and clustering.

Using this processing approach, four clusters (EQ, CT1, ET, CT2), each associated with major phases of the volcanic activities (Figure 4.1b & Figure 4.2a), are identified. The EQ (earthquakes) cluster marks the intense seismic activity prior to the eruption. Samples in this cluster represent time windows of seismic signal when earthquake is the most dominant signal (Figure 4.2b&c). Most samples in this cluster start at the beginning of our data on 12 March and end before the start of the eruption (Figure 4.13a). Between the start of the eruption and 14 June we also see some windows of this cluster that contain earthquake signals (Figure 4.13b). Cluster CT1 (continuous tremors 1) initiates three days before the eruption and ends on 27 April (Figure 4.2d&e). This cluster represents the continuous tremors related to magma movement and lava outflow. The seismic waveform at this time features a narrowbanded tremor with the strongest frequency at 2.5 Hz. Cluster ET (episodic tremors) - from 27 April to 13 June - contains episodic tremors related to lava fountaining (Figure 4.2f&g). From 13 to 24 June,

cluster CT2 (continuous tremors 2) mainly contains continuous tremors with two dominant frequencies: a narrowband frequency of 1.2 Hz, and a broader and weaker frequency between 2 to 3 Hz (Figure 4.2h&i). The amplitude is higher compared to the continuous tremor in cluster CT1. Detailed information related to clusters and the volcanic processes linked with them are provided in the following.

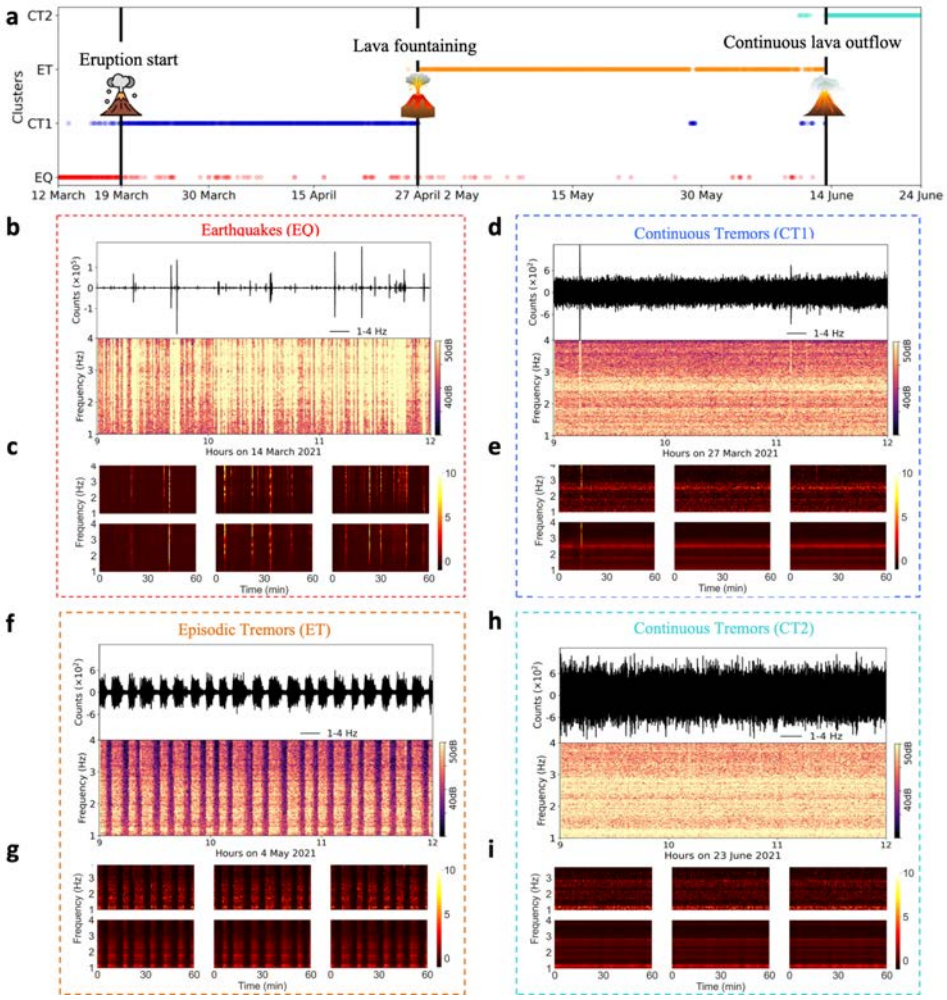

Figure 4.2. Chronology of the eruptive activity. a, Four identified clusters resulted from deep embedded clustering of the continuous seismic waveform in the study time period. b & c, Samples of data in the cluster EQ (earthquake). An example of a three-hour seismogram and the power spectrogram (window length of 16384 samples and overlap of 4096 samples) of data are shown in b. c presents three one-hour STFTs of seismograms as the inputs of the autoencoder (the first row) and the reconstructed outputs of the autoencoder (the second row) in this cluster. d & e, Same as b & c for the cluster CT1 (continuous tremor 1). f & g, Same as b & c for the cluster ET (episodic tremor). h & i, Same as b & c for the cluster CT2 (continuous tremor 2).

4.3 Observation of precursory volcanic tremors

Volcanic tremors play a significant role in volcano seismology since their pattern reflects the evolution of the eruptive activities (Alparone et al., 2003; Falsaperla et al., 2005; Privitera et al., 2003). Although volcanic tremors are well-established short-term (days to minutes) precursors to volcanic eruptions (e.g., Harlow et al., 1996; Hotovec et al., 2013; Sabit et al., 1996; Swanson et al., 1985), some eruptions have occurred without such apparent precursors (e.g., Castruccio et al., 2016; Larsen et al., 2009; Power and Lalla, 2010; Reckziegel et al., 2016). The 2021 Geldingadalir eruption initially has been reported to erupt without any

precursory tremor.

Using a more advanced technique, we were able to detect precursory volcanic tremors before the 2021 Geldingadalir eruption that were initially overlooked. This finding raises an important question of whether no observation of the precursory tremors in some eruptions was related to the data processing or an underlying physical mechanism. The result of DEC shows that tremors in cluster CT1 starts three days before the eruption (Figure 4.2a & Figure 4.14). An important finding here is that although the precursory tremor signals are weak and hidden beneath the stronger earthquake arrivals, the DEC technique can identify them.

To investigate this finding more closely we used a signal decomposition method, i.e., harmonic-percussive separation algorithm (Zali et al., 2021; Zali et al., 2023), and extracted the underlying volcanic tremor signal (Supplementary sheet 1). Figure 4.3a shows seismic signals and their spectrograms between 13 to 25 March where the volcanic tremors are visible after the start of the eruption on the evening of 19 March. However, we can clearly see the tremor signal starting on 16 March in the extracted tremor plot (Figure 4.3b). This confirms the observation of precursory tremors as revealed by the DEC algorithm. The spectrograms of the seismic waveform and the extracted tremors on 16 March, show that the precursory volcanic tremors started at noon of 16 March (Figure 4.3c). Sigmundsson et al., (2022) demonstrate that the high rates of seismicity and deformation, which started on 24 February due to magmatic intrusion, declined from mid-March to the start of the eruption. Tectonic stress release, less lateral magma migration, and emplacement of magma in the shallow weak crust explain this decline (Sigmundsson et al., 2022). Our observation of the precursory volcanic tremor on 16 March could also suggest that magma reached the shallow crust near the surface and indicate an upcoming eruption.

4.4 The eruption style changes

From 19 March until 27 April the eruption is characterized by low and stable effusion rate (Halldórsson et al., 2022; Pedersen et al., 2022). After 27 April the eruption style changed with an increased effusion rate (Halldórsson et al., 2022; Pedersen et al., 2022). From 2 May until 14 June, the eruptive activity is characterized by a sequence of lava fountaining (Eibl et al., 2023; Lamb et al., 2022; Pedersen et al., 2022) reflected as episodic tremors on seismic data (Figure 4.4b-e). Although the patterns of episodic tremors are clearly visible on raw seismic data from the beginning of the lava fountaining on 2 May, our clustering result indicates that ET tremors started earlier on 27 April at 5:00 (Figure 4.2a). This is due to the higher sensitivity of our processing approach confirmed by visual examination of the spectrograms that indicates presence of a subtle episodic pattern starting on 27 April (Figure 4.15).

The observation of a cluster change (CT1 to ET) and subtle episodic pattern from 27 April could indicate that the lava fountaining is triggered on 27 April by an increase in the magma flow rate. Since the major change in the system on 27 April is an increase in the discharge rate, we suggest that the discharge rate increase plays a key role in the shifting to episodic eruption behavior. On 13 June at 10:00, the ET cluster ends and the CT2 cluster starts with a dominating continuous tremor pattern. (Figure 4.2a).

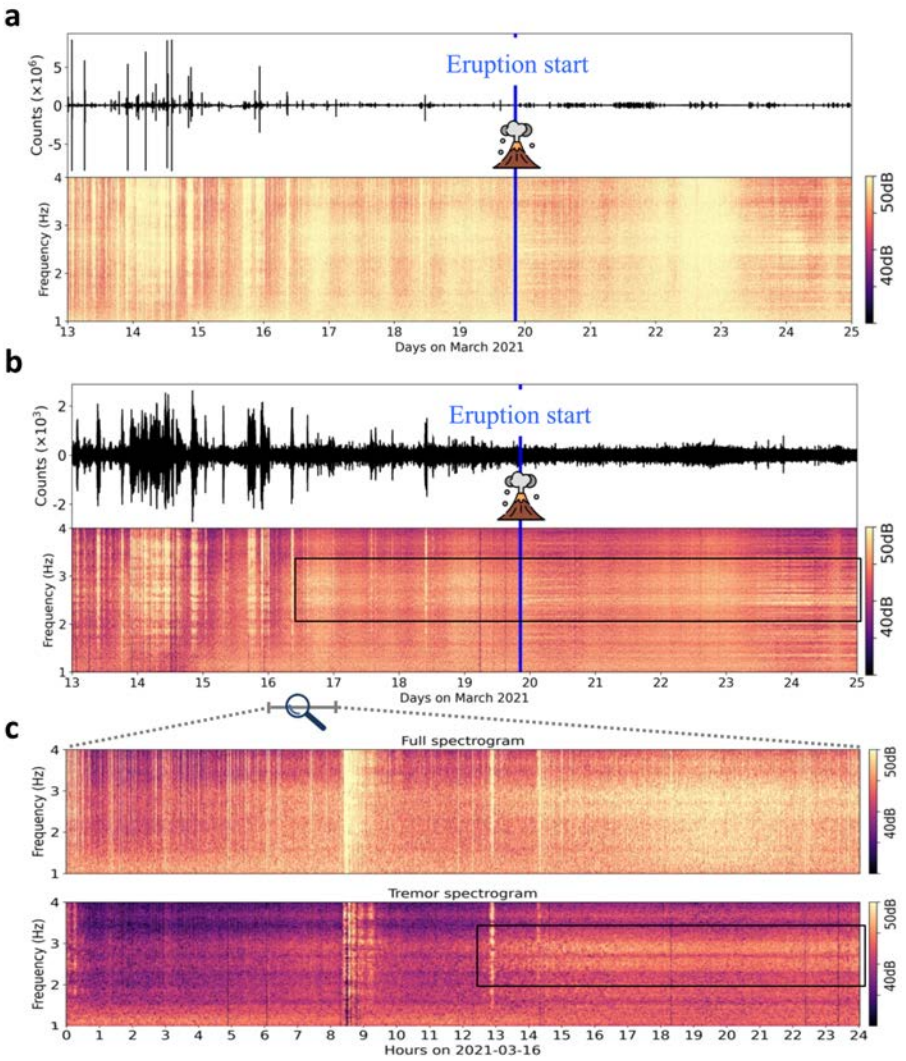

Figure 4.3. Discovered precursory tremor three days before the eruption. a, Seismic signal and power spectrogram (window length of 32768 samples and overlap of 8192 samples) between 13 to 25 March. The blue line marks the start of the eruption. b, Extracted tremor signal from the seismic waveform and the tremor spectrogram between 13 to 25 March using harmonic-percussive separation algorithm. The black box shows the extracted tremor starting on 16 March. c, Spectrogram of the original seismic signal and the extracted tremor on 16 March. The precursory tremor starts on the noon of 16 March. The black box shows the extracted tremor on 16 March.

4.5 The variations of fountaining episodes associated with the system status

Episodic tremors of the cluster ET show distinct patterns with different duration, repose time, and amplitude (Figure 4.4b-e). For a more detailed analysis of these episodic tremors, we performed another DEC of tremor episodes between 2 May and 14 June (lava fountaining period). This time, we used STFT of seven-minutes-long windows of the seismic signal starting from the onset time of episodes (Eibl et al. 2022a) as the input to our model. This process resulted in four clusters (ET-1, ET-1, ET-3, ET-4) and introduced four dates related to major changes in the system: 5, 11, 17 May and 10 June (Figure 4.4a). The general trend of clusters changes is in line with the detailed study of episodic tremors by Eibl et al., (2023) where they linked the evolution of episodic tremor patterns to an evolving shallow magma compartment, outgassed lava accumulating in the crater edifice and a widening conduit. The system status on the mentioned dates is discussed in Eibl et al., 2023.

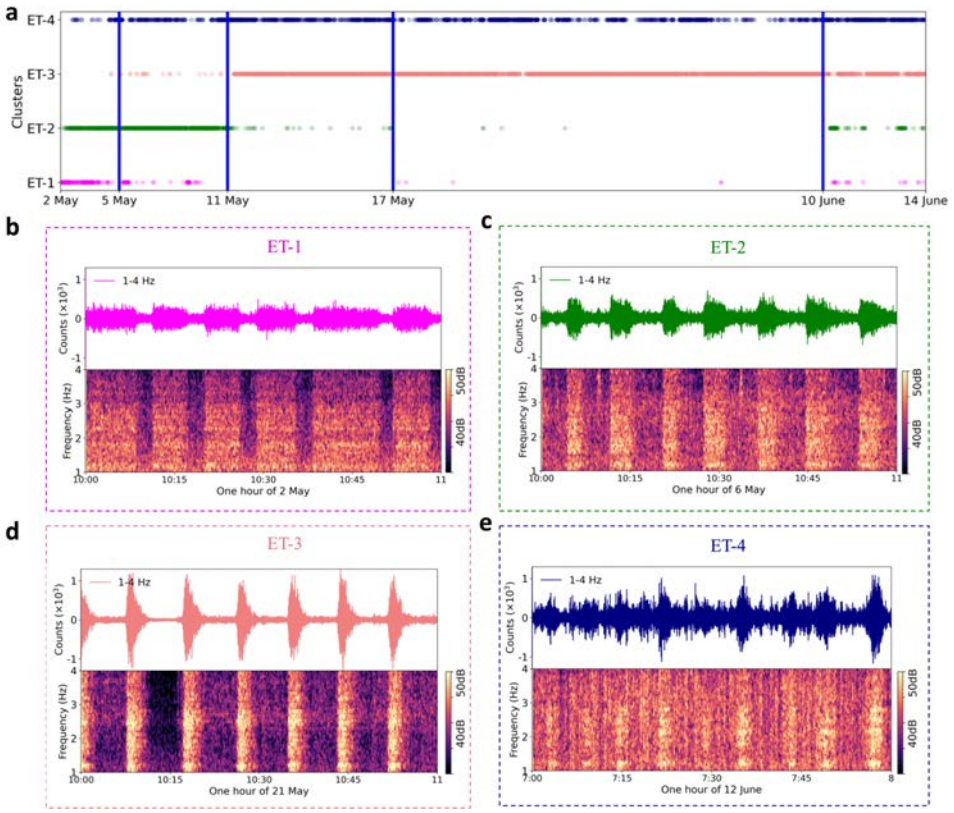

Figure 4.4. Chronology of lava fountaining. a, Four identified clusters resulted from deep embedded clustering of the episodic tremors. Each cluster represents episodes with different duration, amplitude, and frequency content. b, An one-hour example of seismic signal and the spectrogram (window length of 4096 samples and overlap of 1024 samples) of the cluster ET-1. c, Same as b for the cluster ET-2. d, Same as b for the cluster ET-3. e. Same as b for the cluster ET-4.

Cluster ET-1 starts on 2 May. The majority of data in this cluster exist until 5 May at 11:56 (Figure 4.4). This cluster contains episodes with a duration equal to 7 minutes or longer, with a dominant frequency around 1.2 Hz. The amplitude of the episodes is lower compared to other clusters. Cluster ET-2 contains episodes from 2 to 11 May (12:54) with mean duration of 4.5 minutes. The frequency content is similar to cluster ET-1 but the amplitude is larger. There are some episodes of this cluster between 11 to 17 May and between 10 to 13 June. Episodes in cluster ET-3 mainly start on 11 May at 15:55. They have mean duration of 2.8 minutes with a fundamental frequency around 1.4 Hz and first overtone around 2.8 Hz. The amplitude is higher compared to the other clusters. Most data in this cluster exist until 10 June but there are some samples until 13 June as well. Cluster ET-4 contains episodes with a mean duration of 3.3 minutes and frequency content similar to cluster ET-3 but with lower amplitude. This cluster covers most episodes after 10 June 3:39, but it also contains some episodes from 2 May onwards, mostly after 5 May.

The autoencoder extracts three features from the STFTs of episodes (Table 4.1) and DEC is performed using these three features. Visual inspection of raw data for individual clusters revealed that the duration (Figure 4.5a), amplitude (Figure 4.5b), and frequency content of episodes (Figure 4.16) have the most dominant role in the clustering results. This suggests that these three factors are the main features that describe the general pattern of episodes in the seismic waveform.

Our method provides a fast and reproducible approach for automatic revealing of overall temporal evolution patterns of the volcanic systems. It can potentially be used in other eruptions studies and reveal the chronology of the system. This could be beneficial in revealing different phases of past activities and possibly discovering similar patterns. Volcano observatories aiming to analyze and interpret data in a timely manner may use this approach for the large-scale seismic datasets in a near-real time fashion. In a real-time observation framework, the reoccurrence of a previous cluster may inform about an upcoming similar phase that the system experienced before. The extracted salient feature of the seismic signal using the autoencoder may lead to revealing unanticipated information in an efficient way. This could help to better understand the volcanic processes. Also, it could potentially contribute to reveal precursory signals and contribute to volcanic hazard mitigation efforts.

4.6 Method

4.6.1 Feature extraction using autoencoder

Grouping seismic signals of volcanic activity with similar patterns could provide the potential for a deeper understanding of the volcanic processes. Clustering as a branch of unsupervised learning methods partitions unlabeled data into groups of similar objects. One of the fast and popular methods for clustering is k-means (MacQueen et al., 1967) which clusters data based on distance metrics. However, clustering high-dimensional data is computationally expensive and usually less effective as the dimension of data increases (Steinbach et al., 2004). Hence, dimensionality reduction and feature extraction are used before the clustering to improve the clustering results by performing the clustering in a feature space instead of the data space. The ability of deep neural networks to automatically learn cluster-friendly features has shown to be an effective method to improve clustering of high-dimension data (e.g. Xie et al., 2016 & Yang et al., 2017). Here we use an unsupervised deep learning technique named Deep Embedded Clustering (DEC) which uses the latent representation of data extracted using an autoencoder for the clustering task (Mousavi et al., 2019 & Xie et al., 2016).

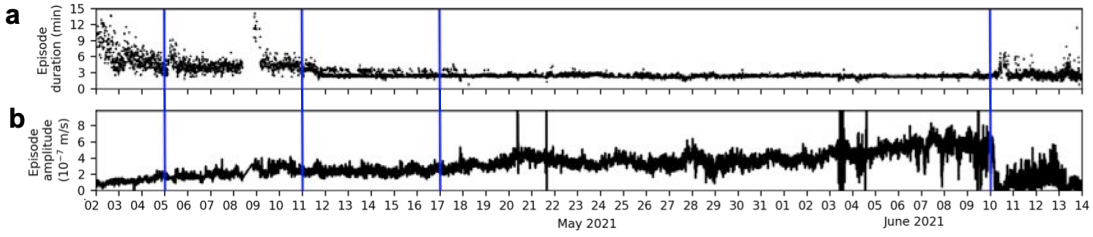

Figure 4.5. Duration and amplitude of the lava fountaining episodes. a, Duration of the lava fountaining episodes. b, Amplitudes of the lava fountaining episodes (modified from Eibl et al. 2023).

Autoencoders are neural networks that learn to compress their input data in the encoder part and decompress it in the decoder part (Vincent et al., 2010). The encoder learns to map the input to a latent representation through automatic feature extraction and a nonlinear transformation. The decoder reconstructs the input from the hidden representation by minimizing the reconstruction loss.

Our network consists of an autoencoder and a clustering layer, which is connected to the autoencoder's bottleneck (Figure 4.6). The encoder composed of four two-dimensional convolutional layers followed by a fully connected neural network, which after flattening of the extracted features by convolutional neural network layers, maps them to the latent space with

low dimension. The decoder has a fully connected neural network followed by four transposed convolutional layers. An Exponential Linear Unit (ELU) activation function is applied for the convolutional and fully connected layers. We use a linear activation function for the last layer in the decoder. The loss function of the autoencoder (L_R) is the mean squared error (MSE) between the input X and the reconstructed output X' as below:

$$L_R = \frac{1}{N}\sum_{i=1}^{N}(X - X')^2 \tag{4.1}$$

for N samples. Details about the hyperparameters of the model are presented in supplementary sheet 2.

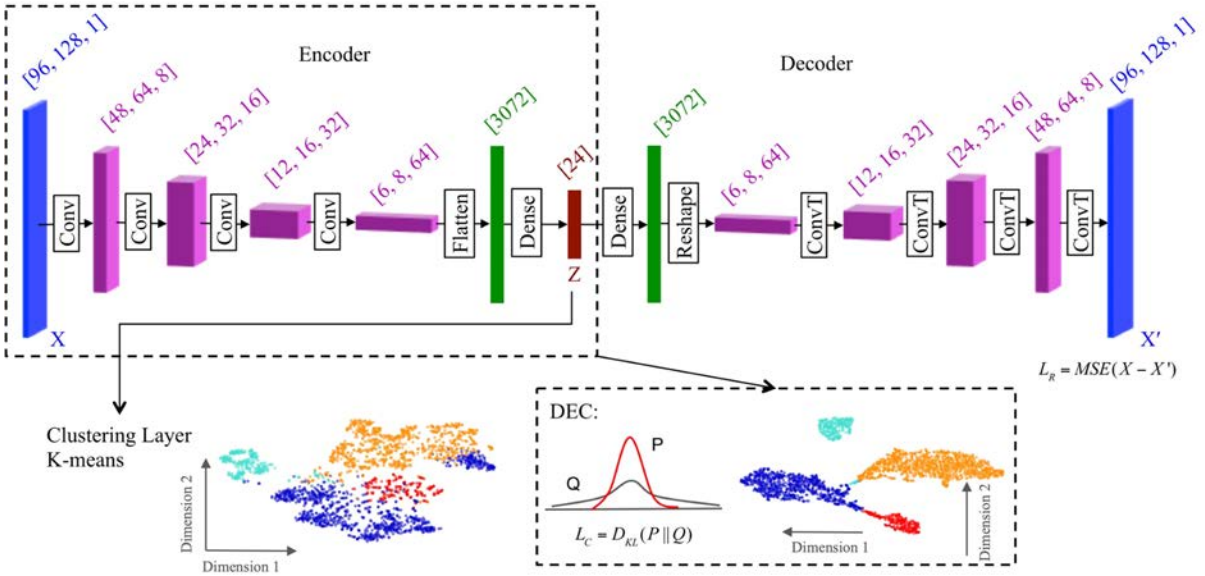

Figure 4.6. The encoder and decoder composed of convolutional fully connected layers. Reconstruction loss (L_R) and the clustering loss (L_C) as well as t-sne plots after pre-training and after fine-tuning of the continuous seismic waveform are given in the figure.

4.6.2 Deep embedded clustering

In a pre-training step the autoencoder is trained to reconstruct the output from the latent space close to the input. Then the extracted features from the bottleneck of the autoencoder are used for the clustering task using k-means algorithm. The algorithm separates the latent space into k clusters with k cluster centroid (μ_j). Next, during a fine-tuning step, the model simultaneously learns feature representations and assigns clusters to them. First the similarity between each embedded point z_i and cluster centroids μ_j is calculated using Student's t-distribution:

$$q_{ij} = \frac{(1 + |z_i||\mu_j|^2)^{-1}}{\sum_j (1 + |z_i||\mu_j|^2)^{-1}} \tag{4.2}$$

q_{ij} is the probability of assigning sample i to cluster j and results in a set of soft class assignments. An auxiliary target distribution p_{ij} is calculated using the membership probability q_{ij} as below:

$$p_{ij} = \frac{q_{ij}^2 / \sum_i q_{ij}}{\sum_j \left(q_{ij}^2 / \sum_i q_{ij} \right)} \tag{4.3}$$

During fine-tuning clustering layer minimizes the Kullback–Leibler (KL) divergence between the soft assignments, q_{ij}, and the target distribution, p_{ij}:

$$L = KL(P \parallel Q) = \sum_i \sum_j p_{ij} \, log \left(\frac{p_{ij}}{q_{ij}} \right) \tag{4.4}$$

Since q_{ij} is the membership probability of each embedded point in each cluster, it defines the confidence of cluster assignments. The auxiliary target distribution p_{ij} normalizes the loss contribution of each centroid by putting more emphasize on samples with higher confidence. So the network learns from high-confidence cluster assignments and refines the cluster centroids by minimizing the divergence between q_{ij} and p_{ij}. During iterations in fine-tuning the cluster centroids are refined, the autoencoder weights are updated, more clustering-friendly features are learned and the clustering results are improved. $L_C = \lambda L$ is the loss function of the clustering layer. λ is a hyper-parameter that weights the clustering layer. A too large λ will distort the latent space so the latent space will not represent the salient features of the data. A too small λ will eliminate the effect of clustering layer. We use 0.1 for λ as it is used in other studies as well (e.g. Mousavi et al., 2019; Snover et al., 2020, & Xie et al., 2016). For the optimization of the clustering layer we use stochastic gradient descent with a momentum of 0.9 and a learning rate of 0.01. Momentum is a moving average of the gradients and it is used to update the weight of the network. The autoencoder weights are updated every 200 iterations. Training will be stopped when the number of samples whose cluster assignments are changed, reaches less than 0.01% of the total number of the input data.

4.6.3 Clustering continuous seismic waveform

We use continuous seismic waveform from 12 March to 24 June 2021 aiming to identify the eruptive activity phases through clustering of volcanic tremors. Volcanic tremors recorded on the east component of station NUPH during the 2021 Geldingadalir eruption are dominant between 1 to 4 Hz so we use this frequency range for our study. Eibl et al., (2023) used this frequency range for the study of episodic tremors as well. The choice of an optimal frequency band depends on the signal of interest, but generally, frequency filtering reduces the dimension of input data and eases the extraction of features from the spectrogram using the autoencoder. Normally, for clustering of volcanic tremors one can use the frequency band of 1 to 9 Hz, which is the usual frequency range of these signals (McNutt & Nishimura, 2008). To further reduce the size of input data, the seismograms were resampled to 8 Hz after being demeaned and detrended.

Since volcanic tremors have a more distinct representation in the time-frequency domain compared to time domain, we calculate the Short Time Fourier Transform (STFT) of one-hour windows of the continuous seismic signal and use the obtained spectrograms as the input for our neural network. To choose the window length, we opt to use the shortest duration that could cover the longest changing pattern. The selected one-hour seismograms are long enough to cover most of signal variations in the volcanic environments. Hence, to generalize the algorithm, we use one-hour windows of the amplitude spectrogram as the input to the autoencoder. As shown in the Figure 4.6, the input and output are 96 (frequency bins) by 128 (time bins) and the bottleneck has a flat dimension of 24. The architecture of our autoencoder

is presented in the Table 4.1.

As shown in Figure 4.7a, training and validation losses exponentially decrease during autoencoder training. The ability of the autoencoder to reconstruct the input from the latent spectrogram is illustrated in the Figure 4.2. The structure of the spectrogram is mainly preserved after reconstruction of the input from the encoded salient features of the latent space. This is a good indication that during the pre-training stage, the network has learned to extract a good selection of features representing the essential elements of our signal of interest. The k-means clustering is then applied to the extracted features at the bottleneck of the autoencoder.

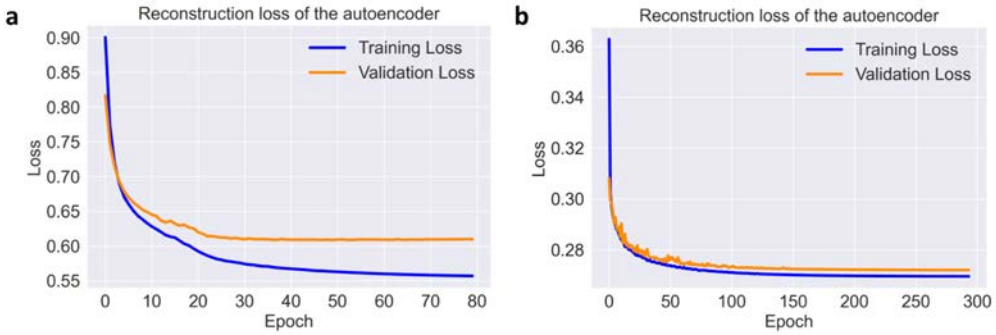

Figure 4.7. Training and validation loss of the autoencoder. Training and validation losses during autoencoder training for the continuous seismic waveform (a) and for the episodic tremors (b) are presented.

To choose the optimal number of clusters we varied the number of clusters, k, between 2 and 15 and calculated the Calinski-Harabasz (Caliński & Harabasz, 1974) index, also known as the variance ratio criterion, which is the ratio of the sum of between-clusters dispersion and of inter-cluster dispersion (Figure 4.8a). We choose the number of clusters to be 4 as it based on the elbow point at the Calinski-Harabasz index plot. This is the cutoff point where diminishing the index by increasing the number of cluster suddenly decreases. Figure 4.9a presents the initial result of k-means clustering of the latent space with the selected number of clusters 4. We visualize the data with 24 dimensions in two dimensions using t-sne method (Maaten & Hinton 2008). Next, after fine-tuning the four clusters are well separated in the t-sne plot (Figure 4.9b). The well separation of clusters in the t-sne space indicates the effectiveness of the DEC algorithm in extracting the most useful features for our clustering task.

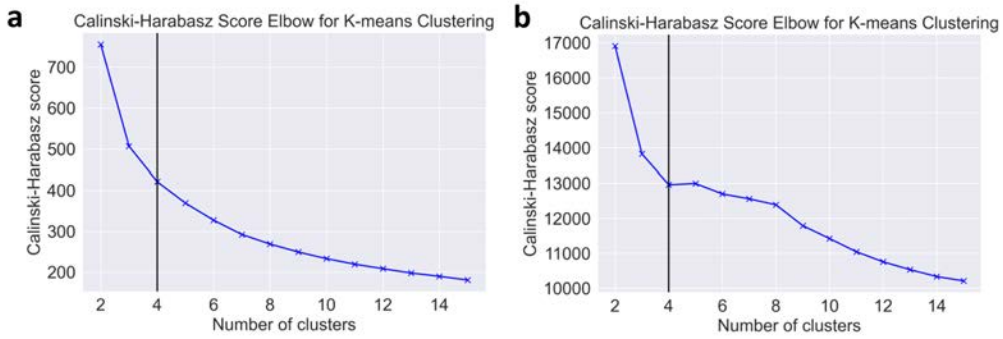

Figure 4.8. Choosing the optimal number of clusters. The number of cluster k=4 is chosen for both the continuous seismic waveform (a) and for the episodic tremors (b) by calculating the Calinski-Harabasz score.

More than 99% of the samples belong to their determined cluster with high confidence; likelihood more than 0.99. Details about samples with likelihood below 0.99 are discussed in supplementary sheet 3.

It is worth to mention that the clustering is done based on the salient features of the seismic signal. If there are different patterns in a time window, the salient pattern determines the related cluster for that time window. For example, there are small earthquakes in our study time that occur in time windows that do not belong to the EQ cluster. The reason is that in those time windows in addition to the earthquake signal there is another pattern (like continuous tremor) that is more dominant compared to the earthquake signal. This means that another process represents the system phase in those time windows.

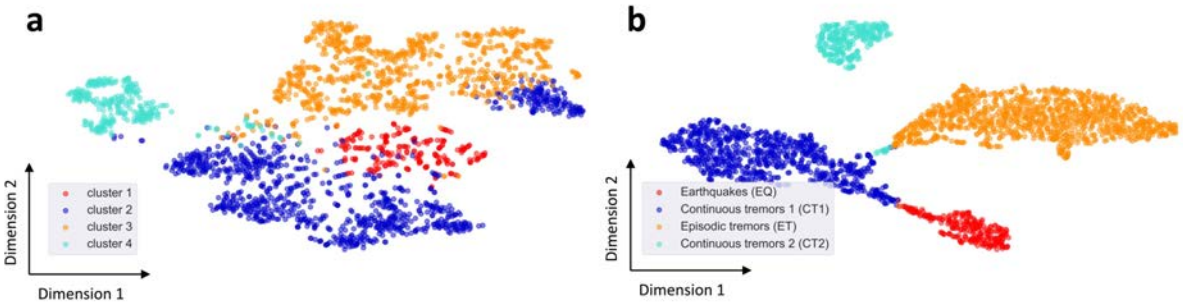

Figure 4.9. T-sne visualizations of the salient features of the continuous seismic waveform. a, T-sne visualizations of data in feature space after pre-training and clustering using k-means algorithm with 4 clusters. b, T-sne visualizations of data in feature space after fine-tuning.

4.6.4 Clustering episodic tremors

Episodic tremors during the 2021 Geldingadalir eruption that are the dominant pattern in the seismic signal from 2 May to 14 June, have different durations, repose times, and amplitudes and could indicate different periods of the volcanic processes. The duration of lava fountaining episodes vary between 2 to 14 min with an average of 3 min (see Figure 4.4f). For a detailed investigation on the lava fountaining episodes we apply a DEC for the episodes. We used the onset time of the episodes from Eibl et al., (2022a) and cut the seismic waveform 7 minutes after the onset time of each episode. 7 minutes is a suitable length for our dataset considering the average duration of the episodes and also because more than 90% of the episodes have duration less than 7 minutes.

We consider the frequency range of 1 to 4 Hz and calculate the STFT of the episodes for the input of the autoencoder. The autoencoder architecture is the same as we designed before. This indicates that our autoencoder does not depend on the input size and can extract features from both one-hour and 7-min spectrograms and reconstruct the input in the decoder. Here the input and output are 1536 dimensional matrices (32 frequency bins and 48 time bins) and the bottleneck has a dimension of 3 (Table 4.1). The number of input spectrograms for training and validation are listed in Table 4.2. For training the autoencoder here we used the Mean Absolute Error (MAE) loss function with a decay rate of 0.9. MAE, which is more robust to outliers and calculates the average of the absolute difference between the input and the reconstructed output.

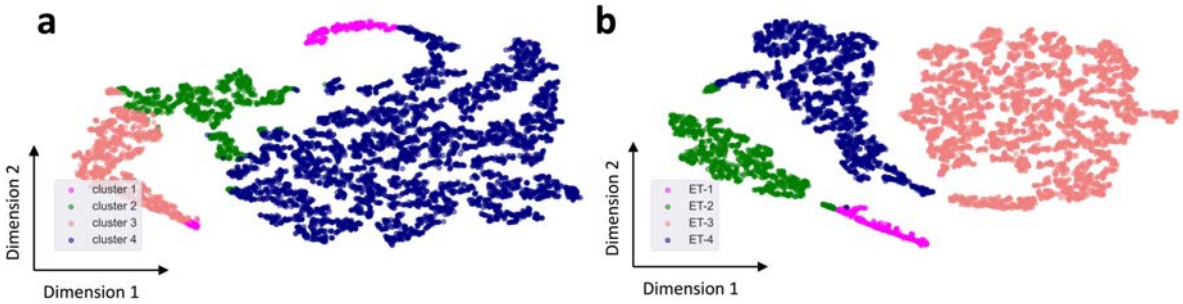

Figure 4.10. T-sne visualizations of the salient features of the episodic tremors. a, T-sne visualizations of data in feature space after pre-training and clustering using k-means algorithm with 4 clusters. b, T-sne visualizations of data in feature space after fine-tuning.

Training and validation losses are shown in the Figure 4.7b. Some examples of the input and output of the autoencoder are shown in Figure 4.16. We apply k-means clustering on the bottleneck of the autoencoder. We choose k=4 as the optimal number of clusters based on the Calinski-Harabasz score (Figure 4.8b). The t-sne plot before and after fine-tuning is shown in the Figure 4.10.

Table 4.1. Autoencoder Architecture. The architecture is the same for the continuous seismic waveform and the episodic tremors but the size of the input data are different. Black values are related to the continuous seismic waveform and grey values are related to the episodic tremors.

Autoencoder Architecture								
Layer Name	Type	Input Shape	Filters	Kernel Size	Stride	Activation	Output Shape	Trainable Parameters
Input	_	_	_	_	_	_	[96, 128, 1] [32, 48, 1]	_
Conv1	Convolution	[96, 128, 1] [32, 48, 1]	8	[7, 5]	[2, 2]	ELU	[48, 64, 8] [16, 24, 8]	288 288
Conv2	Convolution	[48, 64, 8] [16, 24, 8]	16	[5, 3]	[2, 2]	ELU	[24, 32, 16] [8, 12, 16]	1936 1936
Conv3	Convolution	[24, 32, 16] [8, 12, 16]	32	[5, 3]	[2, 2]	ELU	[12, 16, 32] [4, 6, 32]	7712 7712
Conv4	Convolution	[12, 16, 32] [4, 6, 32]	64	[5, 3]	[2, 2]	ELU	[6, 8, 64] [2, 3, 64]	30784 30784
Flat	Flatten	[6, 8, 64] [2, 3, 64]	_	_	_	_	[3072] [384]	0 0
Encoded	Fully Connected	[3072] [384]	_	_	_	ELU	[24] [3]	73752 1155
FC	Fully Connected	[24] [3]	_	_	_	ELU	[3072] [384]	76800 1536
Reshape	Reshape	[3072] [384]	_	_	_	_	[6, 8, 64] [2, 3, 64]	0 0
ConvT1	Transposed Conv	[6, 8, 64] [2, 3, 64]	32	[5, 3]	[2, 2]	ELU	[12, 16, 32] [4, 6, 32]	30752 30752
ConvT2	Transposed Conv	[12, 16, 32] [4, 6, 32]	16	[5, 3]	[2, 2]	ELU	[24, 32, 16] [8, 12, 16]	7696 7696
ConvT3	Transposed Conv	[24, 32, 16] [8, 12, 16]	8	[5, 3]	[2, 2]	ELU	[48, 64, 8] [16, 24, 8]	1928 1928
Decoded	Transposed Conv	[48, 64, 8] [16, 24, 8]	1	[7, 5]	[2, 2]	ELU	[96, 128, 1] [32, 48, 1]	281 281
							Total	231,929 84,068

Data availability

Seismic data from station NUPH are available via GEOFON (Eibl et al. 2022b). The list of tremor episode start and end times is available at GFZ Data Services (Eibl et al. 2022a).

Code availability

The Python code “ClusTremor” related to the proposed method is freely available from https://github.com/ZahraZali/ClusTremor (Zali, 2023).

4.7 Appendix

4.7.1 Supplementary Information Sheet IS1: Harmonic-percussive separation

In the result of clustering continuous seismic waveform we observe some samples in the cluster CT1 between 16 and 19 March. As we explained, cluster CT1 represent continuous tremors.

Observing samples before the start of the eruption raised a hypothesis of existence of precursory tremors 3 days before the eruption. We look at the seismogram and spectrogram of the seismic signal a few days before the eruption (Figure 4.3a) but due to the intense seismic activity before the eruption it is difficult to detect the precursory tremor. Hence, we used the harmonic-percussive separation algorithm from Zali et al., (2021) to extract the potential precursory tremor signal.
As the extracted tremor spectrogram (Figure 4.3b & c) shows, a clear tremor starts on 16 March. This is well in line with our result of deep embedded clustering. Harmonic-percussive separation algorithm is an algorithm for separating simultaneous transient events from long-lasting signals. It has different applications in seismology such as volcanic tremor extraction (Zali et al., 2021; the related code is available at Zali, 2022a) and noise reduction (Zali et al., 2023; the related code is available at Zali, 2022b). The tremor extraction method consists of a two-step separation. In the first step, using a similarity matrix, which measures the cosine similarity between the STFT time frames, repeating patterns in the spectrogram are identified. A median filter is applied to the identified similar frames to constitute the repeating spectrogram that corresponds to harmonic components. To remove the remnants of the transient signals from the repeating spectrogram, in a second step, a horizontal median filter is applied along the time axis. This results in a spectrogram consisting of harmonic patterns of the signal with significantly less energy of the transient signals.

4.7.2 Supplementary Information Sheet IS2: Details of the model hyperparameters

For model training, the trainable parameters are optimized using the Adaptive Moment Estimation (Adam) algorithm (Kingma & Ba, 2017), which propagates the loss backwards through the model after every batch iteration. Batch size defines the number of input for the model at one time. We adapt the learning rate of the optimizer using an exponential decay schedule to increase model performance and reduce training time. The initial learning rate of 0.001 decays every 1000 step with a base of 0.5 across different invocations of optimizer function. Very small learning rate makes the training slow or causes the model settle into a local minimum. Too large learning rate will cause the model converge slowly or not converge at all. From all the input, 80% were used for the training and 20% for the validation. To prevent the autoencoder from over-fitting, training is stopped early if the validation loss has not decreased in 30 epochs. Batch size and learning rate are hyper-parameters of the model and are sets through hyper-parameter tuning. During this process the autoencoder is trained with different hyper-parameter values and the value, which results in the best model, will be chosen. Number of input spectrograms for training and validation as well as the optimal hyper-parameters are listed in Table 4.2.

Table 4.2 | Input sizes and hyper-parameters of deep embedded clustering model

Samples			
Parameters	al input size	Training size	Validation size
Continuous seismic waveform	2390	1912	478
Episodic tremors	7041	5632	1409

Autoencoder hyperparameters **Clustering hyperparameters**

Parameters	Initial learning rate	Decay step	Decay rate	Batch size	Factor (λ)	Optimizer momentum	Learning rate
Continuous seismic waveform	0.001	1000	0.5	32	0.1	0.9	0.01
Episodic tremors	0.001	1000	0.9	32	0.1	0.9	0.01

4.7.3 Supplementary Information Sheet IS3: likelihood of each sample of the continuous seismic waveform to belong to their determined clusters

To investigate the confidence of data belongingness to their cluster we calculated the likelihood of each sample to belong to each of the four clusters. The likelihood is calculated using the mean of each cluster and the covariance matrix. Figure 4.11 shows that majority of the data belong to their specified cluster with high confidence. Existence of some samples in cluster EQ after 19 March and some samples in cluster CT1 before 19 March are discussed in the manuscript (see Figure 4.2) and they are samples with high confidence. In total from 2390 samples (one-hour spectrograms) there are 21 samples with likelihood below 0.99. Figure 4.12 shows all these samples and their specified clusters. In cluster EQ, out of 5 low confidence samples, two of them with likelihood below 0.8 are clustered in a false cluster. Sample 241 from 22 March should belong to cluster CT1, but here the continuous tremor signal is masked by the energy of a transient signal, which is not an earthquake. Sample 971 from 26 April and sample 1032 from 29 April with low confidences in cluster ET are related to the time that the system is changing from continuous tremor to episodic tremor. None of these patterns are clearly exhibited in these samples so they have low likelihood. All other low confidence samples are related to after 10 June when the system is in a transition phase between the episodic tremors and continuous tremors. The samples contain both of these patterns so the likelihoods to belong to one cluster are lower than other samples with a dominant pattern.

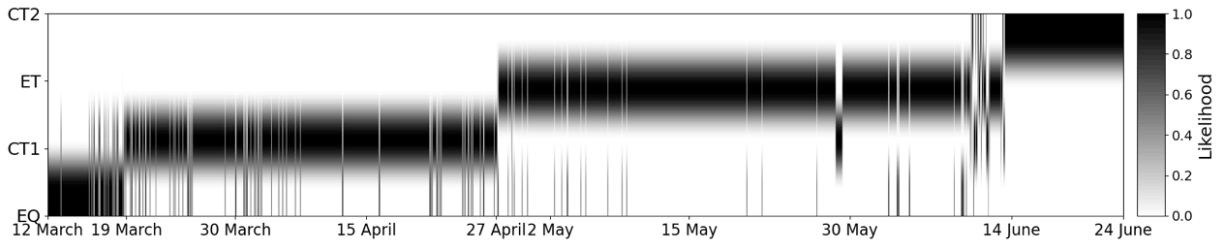

Figure 4.11. Likelihood of each sample of the continuous seismic waveform to belong to each of the four clusters.

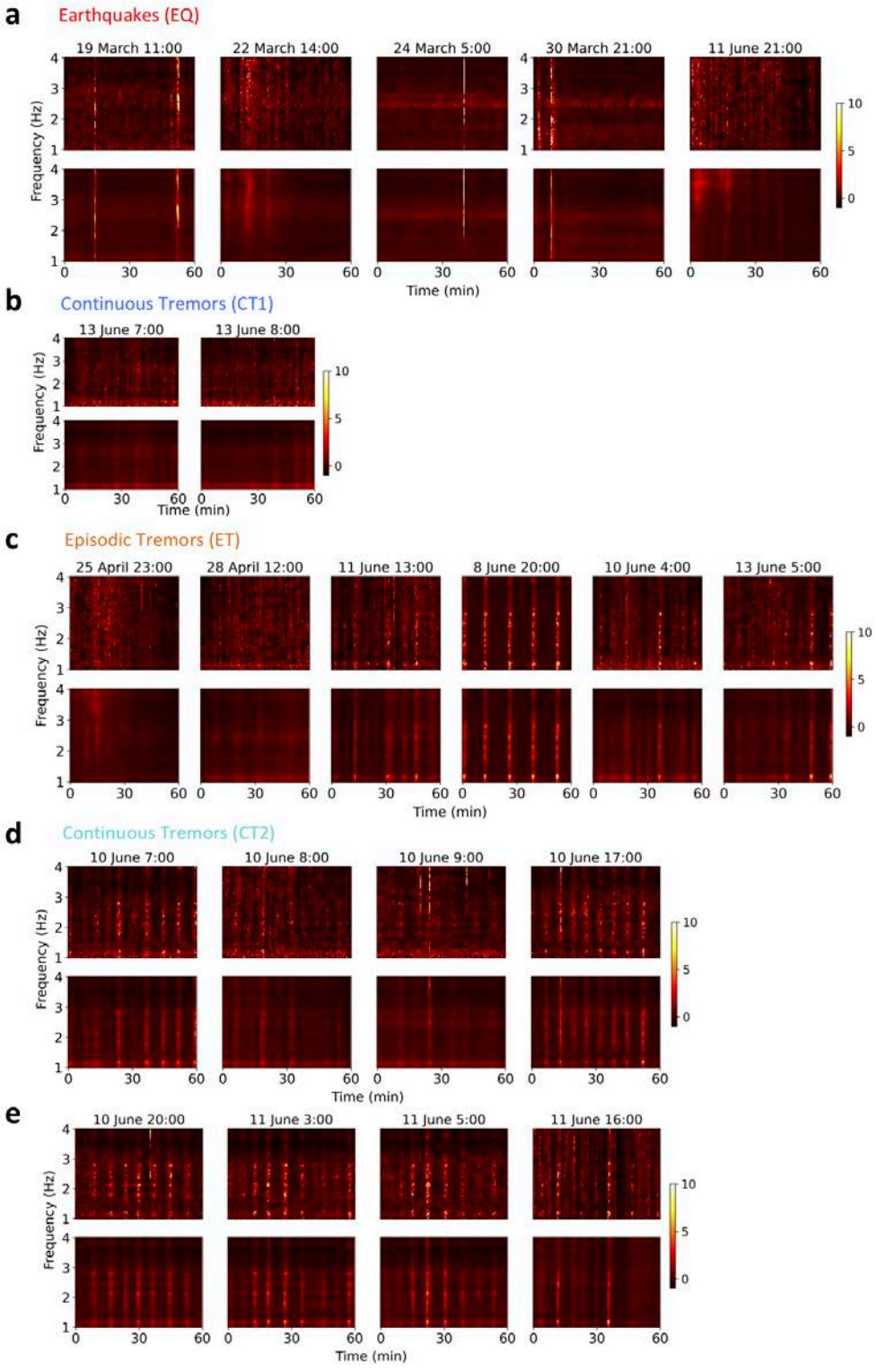

Figure 4.12. Samples with likelihood below 0.99 and their specified clusters. a, Samples in the cluster EQ with likelihood below 0.99. b, Same as a for the cluster CT1. c, Same as a for the cluster ET. d & c, Same as a for the cluster CT2. In each subfigure the top row is the input of the autoencoder and the bottom row is the output of the autoencoder.

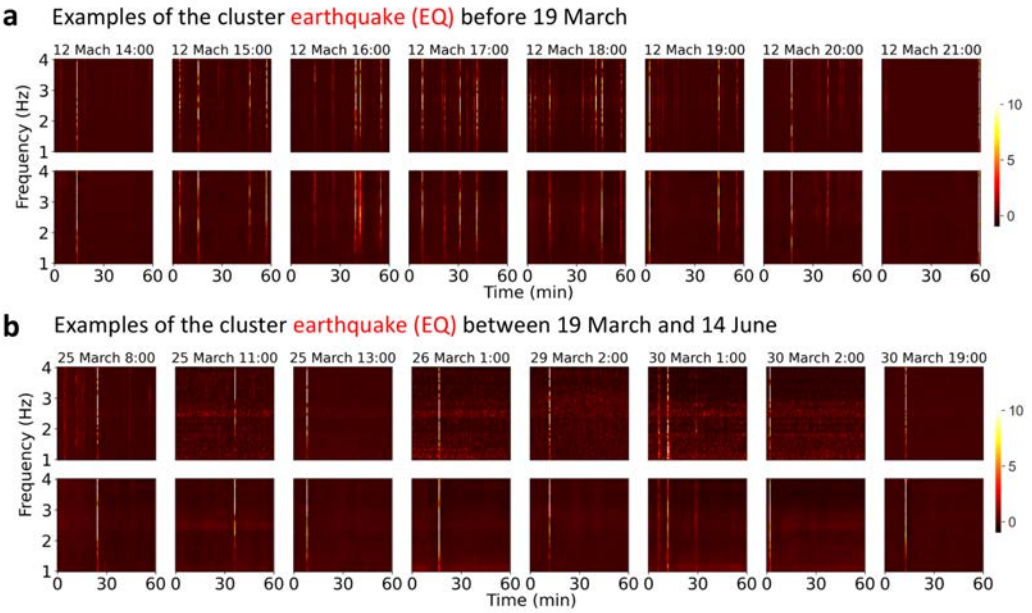

Figure 4.13. Examples of inputs and outputs of data in the cluster EQ which represent earthquake sections. a, Samples before start of the eruption. b, Samples between the start of the eruption and 14 June. In each subfigure the top row is the input of the autoencoder and the bottom row is the output of the autoencoder.

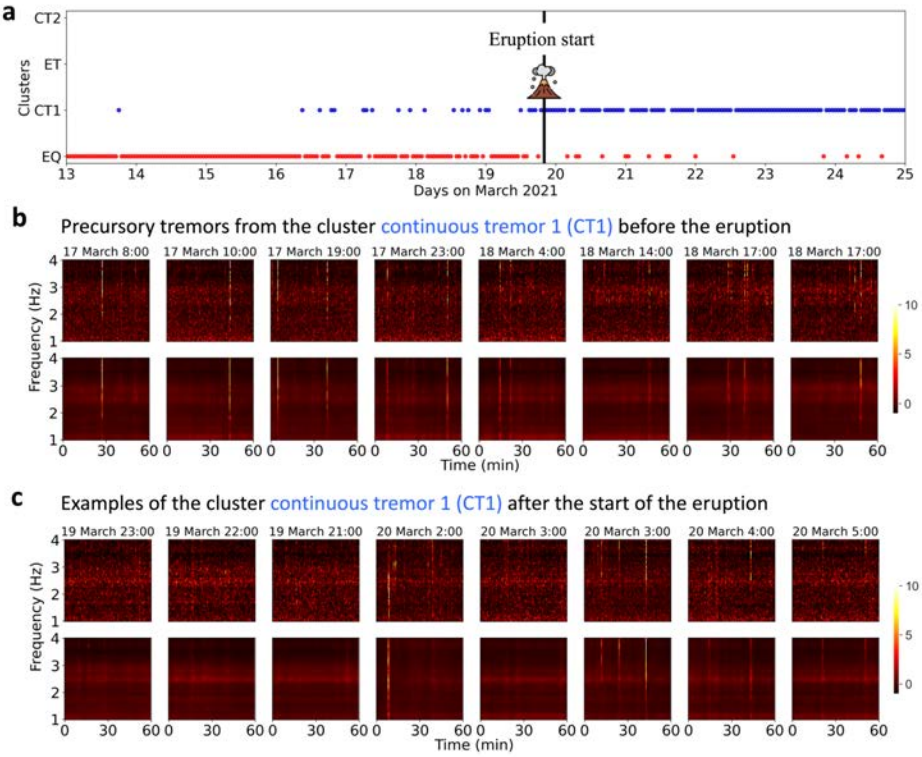

Figure 4.14. Observing precursory volcanic tremor from 16 March onward (three days before the start of the eruption). a, Deep embedded clustering results related to 13 to 25 March. b, Examples of inputs and outputs of data in the cluster CT1 (continuous tremor 1) between 16 to 19 March. c, Examples of inputs and outputs of data in the cluster CT1 after the start of the eruption. In b and c the top row is the input of the autoencoder and the bottom row is the output of the autoencoder.

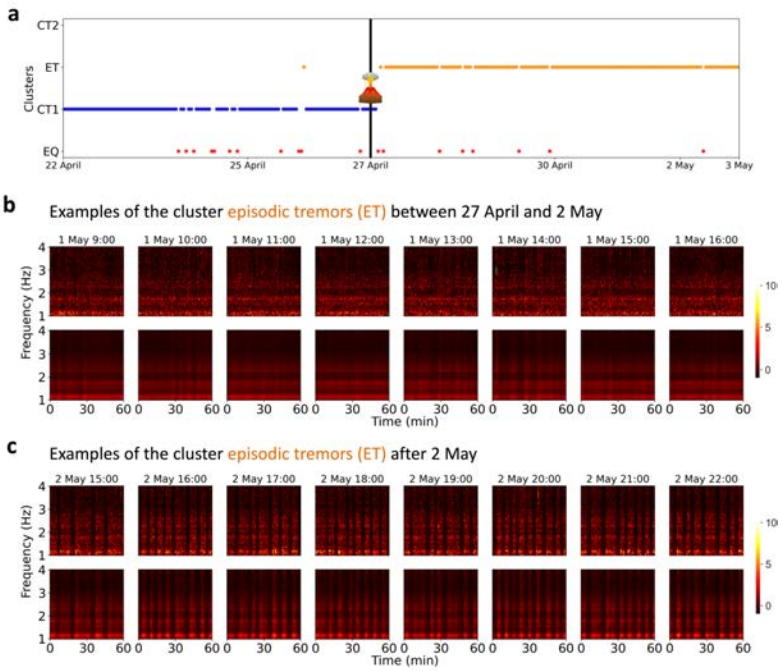

Figure 4.15. Samples from the cluster ET (episodic tremors). a, Examples of inputs and outputs of data in the cluster ET between 27 March and 2 May. b, Examples of inputs and outputs of data in the cluster ET after 2 May (start date of lava fountaining). In each subfigure the top row is the input of the autoencoder and the bottom row is the output of the autoencoder.

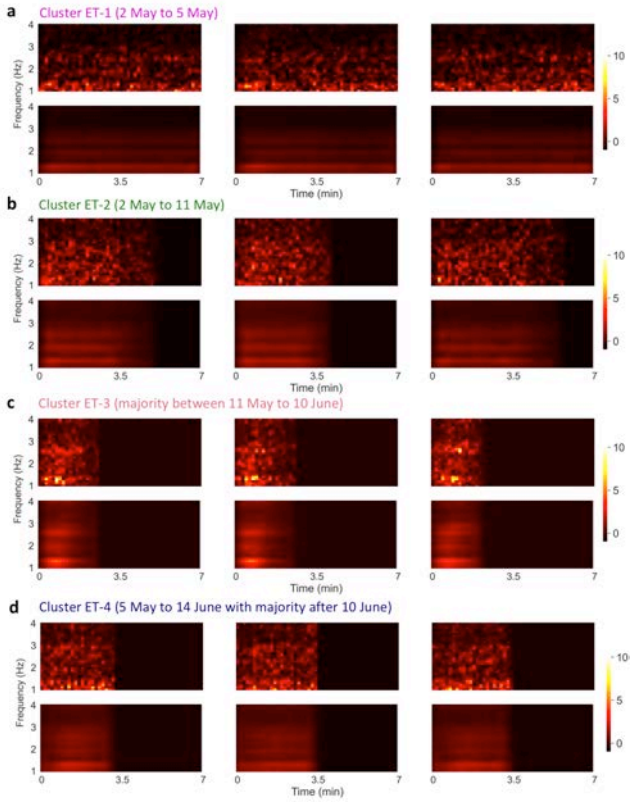

Figure 4.16. Examples of samples in each cluster of the lava fountaining episodes. a, Examples of samples in cluster ET-1. b, Same as a for cluster ET-2. c, Same as a for cluster ET-3. d, Same as a for cluster ET-4. In each subfigure the top row is the input of the autoencoder and the bottom row is the output of the autoencoder.

Chapter 5

Main results and discussion

5.1. Tremor extraction provides a clean volcanic tremor signal that improves the analysis of associated volcanic processes.

We extract volcanic tremors from the seismic record to facilitate the analysis related to this signal and corresponding volcanic activities. The amplitude, shape, and phase of the extracted tremor signal correlate well with the original record. We created semisynthetic data (a combination of real earthquakes, synthetic tremor signal, and seismic noise) with different SNRs of the harmonic signal and investigate the extraction methodology through semisynthetic tests. We measure the cross-correlation of the synthetic harmonic signal and the extracted harmonic signal. We show that we can reconstruct the tremor signal for an SNR of at least 0.4 with a cross-correlation of more than 0.8. The differences between the extracted tremor and the synthetic tremor signals are mainly related to small fluctuations in the input harmonic signal, which show a random pattern instead of a repetitive pattern. We also use real data to evaluate the ability of tremor extraction. The reconstructed tremor signal matches well with the original seismic records and has no trace of transient, earthquake-related signals.

5.2. Earthquake detection along with tremor extraction contributes to a better understanding of the interaction between volcanic tremors and earthquakes.

Besides extracting the volcanic tremor signal, we create a characteristic function related to transient signals and use it for detecting earthquakes. The detection rate is evaluated using semisynthetic and real tests. The results show that for SNR = 0.1, we can detect more than 78% of the events. The average percentage of false picks is 6% for SNR between 0.3 and 1, however, below SNR = 0.3, there are more (up to 30% of all events) false picks. For SNR higher than 0.1, 42% of the missed events are long period (LP) events. The challenge of detecting LP events is related to the properties of the characteristic function, which is used for the detection. This function is more sensitive to broadband signals since it is derived from summing, for each time frame, all frequencies in the transient spectrogram. LP events are more narrowband compared to volcano-tectonic events and detecting them is more difficult. Also, LPs usually persist longer and this is another reason that makes their detection difficult. To create the repeating spectrogram, we derive the corresponding frame in the repeating spectrogram by taking the median of the similar frames for each frequency bin. For a transient (short duration in time) event, there could be a few numbers of similar frames in the spectrogram, so it is identified as a nonrepeating pattern. Therefore, the transient event will show a short-lasting sharp peak in the transient characteristic function. For a long-lasting event, there are some adjacent similar frames, which will be replaced in the repeating spectrogram by the median of them. So, the long-lasting event shows some long-lasting and less sharp adjacent peaks in the transient characteristic function, which is less likely to be detected by the local maximum finder compared with sharper peaks.

We also test the earthquake detection rate of our algorithm with real data and compare the results with other studies. We use a single vertical component to detect earthquakes in September 2014 during the 2014-2015 Holuhraun eruption. We compare the number of detected earthquakes with the bulletin published by Ágústsdóttir et al. (2019) who used a dense local seismic network comprising 72 three-component broadband instruments. We detect a total

of 12,619 events, which is more than twice the number of listed events in their bulletin. We also show that our method can detect two adjacent earthquakes with a minimum interval of around 10s. The shortest interval value to detect two adjacent earthquakes depends on the number of FFT points, the hop size, and the type of earthquake. In our dataset, earthquakes are mostly local, and shorter interval time values will result in the detection of more than one peak for one event.

5.3. Noise reduction of seismic recordings, especially without earthquake distortion, helps to improve the image of the subsurface.

We develop an algorithm to reduce noise from the seismic records and especially from Ocean Bottom Seismometer (OBS) data. We reduce noise from both the vertical and horizontal components, which was a big challenge before this study. We preserve the earthquake signal with the true amplitude and phase after denoising. This makes our algorithm useful for different analyses. To effectively remove noise and preserve the teleseismic signal we divide the frequency band of the spectrogram into two frequency ranges and for each range we use one HPS algorithm. By this division, we separate the frequency range of 0.1 to 1 Hz from other frequencies. Thus frequency division and the use of different algorithms for each range have two purposes: 1- Preserving the energy of low-frequency content (below 0.1 Hz) of the teleseismic events signals and 2- Preserving the true amplitude and phase of the P and S arrivals (between 0.1 to 1 Hz) which usually interfere with the oceanic microseism noise (dominant frequency around 0.1 to 0.3 Hz).

We evaluate the algorithm using synthetic and real tests. The SNR for noisy and denoised signal show significant improvement on all three components after denoising. The high correlation coefficients for the denoised signal and the synthetic earthquake signal compared with the noisy signal and the synthetic earthquake signal for different noise configurations demonstrate a significant noise reduction. A comparison of the root mean square (rms) of the synthetic earthquake, noisy and denoised signals shows that the synthetic earthquake and denoised signals have similar amplitude ranges, while the noisy signal has much higher amplitude. This proves a significant noise reduction along with the preservation of the earthquake and phase arrivals energy. The algorithm removes noises with narrowband frequencies better than broadband noises. The SNR improvement is lower for signals with significant noise frequency variations over time than for signals with a relatively stable noise frequency.

The value of our denoising techniques in seismological analyses, especially those involving the analysis of teleseismic body and surface waves is discussed through various applications of the algorithm. Analysis of the SH wave field (e.g. Love waves) can reveal key information about the Earth's structure in oceanic regions. However, such analysis is often complicated due to strong noise on the horizontal components. SV waves, which are, for instance, important for tomography studies or S and SKS shear wave splitting analysis are also often masked by noise. Our synthetic tests show that the SH phase which was hardly detectable on the horizontal component becomes clearly identifiable after denoising.

We measure, through synthetic tests, Love and Rayleigh waves group velocities with the Multiple Filter Technique (MFT) (Dziewonski et al., 1969) to test the performance of our algorithm in the low-frequency range. Dispersion curves are greatly enhanced in the figures resulting from denoised traces. The Love and Rayleigh waves time histories improve significantly as well. These results show how noise energy is successfully removed in the frequency range of 0.05 to 0.2 Hz (the teleseismic event frequency range in our test). We also

evaluate our denoising technique using real surface wave data through MFT analysis and group velocity dispersion curves. For all components, we find that the improved SNR of denoised data allows the analysis of more events and in a broader frequency range.

Receiver functions are a valuable tool to reveal the Earth's structure using teleseismic events records (e.g., Langston, 1979; Ammon et al., 1990; Kind et al., 1995; Rondenay, 2009). We compare the receiver functions calculated from the synthetic and real data before and after denoising. For both synthetic and real receiver functions, the noise level strongly decreases, and we observe a significant decrease in variance on denoised traces compared to noisy traces. These results demonstrate that the determination of the crustal and mantle phases is easier on the denoised receiver functions stack compared to the noisy receiver functions stack. More distinct Ps-phase arrivals are observed on the denoised stack compared to the noisy stack. In synthetic tests, P-to-S conversion at the Moho and its multiple (PMsPp) is better resolved in the denoised synthetic. Instead of a rather weak peak on the real data stack, a strong peak at the expected time arrival for the P410s phase (Ps conversion at the 410 km discontinuity) is observed on the denoised stack. This confirms the sharp velocity contrast at the 410 km discontinuity. The amplitudes of the P660s phase (Ps conversion at the 660 km discontinuity) on the denoised stack decreased and became a broader peak compared to the noisy stack of real data. This is consistent with the expectations from a conversion at a gradual velocity contrast. These results are in line with Hannemann et al. (2017) analysis of the crustal and mantle structure in this area.

5.4. Advanced machine learning techniques could reveal precursory volcanic tremors and the evolution of eruptions.

In the last step of my PhD, we extend the analysis of volcanic processes using advanced machine learning tools. Our results demonstrate that machine learning techniques can discover subtle hidden information in the seismic signal, reveal changes in the volcanic system and detect patterns such as a precursory volcanic tremor before the Geldingadalir 2021 eruption. Unsupervised processing of seismic records using deep neural networks and clustering reveal the temporal evolution of the eruptive activity in an automated and efficient manner. In this study, we use a deep neural network and extract the salient features of the volcanic tremors from continuous seismic waveforms and use them to identify different clusters and the temporal patterns related to different eruptive phases. Our algorithm, named as Deep Embedded Clustering (DEC), simultaneously learns feature representation and clustering. We find out that salient features of the seismic signal extracted by the autoencoder can describe the system stages.

The Geldingadalir eruption, which started on March 19, 2021, features different volcanic processes such as pre-eruptive activities, continuous lava extrusion, and episodic lava fountaining. We compute the Short Time Fourier Transform (STFT) of one-hour windows of the continuous seismic data. The salient features of the spectrograms are automatically extracted by the autoencoder and are used for clustering. We observe four clusters and four patterns ranging from intense earthquake sequences, episodic tremors, and different continuous tremors, each associated with major phases of volcanic activities. Dates of cluster changes inform about major changes in the system. A cluster change from intense seismic activity in the pre-eruptive phase to continuous tremors related to magma movement and outflow happens on 16 March; three days before the eruption. Although the 2021 Geldingadalir eruption initially has been reported to erupt without any precursory tremor, our clustering result suggests that the tremor related to magma activity starts before the eruption. We checked the seismic signal and

spectrogram but similarly as previous studies we couldn't directly observe the tremor on the raw data due to the high energy of the earthquake related signals. After we applied our tremor extraction algorithm (developed in the first study of this PhD thesis (Zali et al., 2021)), we clearly observe a tremor that starts three days before the eruption. This result confirms the occurrence of precursory tremors as revealed by our DEC model. This is an important finding because volcanic tremors are well-established precursors to volcanic eruptions that could alert about an upcoming event. No reported precursory tremors in other studies could be due to the intense seismic activities in the pre-eruption period that overlay the weaker energies of the tremors. As such, our results show that the lack of precursory tremors observation in some eruptions could be due to the precision of the data processing rather than an unknown mechanism that generates these signals in some eruptions and doesn't generate them in some other eruptions.

The change from a cluster of continuous tremors to a cluster of episodic tremors on April 27 could provide an explanation for the transition mechanism from vigorous outflow to lava fountaining. Indeed, after April 27 the eruption style changed with an increased effusion rate (Halldórsson et al., 2022; Pedersen et al., 2022). From May 2 until June 14, the eruptive activity is characterized by a sequence of lava fountaining (Eibl et al., 2023; Lamb et al., 2022; Pedersen et al., 2022) reflected as episodic tremors on seismic data. A clear pattern of episodic tremors is seen on the seismic signal by the start of the lava fountaining on 2 May. The results of our model indicate that episodic tremors started earlier on April 27. This is confirmed by a visual examination of the spectrograms that indicates the presence of a subtle episodic pattern starting on April 27. Such result illustrates the high sensitivity of our processing approach. Based on these results we suggest that the lava fountaining is triggered on April 27 by an increase in the magma flow rate. This cluster ends on June 13 when the lava fountaining ends and another cluster starts with a dominating continuous tremor pattern.

Episodic tremors in this eruption show distinct patterns with different duration, repose time, and amplitude. For a more detailed analysis of these episodic tremors, we performed another DEC of tremor episodes between May 2 and June 13. This time the input are STFT of 7-minute fountaining episodes. Our model does not depend on the input size and can extract features from both one-hour and 7-min spectrograms and reconstruct the input in the decoder. Clustering episodic tremors results in four clusters and introduces four dates for the changes. Clusters time changes are in line with the detailed study of episodic tremors by Eibl et al., (2023) who linked the evolution of episodic tremor patterns to an evolving shallow magma compartment, outgassed lava accumulating in the crater edifice and a widening conduit.

The autoencoder extracts three features from the STFTs of episodes and DEC is performed using these three features. Visual inspection of the raw data associated to the clusters episodes revealed that the duration, amplitude, and frequency content of episodes have the most dominant role in the clustering results. This suggests that these three factors are the main features that describe the general pattern of episodes in the seismic waveform.

I summarized my PhD work in the Figure 5.1. This Figure summarizes the main purposes and challenges of our study. The Figure also presents the algorithms, which I have developed and shows the contribution of these methods to improve the understanding of our planet, the Earth.

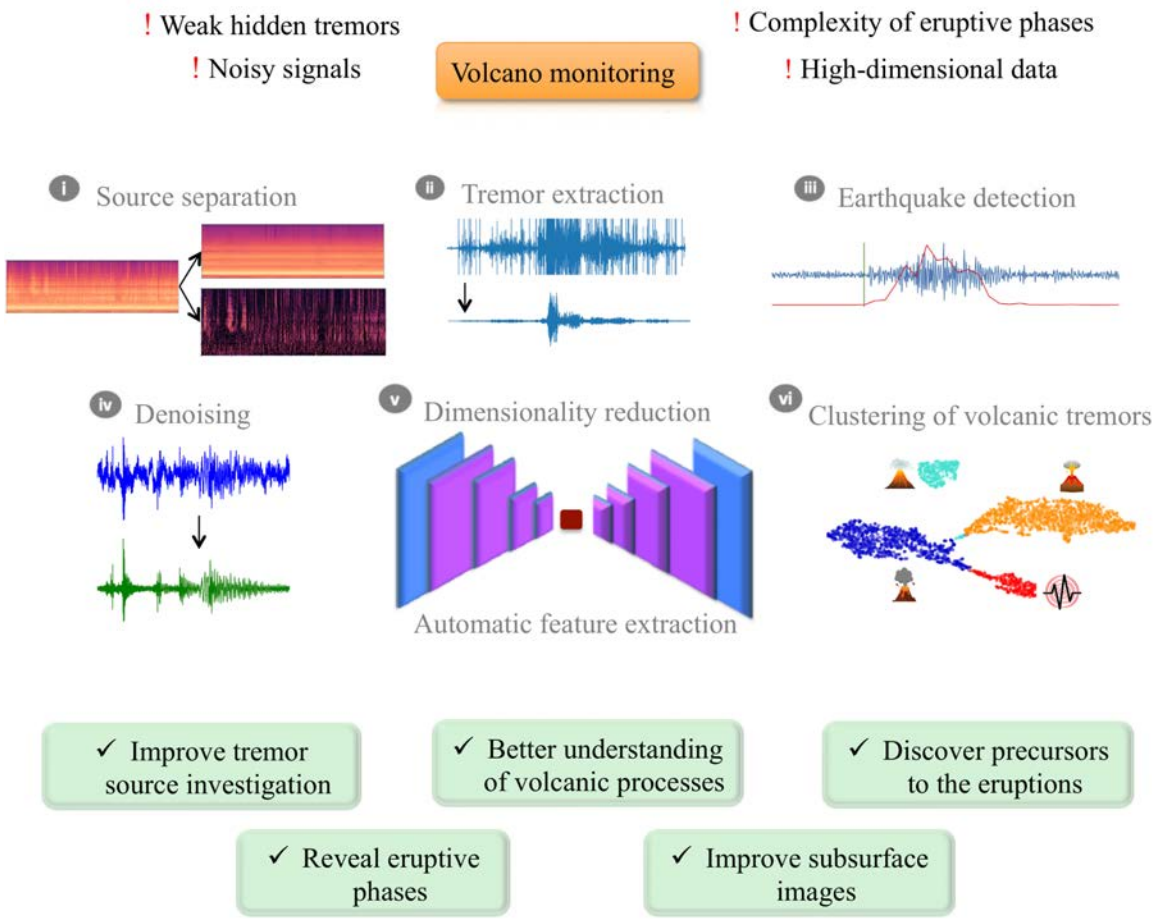

Figure 5.1. The Figure illustrates the general outline of this PhD thesis. The main purpose of this study (volcano monitoring using seismological records) poses different challenges such as weak hidden tremors detection, noisy signals analysis, high-dimensional data processing, and the difficulty of eruptive phases detections. I developed various algorithms shown in (iv) to (vi) to improve the analyses of such complex signals. The contributions of these algorithms to improve the understanding of Earth processes are shown in the bottom green boxes.

Chapter 6

Conclusions and outlooks

I have developed a method to extract volcanic tremor signals, as well as to detect transient signals from seismic waveforms. This method can extract harmonic tremor signals and is applicable to other volcanoes that exhibit such phenomena. A possible application of the proposed method is to extract volcanic tremor signals using a network or an array during a period of heightened volcanic activity. In particular, the clean tremor signal can be used for tremor source location investigations using array analysis, given that the extracted tremor signal provides the true phase of the signal. This could provide an improved analysis of the spatial and temporal evolution of volcanic tremors during active volcanic periods. The transient signal detection algorithm introduced in this study is a useful tool for detecting seismic events and is especially applicable for detecting small events during an earthquake swarm. We used one component of one station for earthquake detection in this study. The results could be improved using three components and additional stations. This method could provide a new basis for tremor source investigations as well as for eruptive activity analysis because it provides simultaneous information about tremors and earthquakes.

As suggested in Chapter 2, another potential application of our source separation algorithm is in the field of earthquake analysis research. The extracted seismic waveform (after subtracting the tremor signals) results in a higher earthquake SNR. This issue is the subject of my second work where we developed a noise reduction technique based on harmonic–percussive separation algorithms. This method is especially useful for denoising OBS data where the presence of harmonic noises complicates the analysis of transient teleseismic events. For most of the OBS analyses preserving the earthquake signal with true phase and shape after denoising is important. Classical noise reduction techniques do not indeed preserve these signal properties.

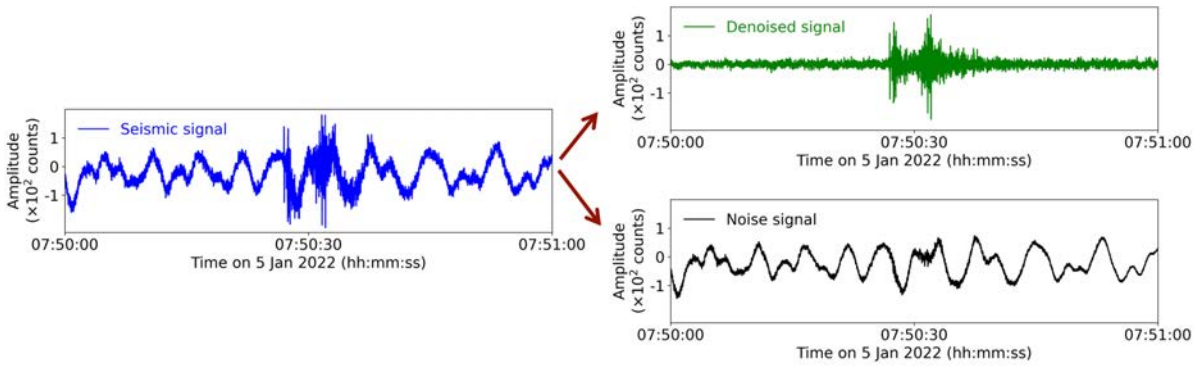

Figure 6.1. An example of removing wind turbine noise from seismic recordings. Data from seismic stations near wind turbines (less than 1 km in this example) may be contaminated by the noise generated by the turbines. Using our algorithm the seismic signal is divided into the denoised and the noise signal.

Our technique is applicable for denoising different data types. In another study (Rein et al., 2022), I used this approach to denoise OBS data recorded at the ultra-slow spreading Knipovich Ridge. This significantly improved the result of the study. I also tried to denoise marsquakes, which are a recent discovery of our community. The initial results are promising but further work is required here. In another ongoing research (not published yet) I denoised records from

seismic stations, which are located close to wind turbines and are affected by the noise generated by the turbines (Figure 6.1). Denoising these seismograms may be of great interest considering the increasing number of wind turbines in Western Europe. The source separation and denoising techniques can be also used for separating transient noises. I contributed to another PhD project to analyze anthropogenic noise using distributed acoustic sensing (DAS) data. There I removed percussive or transient signals (related to train passages) from DAS data. It resulted in higher SNR and improvement in virtual shot gathers (Figure 6.2). These examples show that the algorithms, developed initially for tremor extraction and noise reduction, can have various applications in different seismological research fields.

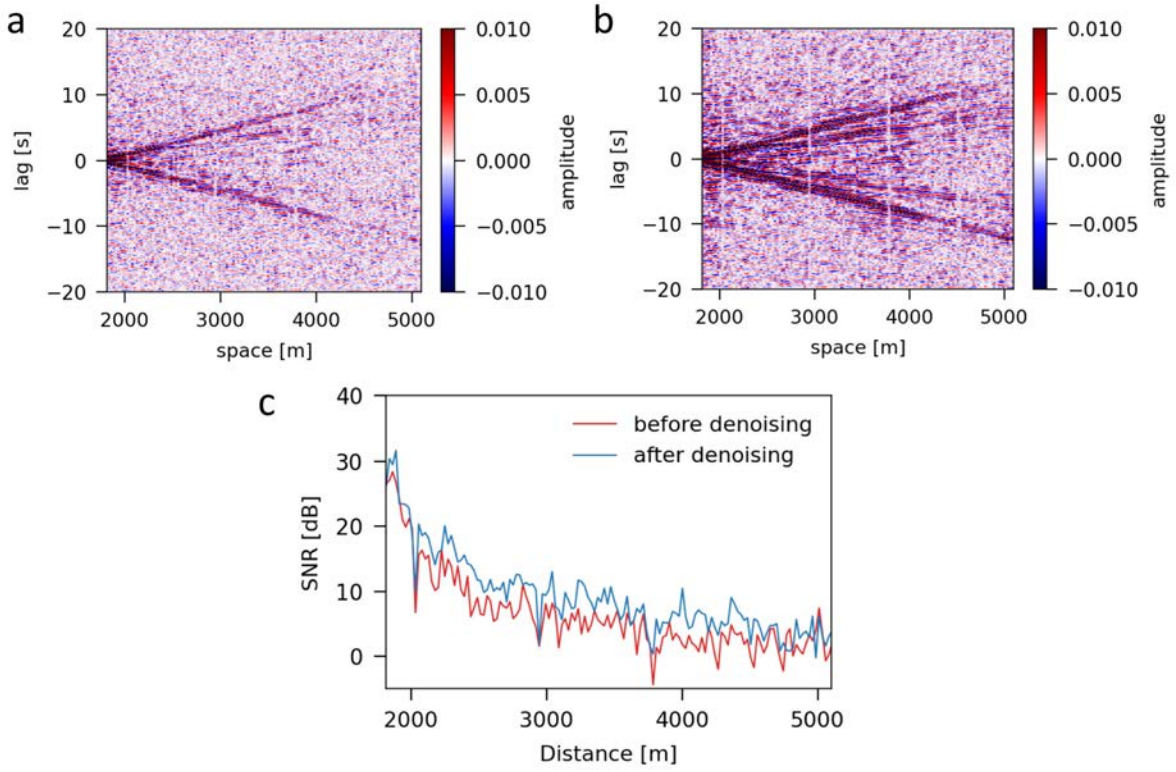

Figure 6.2. Enhancement of coherent signals for Rayleigh waves extraction. a and b show virtual shot gather (Green function retrieval) for original and denoised data respectively. c Comparison of SNR for original and denoised data. The figure is from Ehsaninezhad et al. (submitted abstract to IUGG 2023 conference). The related manuscript is in preparation.

Developing advanced machine learning tools to investigate volcanic activities alongside the classical approaches made my PhD study a comprehensive work that provides a better understanding of the volcanic processes. For the first time, we used deep learning for unsupervised learning of the volcanic tremors. Considering the scarcity of labeled data sets for volcano monitoring unsupervised learning is a suitable and growing approach in this area. Further for the analysis of the continuously growing amount of seismic records, efficient seismic processing techniques are needed. Our method provides a fast and reproducible approach for the automatic revealing of overall temporal evolution patterns of the volcanic systems. It could also discover precursory tremors more systematically, make the eruption prediction potentially possible, contribute to volcanic hazard mitigation efforts, and support timely decision-making. It can potentially be used in other eruptions studies and reveal the chronology of the system. This could be beneficial in revealing different phases of past activities and possibly discovering similar patterns. Volcano observatories aiming to analyze

and interpret data in a timely manner may use this approach for large-scale seismic datasets in a near-real time fashion. In a real-time observation framework, the reoccurrence of a previous cluster may inform about an upcoming similar phase that the system experienced before. In an ongoing study, I am trying to extend this approach by using data from a network instead of one station. I am also using a large dataset that includes different eruptions of one volcano. This could potentially reveal similar/dissimilar patterns of the exhibited volcanic tremors in different sequences of volcanic activities. It could also help to investigate precursory tremors more systematically and potentially find a clear pattern for the precursors that might appear in different eruptions.

I hope that this PhD thesis has contributed to the advancement of the volcano seismological research. New methodological approaches are proposed and they potentially provide a better understanding of solid earth processes. In particular, the algorithms presented here for the analysis of volcanic tremors might be a starting point for a deeper insight of the volcanic system mechanisms. While I believe that this PhD work is a small piece among all the efforts to solve the Earth puzzle, it also raises new questions and motivates further work at the interface between musicology, seismology, and machine learning.

Bibliography

Ágústsdóttir, T., Winder, T., Woods, J., White, R. S., Greenfield, T., & Brandsdóttir, B. (2019). Intense Seismicity During the 2014–2015 Bárðarbunga-Holuhraun Rifting Event, Iceland, Reveals the Nature of Dike-Induced Earthquakes and Caldera Collapse Mechanisms, *J . Geophys. Res.: Solid Earth*, 124(8), 8331-8357. doi:10.1029/2018JB016010.

Ágústsdóttir, T., Woods, J., Greenfield, T., Green, R. G., White, R. S., Winder, T., ... & Soosalu, H. (2016). Strike-slip faulting during the 2014 Bárðarbunga-Holuhraun dike intrusion, central Iceland, *Geophys. Res. Lett*. 43(4), 1495-1503. doi:10.1002/2015GL067423.

Alfred-Wegener-Institut, Helmholtz-Zentrum für Polar- und Meeresforschung et al.: DEPAS (Deutscher Geräte-Pool für amphibische Seismologie): German Instrument Pool for Amphibian Seismology, J. Largescale Res. Facil., 3, A122, https://doi.org/10.17815/jlsrf-3-165, 2017.

Alparone, S., Andronico, D., Lodato, L., & Sgroi, T. Relationship between tremor and volcanic activity during the Southeast Crater eruption on Mount Etna in early 2000. *Journal of Geophysical Research: Solid Earth*, 108 (B5) (2003), https://doi.org/10.1029/2002JB001866.

Ammon, C. J., Randall, G. E., & Zandt, G.: On the nonuniqueness of receiver function inversions, J. Geophys. Res.-Sol. Ea., 95(B10), 15303-15318, https://doi.org/10.1029/JB095iB10p15303, 1990.

An, C., Cai, C., Zhou, L., & Yang, T.: Characteristics of Low-Frequency Horizontal Noise of Ocean-Bottom Seismic Data, Seismol. Res. Lett., https://doi.org/10.1785/0220200349, 2021.

Barsotti, S., Parks, M.M., Pfeffer, M.A., Óladóttir, B.A., Barnie, T., Titos, M.M., Jónsdóttir, K., Pedersen, G.B., Hjartardóttir, Á.R., Stefansdóttir, G. and Johannsson, T. The eruption in Fagradalsfjall (2021, Iceland): how the operational monitoring and the volcanic hazard assessment contributed to its safe access. *Natural Hazards*, pp.1-30 (2023), https://doi.org/10.1007/s11069-022-05798-7.

Bean, C. J., De Barros, L., Lokmer, I., Métaxian, J. P., O'Brien, G., & Murphy, S. Long-period seismicity in the shallow volcanic edifice formed from slow-rupture earthquakes. *Nature geoscience*, 7, 71-75 (2014) https://doi.org/10.1038/ngeo2027.

Bell, S. W., Forsyth, D. W., & Ruan, Y.: Removing noise from the vertical component records of ocean-bottom seismometers: Results from year one of the Cascadia Initiative, B. Seismol. Soc. Am., 105(1), 300-313, https://doi.org/10.1785/0120140054, 2015.

Benoit, J. P., & McNutt, S. R. Global volcanic earthquake swarm database and preliminary analysis of volcanic earthquake swarm duration. *Annali di Geofisica*, 39, 221 (1996).

Beroza, G. C., Segou, M., & Mostafa Mousavi, S. (2021). Machine learning and earthquake forecasting—next steps. *Nature communications*, *12*(1), 4761. https://doi.org/10.1038/s41467-021-24952-6.

Beyreuther, M., Barsch, R., Krischer, L., Megies, T., Behr, Y., Wassermann, J.: ObsPy: A Python Toolbox for Seismology. Seismol. Res. Lett., 81(3), 530-533, 2010.

Brink, K. H.: Tidal and lower frequency currents above Fieberling Guyot. J. Geophys. Res.-: Oceans, 100(C6), 10817-10832, https://doi.org/10.1029/95JC00998, 1995.

Brenguier, F., Mordret, A., Lynch, R., Courbis, R., Campbell, X., Boué, P., ... & Hollis, D. (2019, September). Monitoring of fields using body and surface waves reconstructed from passive seismic ambient noise. *In SEG International Exposition and Annual Meeting*. OnePetro. https://doi.org/10.1190/segam2019-3216217.1

Caliński, T., & Harabasz, J. A dendrite method for cluster analysis. *Communications in Statistics-theory and Methods*, 3 (1), 1-27 (1974), https://doi.org/10.1080/03610927408827101.

Cano, E., FitzGerald, D., Liutkus, A., Plumbley, M. D. & Stöter, F. R. (2018). Musical source separation: An introduction*, IEEE Signal Process Mag*. 36(1), 31-40. doi: 10.1109/MSP.2018.2874719.

Castruccio, A., Clavero, J., Segura, A., Samaniego, P., Roche, O., Le Pennec, J. L., & Droguett, B. Eruptive parameters and dynamics of the April 2015 sub-Plinian eruptions of Calbuco volcano (southern Chile). *Bulletin of Volcanology*, 78, 1-19 (2016) https://doi.org/10.1007/s00445-016-1058-8.

Chardot, L., Jolly, A. D., Kennedy, B. M., Fournier, N., & Sherburn, S. Using volcanic tremor for eruption forecasting at White Island volcano (Whakaari), New Zealand. *Journal of Volcanology and Geothermal Research*, 302, 11-23 (2015), https://doi.org/10.1016/j.jvolgeores.2015.06.001.

Chouet, B. A. Long-period volcano seismicity: its source and use in eruption forecasting. *Nature*, 380(6572), 309-316 (1996), https://doi.org/10.1038/380309a0.

Corela, C.: Ocean bottom seismic noise: applications for the crust knowledge, interaction ocean-atmosphere and instrumental behaviour. Ph.D. thesis, University of Lisbon, 339 pp, 2014.

Crawford, W. C.: Determination of oceanic crustal shear velocity structure from seafloor compliance measurements (Doctoral dissertation, University of California, San Diego), 1994.

Crawford, W. C., & Webb, S. C.: Identifying and removing tilt noise from low-frequency (< 0.1 Hz) seafloor vertical seismic data. B. Seismol. Soc. Am., 90(4), 952-963, https://doi.org/10.1785/0119990121, 2000.

Crawford, W. C., Webb, S. C., & Hildebrand, J. A.: Estimating shear velocities in the oceanic crust from compliance measurements by two-dimensional finite difference modeling. J. Geophys. Res.-Sol. Ea., 103(B5), 9895-9916, https://doi.org/10.1029/97JB03532, 1998.

Cubuk-Sabuncu, Y., Jónsdóttir, K., Caudron, C., Lecocq, T., Parks, M. M., Geirsson, H., & Mordret, A. Temporal seismic velocity changes during the 2020 rapid inflation at Mt. orbjörn-Svartsengi, Iceland, using seismic ambient noise. *Geophysical Research Letters*, 48, e2020GL092265 (2021),
https://doi.org/10.1029/2020GL092265.

Davi, R., O'Brien, G. S., De Barros, L., Lokmer, I., Bean, C. J., Lesage, P., ... & Soto, G. J. (2012). Seismic source mechanisms of tremor recorded on Arenal volcano, Costa Rica, retrieved by waveform inversion, *J. Volcanol. Geotherm.* Res. 213, 1-13. doi:10.1016/j.jvolgeores.2011.10.008.

Deuss, A.: Global observations of mantle discontinuities using SS and PP precursors. Surv. Geophys., 30(4-5), 301-326, https://doi.org/10.1007/s10712-009-9078-y, 2009.

Dmitrieva, K., Hotovec-Ellis, A. J., Prejean, S. & Dunham, E. M. (2013). Frictional-faulting model for harmonic tremor before Redoubt Volcano eruptions, *Nat. Geosci*. 6(8), 652-656. doi: 10.1038/NGEO1879.

Dowla, F. U., Taylor, S. R., & Anderson, R. W. (1990). Seismic discrimination with artificial neural networks: preliminary results with regional spectral data. *Bulletin of the Seismological Society of America*, *80*(5), 1346-1373. https://doi.org/10.1785/BSSA0800051346

Drew, J., White, R. S., Tilmann, F. & Tarasewicz, J. (2013). Coalescence microseismic mapping, *Geophys. J. Int*. 195(3), 1773-1785. doi: 10.1093/gji/ggt331.

Driedger, J., Müller, M. & Disch, S. (2014, October). Extending Harmonic-Percussive Separation of Audio Signals. In ISMIR (pp. 611-616).

Duennebier, F. K., & Sutton, G. H.: Fidelity of ocean bottom seismic observations, Oceanographic Literature Review, 10(43), 996, https://doi.org/10.1007/BF01204343, 1995.

Dziewonski, A., S. Bloch, and M. Landisman.: A technique for the analysis of transient seismic signals, B. Seismol. Soc. Am., 59, no. 1, 427-444, https://doi.org/10.1785/BSSA0590010427, 1969.

Eibl, E. P., Bean, C. J., Vogfjörd, K. S., Ying, Y., Lokmer, I., Möllhoff, M., ... & Pálsson, F. (2017a). Tremor-rich shallow dyke formation followed by silent magma flow at Bárðarbunga in Iceland, *Nat. Geosci*. 10(4), 299-304. doi: 10.1038/NGEO2906.

Eibl, E. P., Bean, C. J., Jónsdóttir, I., Höskuldsson, A., Thordarson, T., Coppola, D. & Walter, T. R. (2017b). Multiple coincident eruptive seismic tremor sources during the 2014–2015 eruption at Holuhraun, Iceland, *J . Geophys. Res.: Solid Earth*, 122(4), 2972-2987. doi:10.1002/2016JB013892.

Eibl EPS, Gnauck U, Hamzaliyev S, Hersir G P, Gudnasson E, Pétursson F. Catalog of start and end times of lava fountaining episodes from 2 May to 14 June 2021 during the Fagradalsfjall eruption (2022a).

Eibl EPS, Hersir GP, Gudnason EA´ , Pe´turson F. 2-year seismological experiment near Fagradalsfjall, Reykjanes peninsula in 2021/22. GFZ Data Services. Other/Seismic Network (2022b).

Eibl, E. P., Thordarson, T., Höskuldsson, Á., Gudnason, E. Á., Dietrich, T., Hersir, G. P., & Ágústsdóttir, T. Evolving shallow conduit revealed by tremor and vent activity observations during episodic lava fountaining of the 2021 Geldingadalir eruption, Iceland. *Bulletin of Volcanology*, 85 (2), 10 (2023), https://doi.org/10.1007/s00445-022-01622-z.

Dokht Dolatabadi Esfahani, R., Vogel, K., Cotton, F., Ohrnberger, M., Scherbaum, F., & Kriegerowski, M. (2021). Exploring the dimensionality of ground-motion data by applying autoencoder techniques. *Bulletin of the Seismological Society of America*, 111(3), 1563-1576. https://doi.org/10.1785/0120200285

Esfahani, R. D., Cotton, F., Ohrnberger, M., & Scherbaum, F. (2023). TFCGAN: Nonstationary Ground-Motion Simulation in the Time–Frequency Domain Using Conditional Generative Adversarial Network (CGAN) and Phase Retrieval Methods. *Bulletin of the Seismological Society of America*, 113(1), 453-467. https://doi.org/10.1785/0120220068

Essing, D., Schlindwein, V., Schmidt-Aursch, M. C., Hadziioannou, C., & Stähler, S. C.: Characteristics of Current-Induced Harmonic Tremor Signals in Ocean-Bottom Seismometer Records, Seismol. Res. Lett., 92(5), 3100-3112. , https://doi.org/10.1785/0220200397, 2021.

Eulenfeld, T.: rf: Receiver function calculation in seismology, *Journal of Open Source Software*, 5(48), 1808, https://doi.org/10.21105/joss.01808, 2020.

Falsaperla, S., Alparone, S., D'Amico, S., Grazia, G., Ferrari, F., Langer, H., ... & Spampinato, S. Volcanic tremor at Mt. Etna, Italy, preceding and accompanying the eruption of July–August, 2001. *pure and applied geophysics*, 162, 2111-2132 (2005), https://doi.org/10.1007/s00024-005-2710-y.

Farrell, J., Husen, S., & Smith, R. B. Earthquake swarm and b-value characterization of the Yellowstone volcano-tectonic system. *Journal of Volcanology and Geothermal Research*, 188, 260-276 (2009). https://doi.org/10.1016/j.jvolgeores.2009.08.008.

Fischer, Tomas, Pavla Hrubcová, Ali Salama, Jana Doubravová, T. Ágústsdóttir, E. Á. Gudnason, J. Horálek, and G. P. Hersir. Swarm seismicity illuminates stress transfer prior to the 2021 Fagradalsfjall eruption in Iceland. *Earth and Planetary Science Letters* 594, 117685 (2022), https://doi.org/10.1016/j.epsl.2022.117685.

Fitzgerald, D. Harmonic/percussive separation using median filtering, In Proceedings of the International Conference on Digital Audio Effects (DAFx) (Vol. 13), 2010.

FitzGerald, D. (2012). Vocal separation using nearest neighbours and median filtering, *23rd IET Irish Signals and Systems Conference*, Maynooth. 28-29th. June 2012. doi: 10.1049/ic.2012.0225.

FitzGerald, D., & Gainza, M. (2010). Single channel vocal separation using median filtering and factorisation techniques*, ISAST Transactions on Electronic and Signal Processing,* No. 1, Vol. 4,2010 (ISSN 1797-2329), pages: 62 - 73, 2010.

Flóvenz, Ó.G., Wang, R., Hersir, G.P., Dahm, T., Hainzl, S., Vassileva, M., Drouin, V., Heimann, S., Isken, M.P., Gudnason, E.Á. and Ágústsson, K. Cyclical geothermal unrest as a precursor to Iceland's 2021 Fagradalsfjall eruption. *Nature Geoscience*, 15 (5), pp.397-404 (2022), https://doi.org/10.1038/s41561-022-00930-5.

Friedrich, A., Krüger, F., & Klinge, K.: Ocean-generated microseismic noise located with the Gräfenberg array, J. Seismol., 2(1), 47-64, https://doi.org/10.1023/A:1009788904007, 1998.

Gaspà Rebull, O., Cusí, J. D., Ruiz Fernández, M., & Muset, J. G.: Tracking fin whale calls offshore the Galicia Margin, north east Atlantic Ocean, The Journal of the Acoustical Society of America, 120(4), 2077-2085, https://doi.org/10.1121/1.2336751, 2006.

Geirsson H, Parks M, Vogfjörd K, Einarsson P, Sigmundsson F, Jónsdóttir K, Drouin V, Ófeigsson B G, Hreinsdóttir S, Ducrocq C. The 2020 volcano-tectonic unrest at Reykjanes Peninsula Iceland: stress triggering and reactivation of several volcanic systems. In: EGU general assembly conference abstracts (2021).
Griffin, D., & Lim, J. (1984). Signal estimation from modified short-time Fourier transform, *IEEE Trans. Acoust. Speech Signal Process*. 32(2), 236-243. doi:10.1109/icassp.1983.1172092.

Griffin, O. M.: Vortex-Induced Vibrations of Marine Cables and Structures, NRL Memorandum Report 5600, Naval Research Laboratory – Marine Technology Division, Washington D.C, 1985.

Gudmundsson, M. T., Jónsdóttir, K., Hooper, A., Holohan, E. P., Halldórsson, S. A., Ófeigsson, B. G., ... & Einarsson, P. (2016). Gradual caldera collapse at Bárdarbunga volcano, Iceland, regulated by lateral magma outflow. *Science*, 353(6296). doi: 10.1126/science.aaf8988.

Halldórsson, S. A., Marshall, E. W., Caracciolo, A., Matthews, S., Bali, E., Rasmussen, M. B., ... & Stefánsson, A. Rapid shifting of a deep magmatic source at Fagradalsfjall volcano, Iceland. *Nature*, 609 (7927), 529-534 (2022), https://doi.org/10.1038/s41586-022-04981-x.

Hannemann, K., Krüger, F., Dahm, T., & Lange, D.: Structure of the oceanic lithosphere and upper mantle north of the Gloria fault in the eastern mid-Atlantic by receiver function analysis, J. Geophys. Res-Sol Ea., 122(10), 7927-7950, https://doi.org/10.1002/2016JB013582, 2017.

Harlow, D. H., Power, J. A., Laguerta, E. P., Ambubuyog, G., White, R. A., & Hoblitt, R. P. Precursory seismicity and forecasting of the June 15, 1991, eruption of Mount Pinatubo. *Fire and Mud: eruptions and lahars of Mount Pinatubo, Philippines*, 223-247 (1996).

Hasselmann, K.: A statistical analysis of the generation of microseisms. Rev. Geophys., 1(2), 177-210, https://doi.org/10.1029/RG001i002p00177, 1963.

Heimann, S., Kriegerowski, M., Isken, M., Cesca, S., Daout, S., Grigoli, F., Juretzek, C., Megies, T., Nooshiri, N., Steinberg, A., Sudhaus, H., Vasyura-Bathke, H., Willey, T., Dahm, T.: Pyrocko - An open-source seismology toolbox and library. V. 0.3. GFZ Data Services, https://doi.org/10.5880/GFZ.2.1.2017.001, 2017.

Hellweg, M. (2000). Physical models for the source of Lascar's harmonic tremor, *J. Volcanol. Geotherm. Res.* 101(1-2), 183-198. doi: 10.1016/S0377-0273(00)00163-3.

Herrmann, R. B.: Computer programs in seismology: An evolving tool for instruction and research, Seism. Res. Lettr., 84, 1081-1088, https://doi.org/10.1785/0220110096, 2013.

Hotovec, A. J., Prejean, S. G., Vidale, J. E., & Gomberg, J. Strongly gliding harmonic tremor during the 2009 eruption of Redoubt Volcano. *Journal of Volcanology and Geothermal Research*, *259*, 89-99 (2013), https://doi.org/10.1016/j.jvolgeores.2012.01.001.

Janiszewski, H. A., Gaherty, J. B., Abers, G. A., Gao, H., & Eilon, Z. C.: Amphibious surface-wave phase-velocity measurements of the Cascadia subduction zone. Geophys. J. Int., 217(3), 1929-1948, https://doi.org/10.1093/gji/ggz051, 2019.

Johnson, J. B., & Watson, L. M.: Monitoring volcanic craters with infrasound "music", Eos, 100. https://doi.org/10.1029/2019EO123979, 2019.

Jónsson, J. Eldgos a sogulegum tima a Reykjanesskaga.(Volcanic eruptions in historical time on the Reykjanes peninsula, South-West Iceland). *Natturufraedingurinn Reykjavik*, 52, 127-139 (1983).

Kaur, H., Fomel, S., & Pham, N. (2020). Seismic ground-roll noise attenuation using deep learning. *Geophysical Prospecting*, *68*(7), 2064-2077. DOI: https://doi.org/10.1111/1365-2478.12985

Kennett, B. L., Engdahl, E. R., & Buland, R.: Constraints on seismic velocities in the Earth from traveltimes. Geophys. J. Int., 122(1), 108-124. https://doi.org/10.1111/j.1365-246X.1995.tb03540.x, 1995.

Khosravikia, F., Clayton, P., & Nagy, Z. (2019). Artificial neural network-based framework for developing ground-motion models for natural and induced earthquakes in Oklahoma, Kansas, and Texas. *Seismological Research Letters*, 90(2A), 604-613. https://doi.org/10.1785/0220180218

Kind, R., Kosarev, G. L., & Petersen, N. V.: Receiver functions at the stations of the German Regional Seismic Network (GRSN). Geophys. J. Int., 121(1), 191-202, https://doi.org/10.1111/j.1365-246X.1995.tb03520.x, 1995.
Kingma, D. P. & Ba, J. Adam: a method for stochastic optimization. In *Proc. 3rd International Conference on Learning Representations (ICLR)* (2015).

Konstantinou, K. I., & Schlindwein, V. Nature, wavefield properties and source mechanism of volcanic tremor: a review. *Journal of volcanology and geothermal research*, 119 (1-4), 161-187 (2003), https://doi.org/10.1016/S0377-0273(02)00311-6.

Lamb, O. D., Gestrich, J. E., Barnie, T. D., Jónsdóttir, K., Ducrocq, C., Shore, M. J., ... & Lee, S. J. Acoustic observations of lava fountain activity during the 2021 Fagradalsfjall eruption, Iceland. *Bulletin of Volcanology*, 84 (11), 96 (2022), https://doi.org/10.1007/s00445-022-01602-3.

Langston, C.A.: Structure under Mount Rainier, Washington, inferred from teleseismic body waves. J. Geophys. Res., 84, 4749-4762, https://doi.org/10.1029/JB084iB09p04749, 1979.

Lara-Benítez, P., Carranza-García, M., & Riquelme, J. C. (2021). An experimental review on deep learning architectures for time series forecasting. *International Journal of Neural Systems*, *31*(03), 2130001. https://doi.org/10.1142/S0129065721300011.

Larsen, J., Neal, C., Webley, P., Freymueller, J., Haney, M., McNutt, S., ... & Wessels, R. Eruption of Alaska volcano breaks historic pattern. *Eos, Transactions American Geophysical Union*, 90 (20), 173-174 (2009), https://doi.org/10.1029/2009EO200001.

Ligorría, J. P., & Ammon, C. J.: Iterative deconvolution and receiver-function estimation. B. Seismol. Soc. Am., 89(5), 1395-1400, https://doi.org/10.1785/BSSA0890051395, 1999.

Lilienkamp, H., von Specht, S., Weatherill, G., Caire, G., & Cotton, F. (2022). Ground-motion modeling as an image processing task: Introducing a neural network based, fully data-driven, and nonergodic approach. *Bulletin of the Seismological Society of America*, 112(3), 1565-1582. https://doi.org/10.1785/0120220008

Longuet-Higgins, M. S.: A theory of the origin of microseisms, Philosophical Transactions of the Royal Society of London. Series A, Mathematical and Physical Sciences, 243(857), 1-35, https://doi.org/10.1098/rsta.1950.0012, 1950.

MacQueen, J. Classification and analysis of multivariate observations. In *5th Berkeley Symp. Math. Statist. Probability* (pp. 281-297). Los Angeles LA USA: University of California (1967, June).

McFee, B., V. Lostanlen, A. Metsai, M. McVicar, S. Balke, C. Thomé, C. Raffel, F. Zalkow, A. Malek, Dana, et al.: librosa/librosa: 0.8.0, Version 0.8.0, Zenodo, https://doi.org/10.5281/zenodo.3955228, 2020.

McNutt, S. R. (1992). Volcanic tremor, *Encyclopedia of earth system science*, 4, 417-425.

McNutt, S. R., & Nishimura, T. Volcanic tremor during eruptions: temporal characteristics, scaling and constraints on conduit size and processes. *Journal of Volcanology and Geothermal Research*, 178 (1), 10-18 (2008), https://doi.org/10.1016/j.jvolgeores.2008.03.010.

Montegrossi, G., Farina, A., Fusi, L., & De Biase, A. (2019). Mathematical model for volcanic harmonic tremors. *Scientific reports*, 9(1), 1-14.

Moran, S. C., Newhall, C., & Roman, D. C. Failed magmatic eruptions: late-stage cessation of magma ascent. *Bulletin of Volcanology*, 73, 115-122 (2011), https://doi.org/10.1007/s00445-010-0444-x.

Mousavi, S. M., & Beroza, G. C. (2022). Deep-learning seismology. *Science*, *377*(6607), eabm4470. DOI: 10.1126/science.abm4470

Mousavi, S. M., & Beroza, G. C. (2023). Machine Learning in Earthquake Seismology. *Annual Review of Earth and Planetary Sciences*, *51*. https://doi.org/10.1146/annurev-earth-071822-100323

Mousavi, S. M., & Langston, C.A.: Automatic noise-removal/signal-removal based on general cross-validation thresholding in synchrosqueezed domain and its application on earthquake data. Geophysics, 82.4, V211-V227. https://doi.org/10.1190/geo2016-0433.1, 2017.

Mousavi, S. M., Zhu, W., Ellsworth, W., & Beroza, G. Unsupervised clustering of seismic signals using deep convolutional autoencoders. *IEEE Geoscience and Remote Sensing Letters*, 16 (11), 1693-1697 (2019) https://doi.org/10.1109/LGRS.2019.2909218.

Müller, M. (2015). Fundamentals of music processing: Audio, analysis, algorithms, applications. Cham, Switzerland: *Springer International Publishing*. doi: 10.1007/978-3-319-21945-5.

Nakano, M., Sugiyama, D., Hori, T., Kuwatani, T., & Tsuboi, S. (2019). Discrimination of seismic signals from earthquakes and tectonic tremor by applying a convolutional neural network to running spectral images. *Seismological Research Letters*, *90*(2A), 530-538. https://doi.org/10.1785/0220180279

Negi, S. S., Kumar, A., Ningthoujam, L. S., & Pandey, D. K.: An Efficient Approach of Data Adaptive Polarization Filter to Extract Teleseismic Phases from the Ocean-Bottom Seismograms. Seismological Society of America, 92(1), 528-542, https://doi.org/10.1785/0220200034, 2021.

Olofsson, B.: Marine ambient seismic noise in the frequency range 1–10 Hz. The Leading Edge, 29(4), 418-435, https://doi.org/10.1190/1.3378306, 2010.

Pedersen, G. B., Belart, J. M., Óskarsson, B. V., Gudmundsson, M. T., Gies, N., Högnadóttir, T., ... & Oddsson, B. Volume, effusion rate, and lava transport during the 2021 Fagradalsfjall eruption: Results from near real-time photogrammetric monitoring. *Geophysical Research Letters*, 49 (13), e2021GL097125 (2022), https://doi.org/10.1029/2021GL097125.

Peng, P., He, Z., Wang, L., & Jiang, Y. (2020). Automatic classification of microseismic records in underground mining: a deep learning approach. *IEEE Access*, *8*, 17863-17876. doi: 10.1109/ACCESS.2020.2967121

Pereira, A., Romagosa, M., Corela, C., Silva, M. A., & Matias, L.: Source Levels of 20 Hz Fin Whale Notes Measured as Sound Pressure and Particle Velocity from Ocean-Bottom Seismometers in the North Atlantic. Journal of Marine Science and Engineering, 9(6), 646, https://doi.org/10.3390/jmse9060646, 2021.

Peterson, J. R. (1993). Observations and modeling of seismic background noise (No. 93-322). *US Geological Survey*. doi:10.3133/ofr93322.

Pillet, R., Deschamps, A., Legrand, D., Virieux, J., Béthoux, N., & Yates, B.: Interpretation of broadband ocean-bottom seismometer horizontal data seismic background noise, B. Seismol. Soc. Am., 99(2B), 1333-1342, https://doi.org/10.1785/0120080123, 2009.

Power, J. A., & Lalla, D. J. *Seismic observations of Augustine Volcano, 1970-2007: Chapter 1 in The 2006 eruption of Augustine Volcano, Alaska* (No. 1769-1, pp. 3-40). US Geological Survey (2010), https://doi.org/10.3133/pp17691.

Privitera, E., Sgroi, T., & Gresta, S. Statistical analysis of intermittent volcanic tremor associated with the September 1989 summit explosive eruptions at Mount Etna, Sicily. *Journal of volcanology and geothermal research*, 120 (3-4), 235-247 (2003) https://doi.org/10.1016/S0377-0273(02)00400-6.

Rafii, Z., Liutkus, A., & Pardo, B.: REPET for background/foreground separation in audio. In Blind Source Separation (pp. 395-411). Springer, Berlin, Heidelberg, https://doi.org/10.1007/978-3-642-55016-4_14, 2014.

Rafii, Z., Liutkus, A., Stöter, F. R., Mimilakis, S. I., FitzGerald, D., & Pardo, B. (2018). An overview of lead and accompaniment separation in music*, IEEE/ACM Transactions on Audio, Speech, and Language Processing*, 26(8), 1307-1335. doi: 10.1109/TASLP.2018.2825440.

Rafii, Z., & Pardo, B. (2011, May). A simple music/voice separation method based on the extraction of the repeating musical structure, In *2011 IEEE International Conference on Acoustics, Speech and Signal Processing (ICASSP)* (pp. 221-224). IEEE. Doi: 10.1109/ICASSP.2011.5946380.

Rafii, Z., & Pardo, B. (2012, October). Music/Voice Separation Using the Similarity Matrix, In *ISMIR* (pp. 583-588).
Ramakrushana Reddy, T., Dewangan, P., Arya, L., Singha, P., & Kamesh Raju, K. A. Tidal triggering of the harmonic noise in ocean-bottom seismometers. Seismol. Res. Lett., 91(2A), 803-813, https://doi.org/10.1785/0220190080, 2020.

Reckziegel, F., Bustos, E., Mingari, L., Báez, W., Villarosa, G., Folch, A., ... & Osores, S. Forecasting volcanic ash dispersal and coeval resuspension during the April–May 2015 Calbuco eruption. *Journal of Volcanology and Geothermal Research*, 321, 44-57 (2016), https://doi.org/10.1016/j.jvolgeores.2016.04.033.

Rein, T., Zali, Z., Krüger, F., & Schlindwein, V. (2022, May). Receiver Function analysis of noise reduced OBS data recorded at the ultra-slow spreading Knipovich Ridge. *In EGU General Assembly Conference Abstracts (pp. EGU22-3755)*. DOI: 10.5194/egusphere-egu22-3755

Romanowicz, B., Stakes, D., Montagner, J. P., Tarits, P., Uhrhammer, R., Begnaud, M., Stutzmann, E., Pasyanos, M., Karczewski, J.F., Etchemendy, S. and Neuhauser, D.: MOISE: A pilot experiment towards long term sea-floor geophysical observatories, Earth, planets and space, 50(11), 927-937, https://doi.org/10.1186/BF03352188, 1998.

Rondenay, S.: Upper mantle imaging with array recordings of converted and scattered teleseismic waves. Surv. Geophys., 30(4), 377-405, https://doi.org/10.1007/s10712-009-9071-5, 2009.

Rouland, D., Legrand, D., Zhizhin, M., & Vergniolle, S. (2009). Automatic detection and discrimination of volcanic tremors and tectonic earthquakes: An application to Ambrym volcano, Vanuatu, *J. Volcanol. Geotherm.* Res. 181(3-4), 196-206. doi: 10.1016/j.jvolgeores.2009.01.019.

Saad, O. M., & Chen, Y. (2020). Deep denoising autoencoder for seismic random noise attenuation. *Geophysics*, *85*(4), V367-V376. https://doi.org/10.1190/geo2019-0468.1

Sabit, J. P., Pigtain, R. C., & De la Cruz, E. G. The west-side story: observations of the 1991 Mount Pinatubo eruptions from the west. *Fire and mud: eruptions and lahars of Mount Pinatubo, Philippines. University of Washington Press, Seattle*, 445-455 (1996).

Schlindwein, V., Krüger, F., Schmidt-Aursch, M.: Project KNIPAS: DEPAS ocean-bottom seismometer operations in the Greenland Sea in 2016-2017, Alfred Wegener Institute, Helmholtz Centre for Polar and Marine Research, Bremerhaven, PANGAEA, https://doi.org/10.1594/PANGAEA.896635, 2018.

Schlindwein, V., Wassermann, J., & Scherbaum, F. (1995). Spectral analysis of harmonic tremor signals at Mt. Semeru volcano, Indonesia, *Geophys. Res. Lett*. 22(13), 1685-1688. doi:10.1029/95GL01433.

Shelly, D. R., Taira, T. A., Prejean, S. G., Hill, D. P., & Dreger, D. S. Fluid-faulting interactions: Fracture-mesh and fault-valve behavior in the February 2014 Mammoth Mountain, California, earthquake swarm. *Geophysical Research Letters*, *42*(14), 5803-5812. (2015), https://doi.org/10.1002/2015GL064325.

Sigmundsson, F., Hooper, A., Hreinsdóttir, S., Vogfjörd, K. S., Ófeigsson, B. G., Heimisson, E. R., ... & Drouin, V. (2015). Segmented lateral dyke growth in a rifting event at Bárðarbunga volcanic system, Iceland*, Nature*, 517(7533), 191-195. doi: 10.1038/nature14111.

Sigmundsson F, Parks M, Hooper AJ, Geirsson H, Vogfjörd KS, Drouin V, Ofeigsson B, Hreinsdottir S, Hjaltadottir S, Einarsson P, Jonsdottir K, Barsotti S (2021) Un-stressing of crust prior to eruptions: precursors to the 2021 eruption at Geldingadalir, Mt. Fagradalsfjall, in the Reykjanes Peninsula Oblique Rift, Iceland. In: AGU Fall Meeting 2021.

Sigmundsson, F., Parks, M., Hooper, A., Geirsson, H., Vogfjörd, K. S., Drouin, V., ... & Ágústsdóttir, T. Deformation and seismicity decline before the 2021 Fagradalsfjall eruption. *Nature*, 609(7927), 523-528 (2022), https://doi.org/10.1038/s41586-022-05083-4.

Sigurdsson, H., & Carey, S. (1985). The Eruption of. *National Geographic Research*, *1*(3), 332-387.

Sigurgeirsson, M. Á. The Younger-Stamp ar eruption at Reykjanes, SW Iceland. *Náttúrufræðingurinn*, 64, 211-230 (1995).

Silver, P.G. & Chan, W.W.: Shear wave splitting and subcontinental mantle deformation. J. Geophys. Res., 96, 16429-16454, https://doi.org/10.1029/91JB00899, 1991.

Simkin, T., Siebert, L., McClelland, L., Bridge, D., Newhall, C., & Latter, J. H. (1981). Volcanoes of the world: a regional directory, gazetteer, and chronology of volcanism during the last 10,000 years. In *Volcanoes of the world: A regional directory, gazetteer, and chronology of volcanism during the last 10,000 years*. US Hutchinson Ross Publishing.

Skop, R. A., & Griffin, O. M.: On a theory for the vortex-excited oscillations of flexible cylindrical structures. Journal of Sound and Vibration, 41(3), 263-274, https://doi.org/10.1016/S0022-460X(75)80173-8, 1975.
Snodgrass, F. E., Hasselmann, K. F., Miller, G. R., Munk, W. H., & Powers, W. H.: Propagation of ocean swell across the Pacific, Philosophical Transactions of the Royal Society of London. Series A, Mathematical and Physical Sciences, 259(1103), 431-497, https://doi.org/10.1098/rsta.1966.0022, 1996.

Snover, D., Johnson, C. W., Bianco, M. J., & Gerstoft, P. Deep clustering to identify sources of urban seismic noise in Long Beach, California. *Seismological Society of America*, 92 (2A), 1011-1022 (2021), https://doi.org/10.1785/0220200164.

Sparks, R. S. J. Forecasting volcanic eruptions. *Earth and Planetary Science Letters*, 210 (1-2), 1-15 (2003) https://doi.org/10.1016/S0012-821X(03)00124-9.

Stähler, S. C., Schmidt-Aursch, M. C., Hein, G., & Mars, R.: A self-noise model for the German DEPAS OBS pool. Seismol. Res. Lett., 89(5), 1838-1845, https://doi.org/10.1785/0220180056, 2018.

Steinbach, M., Ertöz, L., & Kumar, V. The challenges of clustering high dimensional data. *New directions in statistical physics: econophysics, bioinformatics, and pattern recognition*, 273-309 (2004), https://doi.org/10.1007/978-3-662-08968-2_16.

Sturmel, N., & Daudet, L. (2011, September). Signal reconstruction from STFT magnitude: A state of the art, In *International conference on digital audio effects (DAFx)* (pp. 375-386).

Swanson, D. A., Casadevall, T. J., Dzurisin, D., Holcomb, R. T., Newhall, C. G., Malone, S. D., & Weaver, C. S. Forecasts and predictions of eruptive activity at Mount St. Helens, USA: 1975–1984. *Journal of Geodynamics*, 3 (3-4), 397-423 (1985), https://doi.org/10.1016/0264-3707(85)90044-4.

Sæmundsson, K., Sigurgeirsson, M. Á., & Friðleifsson, G. Ó. Geology and structure of the Reykjanes volcanic system, Iceland. *Journal of Volcanology and Geothermal Research*, 391, 106501 (2020), https://doi.org/10.1016/j.jvolgeores.2018.11.022.

Tanimoto, T., Rivera, L.: The ZH ratio method for long-period seismic data: sensitivity kernels and observational techniques. Geophys. J. Int., 172(1), 187-198, https://doi.org/10.1111/j.1365-246X.2007.03609.x, 2008.

Takano, T., Brenguier, F., Campillo, M., Peltier, A., & Nishimura, T. (2020). Noise-based passive ballistic wave seismic monitoring on an active volcano. *Geophysical Journal International*, 220(1), 501-507. https://doi.org/10.1093/gji/ggz466

Taylor, G. A. (1958). The 1951 eruption of Mount Lamington, Papua. *Aust. Bur. Miner. Resour. Geol. Geophys. Bull.*, *38*, 1-117.

Tilling, R. I. (1989). Volcanic hazards and their mitigation: progress and problems. *Reviews of Geophysics*, *27*(2), 237-269. https://doi.org/10.1029/RG027i002p00237

Titos, M., Bueno, A., García, L., Benitez, C., & Segura, J. C. (2019). Classification of isolated volcano-seismic events based on inductive transfer learning. *IEEE Geoscience and Remote Sensing Letters*, *17*(5), 869-873. DOI: 10.1109/LGRS.2019.2931063
Titze, I. R.: Nonlinear source–filter coupling in phonation: Theory, The Journal of the Acoustical Society of America, 123(4), 1902-1915, https://doi.org/10.1121/1.2832337, 2008.

Turhan Taner, M., Lu, L., & Baysal, E. (1988). Unified method for 2-D and 3-D refraction statics with first break picking by supervised learning. In *SEG Technical Program Expanded Abstracts 1988* (pp. 772-774). Society of Exploration Geophysicists. https://doi.org/10.1190/1.1892424

Van der Maaten, L., & Hinton, G. Visualizing data using t-SNE. *Journal of machine learning research*, 9 (11) (2008).

Vaseghi, S. V.: Advanced signal processing and digital noise reduction. Vieweg + Teubner Verlag, https://doi.org/10.1002/9780470740156, 1996.

Vincent, P., Larochelle, H., Lajoie, I., Bengio, Y., Manzagol, P. A., & Bottou, L. Stacked denoising autoencoders: Learning useful representations in a deep network with a local denoising criterion. *Journal of machine learning research*, 11 (12) (2010).

Wang, R.: A simple orthonormalization method for stable and efficient computation of Green's functions, B. Seismol. Soc. Am., 89(3), 733-741, https://doi.org/10.1785/BSSA0890030733, 1999.

Webb, S. C.: Broadband seismology and noise under the ocean, Rev. Geophys., 36(1), 105-142, https://doi.org/10.1029/97RG02287, 1998.

Webb, S. C., Zhang, X., & Crawford, W.: Infragravity waves in the deep ocean, J. Geophys. Res.-: Oceans, 96(C2), 2723-2736, https://doi.org/10.1029/90JC02212, 1991.

White, R. (2010). Northern Volcanic Zone [Data set], *International Federation of Digital Seismograph Networks*. doi: 10.7914/SN/Z7_2010.

Woods, J., Donaldson, C., White, R. S., Caudron, C., Brandsdóttir, B., Hudson, T. S. & Ágústsdóttir, T. (2018). Long-period seismicity reveals magma pathways above a laterally propagating dyke during the 2014–15 Bárðarbunga rifting event, Iceland, *Earth Planet. Sci. Lett*. 490, 216-229. doi: 10.1016/j.epsl.2018.03.020.

Woods, J., Winder, T., White, R. S. & Brandsdóttir, B. (2019). Evolution of a lateral dike intrusion revealed by relatively-relocated dike-induced earthquakes: The 2014–15 Bárðarbunga–Holuhraun rifting event, Iceland*, Earth Planet. Sci. Lett*. 506, 53-63. doi: 10.1016/j.epsl.2018.10.032.

Xie, J., Girshick, R., & Farhadi, A. Unsupervised deep embedding for clustering analysis. In *International conference on machine learning* (pp. 478-487). PMLR (2016, June).

Yang, B., Fu, X., Sidiropoulos, N. D., & Hong, M. Towards k-means-friendly spaces: Simultaneous deep learning and clustering. In *international conference on machine learning* (pp. 3861-3870). PMLR (2017, July).

Yukutake, Y., Honda, R., Harada, M., Doke, R., Saito, T., Ueno, T., ... & Morita, Y. (2017). Analyzing the continuous volcanic tremors detected during the 2015 phreatic eruption of the Hakone volcano, *Earth Planets Space*, 69(1), 164. doi: 10.1186/s40623-017-0751-y.

Zahra Zali, Matthias Ohrnberger, Frank Scherbaum, Fabrice Cotton, and Eva PS Eibl. Volcanic Tremor Extraction and Earthquake Detection Using Music Information Retrieval Algorithms. *Seismol. Res. Lett*., 92, 3668–3681 (2021), https://doi.org/10.1785/0220210016.

Zahra Zali. (2022a). TremorExtractor-EqDetector (v1.0.0). Zenodo. https://doi.org/10.5281/zenodo.7339603

Zahra Zali. (2022b). ZahraZali/NoiseCut: NoiseCut (v1.0.0). Zenodo. https://doi.org/10.5281/zenodo.7339552

Zahra Zali (2023). ZahraZali/ClusTremor: ClusTremor (v1.0.0). Zenodo. https://doi.org/10.5281/zenodo.8386966

Zahra Zali, Theresa Rein, Frank Krüger, Matthias Ohrnberger, and Frank Scherbaum. Ocean bottom seismometer (OBS) noise reduction from horizontal and vertical components using harmonic–percussive separation algorithms. *Solid Earth* 14, 181-195 (2023), https://doi.org/10.5194/se-14-181-2023.

Zali, Z., Mousavi, S. M., Ohrnberger, M., Eibl, E. P., Cotton, F. Tremor clustering reveals precursors and evolution of the 2021 Geldingadalir eruption, 05 May 2023, PREPRINT (Version 1) available at Research Square. https://doi.org/10.21203/rs.3.rs-2716246/v1

Zhang, Q., Yuan, Q., Li, J., Liu, X., Shen, H., & Zhang, L. (2019). Hybrid noise removal in hyperspectral imagery with a spatial–spectral gradient network. *IEEE Transactions on Geoscience and Remote Sensing*, *57*(10), 7317-7329. DOI: 10.1109/TGRS.2019.2912909

Zhu, W., Mousavi, S. M., & Beroza, G. C.: Seismic signal denoising and decomposition using deep neural networks. IEEE T. Geosci. Remote. 57(11), 9476-9488. https://doi.org/10.1109/TGRS.2019.2926772, 2019.